INTEGRALS OF MOTION FOR FRACTIONATED SPACE SYSTEMS

A Dissertation

Presented to the Faculty of the Graduate School

of Cornell University

in Partial Fulfillment of the Requirements for the Degree of

Doctor of Philosophy

by

Michael Christopher Norman

August 2011

INTEGRALS OF MOTION FOR FRACTIONATED SPACE SYSTEMS

Michael Christopher Norman, Ph.D.

Cornell University 2011

As space system architectures begin to rely upon cooperation between multiple spacecraft to perform a single task, the analysis and control of the relative motion of the individual vehicles becomes a critical component of a successful mission. The approach of a typical constellation of spacecraft is to establish initial orbital conditions such that the natural motion of the individual component spacecraft of the larger system provide the desired Earth coverage, relative separation, or other performance parameters at specified times. When a correction needs to be made, a specific spacecraft can be commanded to perform the required maneuver to reestablish the desired conditions. While this approach is viable for satellite constellations where each component is designed to function independently over large separation distances, future concepts of space systems focus instead on the cooperative interaction of fractionated architectures, where each component spacecraft provides a necessary function to the overall system and cannot necessarily be moved independently.

The inclusion of non-contacting force and torque interactions between the component spacecraft potentially addresses the perceived need of these fractionated space systems to act in a collaborative fashion. By establishing an internal and controllable force dependent upon the relative dynamical states between spacecraft, traditional feedback control approaches provide stabilizing actuator inputs to either maintain or change the relative geometry of the system. Augmenting the dynamics of the individual spacecraft with these

forces, however, effectively introduces a perturbation to their otherwise easily predictable orbital motion about the central body.

This dissertation explores the unique dynamics encountered in these fractionated space system architectures utilizing non-contacting interactions between components. As these non-contacting interactions represent forces and torques internal to the overall system, certain integrals of motion exist that can provide insight to the system dynamics. The relative motion of a model two-spacecraft system dynamically coupled by magnetic flux pinning is analyzed through the development of the equations of motion under a simplifying assumption related to center of mass motion and the implementation of a feedback control law stabilizing the system about identified equilibrium separations. An examination of the integrals of motion under this class of simplifying assumption reveals a violation of their ideally time-independent property that can be related to the induced error in the dynamical state of the fractionated space system. This provides a means to evaluate the validity of these center of mass motion assumptions. A hybrid systems framework for designing recurring non-contacting interactions to accomplish an arbitrary change in orbital elements for these fractionated space systems is developed as well. Finally, applications of identified integrals of motion of space systems to parameter estimation problems are introduced and used to extract the inertia and actuator alignment parameters of a spacecraft with momentum actuators.

BIOGRAPHICAL SKETCH

Michael Christopher Norman was born on May 18, 1984 in Yonkers, New York to Stephen and Clara Ann Norman. He grew up in Richardson, Texas, and attended the nearby St. Mark's School of Texas. After graduating from high school in 2002, he moved north to Pittsburgh, Pennsylvania to attend Carnegie Mellon University. There, he worked in Professor Kenji Shimada's Computer Integrated Engineering Lab and received his Bachelor of Science in Mechanical Engineering in May of 2006.

At the end of his time in Pittsburgh, Michael decided to pursue a life-long interest in the exploration of space by enrolling in the doctoral program at Cornell University's Sibley School of Mechanical and Aerospace Engineering. Professor Mason Peck's Space Systems Design Studio introduced him to the field of spacecraft engineering and provided the context for his work in the analysis and control of complex dynamical systems. He received his Master of Science in Mechanical Engineering in May of 2009 and his Doctorate of Philosophy in Mechanical Engineering in August of 2011 from Cornell University.

To my grandfather, Tom Norman, for helping me discover the elegance of the practical approach to solving problems.

ACKNOWLEDGEMENTS

I believe there exists an inescapable aspect of graduate research that finds you regularly indebted to those who enable you to grasp, grow, and eventually graduate. Lagrange, Euler, and Lyapunov all made unarguably crucial contributions in their time to the theoretical foundations of my dissertation and more, but here I wish to acknowledge instead the more personal gifts of the mentors, friends, and family who gave me the tools to make it to this point.

I would like to thank members of the Cornell community for their role in my graduate studies. Having Dr. Mason Peck as my advisor provided me with a wealth of challenging problems in spacecraft engineering, a solid theoretical background, and a reminder not to restrict myself to considering only the obvious solutions. The efforts of Dr. Mark Campbell and Dr. Joseph Burns were invaluable to my research, providing both constructive feedback and engaging discussions. Thank you all for your academic guidance and patience while helping me understand essential concepts of spacecraft engineering. The part played by my fellow students was likewise integral to my completion of the graduate program. Joseph Shoer, Justin Atchison, Joanna Hinks, and Nisar Ahmed, to name a few among many, helped improve not only my understanding through their collaboration but also my morale through their comradeship. I can only hope to have given as much in return.

The support of my family and friends over the past five years has been just as important, if not more so, as any other aspect of my life in Ithaca. I thank all of my grandparents, Joseph and Lucille Stahl and Tom and Bertha Norman, for their role in bringing me into this loving family and encouraging my curiosity throughout my life. From the care packages using Legos for filler to the regular phone conversations on the walk home, my parents, Stephen and Clara Ann

Norman, made sure that Richardson, Texas never seemed all that far away. My siblings, Joseph Norman and Catherine Deitchman and their families, have always been ready to give me the support, humor, or heckling I needed as the situation warranted. Finally, I want to thank my wife Sarah for her patience, kindness, and love over the years. You bring out the best in me, and I cannot help but smile when I think of the years ahead of us and our humble beginning on one quiet afternoon in Sage Hall.

TABLE OF CONTENTS

LIST OF TABLES

LIST OF FIGURES

CHAPTER 1

INTRODUCTION

The driving design concepts and capabilities behind space system architectures have evolved to match the desire for increased reliability and utility while simultaneously mitigating risk. Although combining all required capabilities for a particular mission into a single monolithic structure represents a familiar spacecraft design paradigm, this approach does not create an easily-scalable solution as the complexity of the system increases. The expected risk over the life of a mission takes many forms: hardware performance, operational environments, funding, demand, and launch operations all contribute significant uncertainties that need to be accounted for in the design process. Brown and Eremenko argue that managing these uncertainties has traditionally led to spacecraft architectures with a longer designed lifetime and greater technical capability.[1] In the context of a monolithic spacecraft, the requirements imposed by this philosophy lead to more massive and more complex spacecraft, which subsequently inherit increased performance risks. Brown, Eremenko and Collopy continue to claim that this approach to risk mitigation results in an inherently less responsive design in the presence of uncertainty at a greater total cost.[2] Their proposed solution to this vicious cycle takes the form of fractionated space systems, where multiple low-complexity spacecraft cooperate to provide the functionality of an equivalent monolithic architecture.

By splitting the functional components across multiple spacecraft, the system architecture potentially accommodates for the aforementioned uncertainties. A fractionated design approach gains flexibility in the form of relative

ease of maintenance and upgrade operations. The Hubble Space Telescope has been the target of several servicing missions and the DARPA Orbital Express program sought to demonstrate unmanned robotic servicing capabilities, but further examples of in-orbit maintenance of unmanned spacecraft beyond these are sparse.[1] Taking a modular approach to the system architecture instead allows for the replacement or retirement of particular functionalities through the launch and subsequent maneuvering of a new component spacecraft. Instead of making all launch- and operations-related risks dependent upon the success of a single complex spacecraft, these risks can instead be distributed across multiple vehicles. This flexibility also allows for resizing of the system's capabilities over time to match evolving demand and funding constraints through judicious addition or removal of individual spacecraft.

While a multi-spacecraft architecture, such as the GPS and Iridium constellations, does not alone represent a novel design paradigm, splitting subsystem functionality across physically separated spacecraft requires some additional consideration. The relative separation and orbit geometry of the individual spacecraft becomes an important factor in designing appropriate communication crosslinks and cooperative behaviors between the system components. This need to analyze the relative motion of the spacecraft has many ties to ideas traditionally associated with spacecraft formation flight. By maintaining capabilities for propulsive maneuvers on each spacecraft, individual orbits can be corrected to account for environmental disturbances to the planned ideal natural motions selected in light of the fractionated system's relative geometry constraints.[1] Future space architectures, such as that of the Magnetospheric Multiscale Mission, utilize a similar strategy to ensure appropriate formation configurations at specified times.[3–5]

Maneuver-planning algorithms for spacecraft formation flight historically focus on utilizing traditional chemical or electric propulsion concepts to change the translational dynamics of one particular spacecraft. Similar to the in-orbit rendezvous problem studied by Clohessy and Wiltshire, dynamical models used in these algorithms typically examine the spacecraft motion relative to a known reference orbit.[4–10] This referenced orbit does not necessarily reflect the position of one component spacecraft of the formation, and frequently is instead assumed to correspond to a 'virtual' spacecraft on an unperturbed Keplerian orbit. This effectively imposes a simplifying constraint on the motion.

This dissertation contends that just as utilizing the conservation of mechanical quantities is essential to our understanding of unperturbed orbital motion in the two-body problem, these integrals of motion are of similar importance to the relative geometry problem for spacecraft formation flight. Of particular interest are technologies that enable non-contacting force and torque interactions between spacecraft. As these interactions are internal to the larger fractionated space system, certain integrals of motion, such as angular momentum, are required to be conserved and of value when analyzing the relative motion. Deriving these conservation laws provide insight to the dynamics of the associated problem by defining relationships between dynamical states at two arbitrary times. Therefore, given the initial conditions of the system, the future states are required to satisfy a known equation and effectively reduce the complexity of the problem.

While the identification of the integrals of motion in single-spacecraft architectures and the relative motion in spacecraft formation flight have both been studied extensively as independent problems, their intersection

holds some potential for understanding the relative motion of these complex fractionated space system architectures. This dissertation approaches this unique area by examining the historical approach to the relative motion problem and moving on to describe how this approach affects known integrals of motion. The specific contributions of this body of work are :

1. Analysis of the relative motion and control of a model close-proximity formation of two spacecraft utilizing an internal, non-contacting force for stationkeeping.
2. Demonstration through simulation of the viability of using non-contacting forces to maintain relative position in an example ring formation in the presence of force and torque disturbances.
3. Identification of relevant integrals of motion for model spacecraft formations for use in relative motion analysis.
4. Mathematical description of the relationship between known errors introduced to integrals of motion of fractionated space systems through center-of-mass motion assumptions and the resulting simulation errors in spacecraft relative-motion states.
5. Construction of a hybrid systems framework to be used in designing relative motion of infrequently interacting fractionated space systems.
6. Utilization of known integrals of motion to extract inertia and actuator alignment characteristics of spacecraft from available telemetry data.
7. Implementation of the developed inertia and actuator alignment parameter estimators on both simulated calibration maneuvers and several downlinked sets of telemetry data from the MESSENGER spacecraft.

As the unique dynamics introduced to fractionated space systems through non-contacting forces serves as motivation for several of the contributions of this dissertation, Chapter 2 introduces several models of these interactions utilized here and throughout the literature. As forces and torques acting between specified bodies in a larger multi-body fractionated space system, these internal interactions cannot directly affect the system angular momentum, one of the frequently identified integrals of motion for idealized spacecraft models. Potential functions generating these force and torque models are also provided and are suitable for integration into the material of the remaining chapters that utilize a Lagrangian approach in their analysis.

Chapter 3 introduces a simple model of a close-proximity formation with a non-contacting force acting between the two bodies. The specific force simulated is based upon a further simplification of the magnetic flux-pinning force model presented in Section 2.4. Utilizing an assumption regarding the orbital path of the center of mass of the formation about the central body, the dynamics equations describing the relative motion of the system are developed in detail in Appendix A utilizing the framework suggested by Kane and Levinson.[11] This process identifies potential stable and unstable equilibrium separation distances between the spacecraft. A sample feedback control law is developed to stabilize the system about these equilibrium separations for a simulated orbital configuration.

While the controlled response of a two-spacecraft formation utilizing magnetic flux pinning represents a motivating sample fractionated space system, investigation of the dynamics of a formation incorporating many more elements holds merit as well. Chapter 4 addresses this area by examining

the natural response of an example ring formation of vehicles linked together with magnetic flux pinning in the presence of disturbance torques and forces. By taking advantage of the stable equilibrium separation distances between spacecraft identified in Chapter 3, the ring formation loosely maintains its intended shape.

Chapter 5 addresses the analysis of fractionated space system architectures through identification of integrals of motion. These integrals represent conserved quantities that not only allow for the dynamics states at two distinct times to be related through an algebraic equation but also provide further insight into the errors introduced through simplifying assumptions. As is done in Chapter 3 and elsewhere in the literature, assuming the center of mass of a system follows a predetermined path, usually a circular orbit, allows for a potentially more intuitive representation of the dynamics of the relative motion of two bodies.[4,5,12,13] These assumptions effectively impose constraint forces and torques on the system, resulting in the identified integrals of motion acquiring an erroneous time-varying nature. This known induced error in the supposedly conserved quantities can then be related to induced errors in the relative motion of the component bodies of the system. Identifying this relationship between a known integral of motion error and the more relevant dynamics states potentially serves to validate the original assumptions. While Chapter 5 makes specific use of the Photonic Laser Propulsion (PLP) interaction in the derivation, the analysis is such that any of the interaction potential functions given in Chapter 2 could be utilized in its place.

While Chapters 3 and 4 focused on applying non-contacting forces to the stationkeeping problem, Chapter 6 instead introduces a hybrid systems

framework that can describe the cumulative effect of distinct interaction periods between components of a fractionated space system. Switches between two discrete modes with different dynamics functions, namely one including the non-contacting interaction and a second without it, are governed both by a user-defined schedule and also physical limitations due to maximum effective distances of the interactions and line-of-sight effects. By picking appropriate discrete interactions between spacecraft resulting in small changes to the overall system, these individual effects accumulate over multiple interactions and result in significant changes in the system output. The selection of the switching times between the two discrete modes is related to the sensitivities of the states to the interaction input. The motivating example provided is that of countering atmospheric drag using PLP between two spacecraft in identically-sized orbits in opposite directions.

Chapter 7 makes use of known integrals of motion to estimate physical parameters of a space system. Specifically, the angular momentum and rotational kinetic energy of a rigid body provide the measurement equations in a linearized filtering scheme that estimates inertia-matrix parameters and momentum-actuator alignments from attitude dynamics data. Appendix B describes the specific representation of actuator alignment error implemented in the resulting algorithms. Filter variants utilizing different measurement equations are evaluated both over a set of simulated maneuvers and also over several calibration maneuver data sets from the MESSENGER spacecraft. While the chapter focuses on applications to a single spacecraft, the concept of utilizing integrals of motion for parameter estimation of fractionated space systems hold some potential as well.

CHAPTER 2

NON-CONTACTING INTERACTIONS FOR SPACE SYSTEMS ARCHITECTURES

Non-contacting interactions between different spacecraft have the potential to conserve important mechanical quantities of a larger fractionated space system and are therefore of particular importance to this dissertation. Several candidate technologies have been suggested to establish this type of interaction, all of which can be represented with some degree of fidelity as potential energy functions modifying the scalar Lagrangian function used in deriving equations of motion of the system. This approach is effectively that taken in Chapter 5 to aid in the identification of integrals of motion. For a potential function $\mathcal{V}$ and system kinetic energy of $\mathcal{T}$, the Lagrangian is

$$\mathcal{L} = \mathcal{T} - \mathcal{V} \tag{2.1}$$

Using Lagrange's approach, the equations of motion of the system described by generalized coordinates q in the absence of non-conservative forces and constraints is[14]

$$\frac{d}{dt}\left(\frac{\partial}{\partial \dot{q}}\mathcal{L}\right) - \frac{\partial}{\partial q}\mathcal{L} = 0 \tag{2.2}$$

The potential functions produced by these interactions could alternatively be viewed as conservative perturbations to the two-body motion of the individual spacecraft and allow for the use of Lagrange's Planetary Equations to describe the resulting changes in the classical orbital elements of each spacecraft.[15]

The four candidate technologies reviewed are Electromagnetic Formation Flight (EMFF), Virtual Coulomb Structures (VCS), Photonic Laser Propulsion

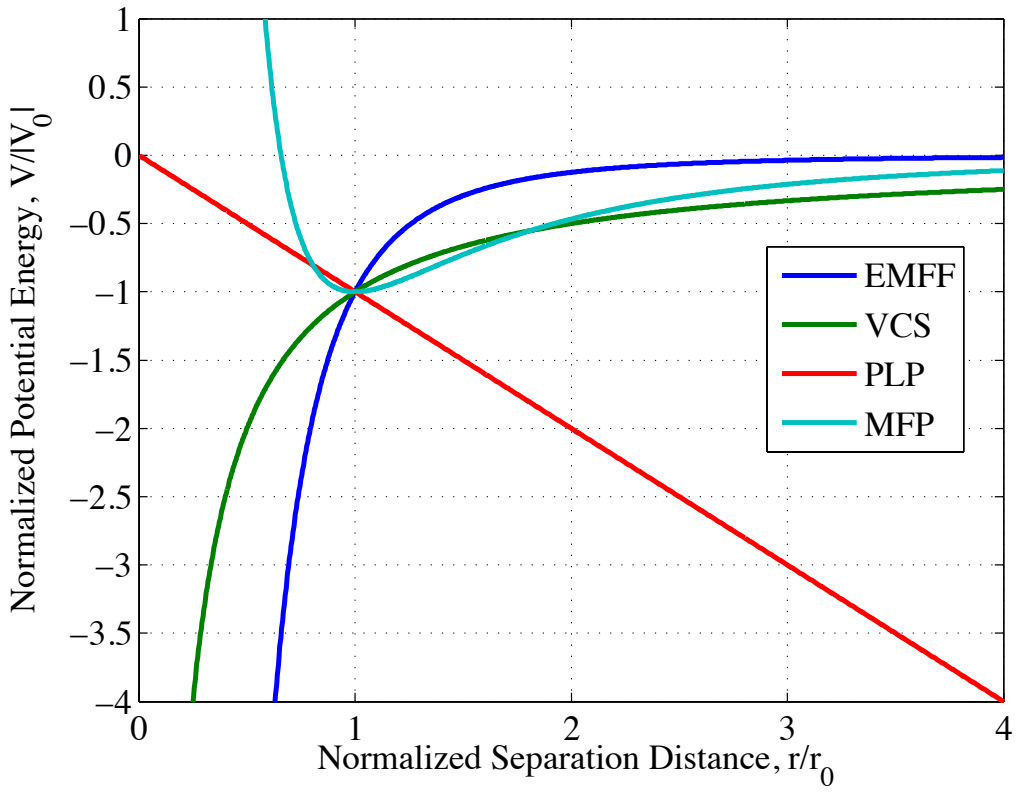

Figure 2.1: Normalized interaction potential functions variation over separation distance.

(PLP), and Magnetic Flux Pinning (MFP). Figure 2.1 qualitatively describes how the model potential functions for these interactions vary with separation distance. Normalizing the potential functions by their value at scalar separation r_0 can equivalently be thought of as sizing the individual interactions to have the same potential energy contribution to the system Lagrangian at the selected nominal separation. Equation (2.2) indicates that the force produced by a particular interaction corresponds to how the potential function changes as a function of a particular generalized coordinate. Figure 2.1 qualitatively

describes these changes, reflecting some of the unique qualities of each option.

2.1 Electromagnetic Formation Flight

EMFF can essentially be represented as the electromagnetic interaction between a group of steerable magnetic dipoles placed on each component of the fractionated space system. The vector magnetic field **B** of a dipole with a vector magnetic moment of $\boldsymbol{\mu}$ at a relative position given by **r** is described by Eq. (2.3) in terms of the constant permeability of free space, μ_0.

$$\mathbf{B}(\boldsymbol{\mu}, \mathbf{r}) = \frac{\mu_0}{4\pi r^3}\left(3(\boldsymbol{\mu}\cdot\hat{\mathbf{r}})\hat{\mathbf{r}} - \boldsymbol{\mu}\right) \tag{2.3}$$

Placing one dipole $\boldsymbol{\mu}_1$ in the presence of a second dipole $\boldsymbol{\mu}_2$ with a relative location given by the position vector **r** has a related potential energy function $\mathcal{V}_m$.

$$\begin{aligned}\mathcal{V}_m &= -\boldsymbol{\mu}_1\cdot\mathbf{B}(\boldsymbol{\mu}_2, \mathbf{r}) \\ &= \frac{\mu_0}{4\pi r^3}\left(\boldsymbol{\mu}_1\cdot\boldsymbol{\mu}_2 - 3(\boldsymbol{\mu}_1\cdot\hat{\mathbf{r}})(\boldsymbol{\mu}_2\cdot\hat{\mathbf{r}})\right)\end{aligned} \tag{2.4}$$

Landecker, Villani, and Yung assume a current loop model of a magnetic dipole and derive expressions for the force $\mathbf{f}_{12}$ and torque $\boldsymbol{\tau}_{12}$ that dipole $\boldsymbol{\mu}_1$ applies to dipole $\boldsymbol{\mu}_2$.[16]

$$\mathbf{f}_{12} = \frac{3\mu_0}{4\pi r^5}\left(\mathbf{r}(\boldsymbol{\mu}_1\cdot\boldsymbol{\mu}_2) + \boldsymbol{\mu}_1(\mathbf{r}\cdot\boldsymbol{\mu}_2) + \boldsymbol{\mu}_2(\mathbf{r}\cdot\boldsymbol{\mu}_1) - \frac{5}{r^2}\mathbf{r}(\mathbf{r}\cdot\boldsymbol{\mu}_1)(\mathbf{r}\cdot\boldsymbol{\mu}_2)\right) \tag{2.5a}$$

$$\boldsymbol{\tau}_{12} = \frac{\mu_0}{4\pi r^5}\left(3(\boldsymbol{\mu}_1\cdot\mathbf{r})(\boldsymbol{\mu}_2\times\mathbf{r}) + r^2\boldsymbol{\mu}_1\times\boldsymbol{\mu}_2\right) \tag{2.5b}$$

These force and torque representations can also be derived through the use of the potential function from Eq. 2.4 in Eq. 2.2 for a given system configuration.

EMFF represents a promising candidate technology for controlling the relative positions of spacecraft in a fractionated space system. Miller *et al*.

initially described EMFF in the context of the proposed Terrestrial Planet Finder (TPF) mission.[17] Kong *et al*. develop a cost functions for use in optimally sizing relevant EMFF hardware for TPF.[18] Elias, Kwon, Sedwick, and Miller examine the linearized dynamics of a two-spacecraft EMFF setup including reaction wheels and develop an associated feedback control law for managing the formation geometry.[19] The literature to date has focused on the dynamics of fractionated space systems utilizing EMFF outside an orbital context, thereby ignoring the tidal of gravitational attraction to a central body on the relative motion of the components.

2.2 Virtual Coulomb Structures

The concept behind VCS is conceptually simple: by establishing an electric charge on two spacecraft, electrostatic attraction will contribute an attractive or repulsive force based on the sign of the product of the charges. The potential function $\mathcal{V}_c$ for two point charges, Q_1 and Q_2 separated by scalar distance r is given by Eq. (2.6) in terms of the permittivity of free space ϵ_0.

$$\mathcal{V}_c = \frac{Q_1 Q_2}{4\pi\epsilon_0 r} \tag{2.6}$$

Equation (2.6) produces a corresponding force $\mathbf{f}_{12}$ between two electrically-charged point masses.

$$\mathbf{f}_{12} = \frac{Q_1 Q_2}{4\pi\epsilon_0 r^3}\mathbf{r} \tag{2.7}$$

No torque is produced between two point charges. Equation (2.7) has to be modified in an Earth-orbiting context so as to account for the effects of the electrically charged plasma environment. The plasma environment shields the

influence of one charged body on another, and can be approximated through a characteristic Debye length λ_d and modification of Eq. (2.7) to the form of Eq. (2.8).[20]

$$\mathbf{f}_{12} = \frac{Q_1 Q_2}{4\pi\epsilon_0 r^3} e^{-r/\lambda_d} \mathbf{r} \tag{2.8}$$

Due to altitude-based variations in the space plasma environment, this Debye length typically decreases as altitude increases, reducing the influence of the exponential term included in Eq. (2.8) and thereby making VCS an attractive option for high orbit altitudes.

Schaub and Natarajan examine the dynamics and stability of a two-spacecraft VCS formation relative to a circular reference orbit.[12,20] Berryman and Schaub identify charges establishing equilibrium conditions for a three-spacecraft formation in a rotating Hill frame.[8] Kim and Schaub identify conserved quantities for a VCS spacecraft formation and examins the effect of simplifying center of mass motion assumptions on the spacecraft trajectory.[21]

2.3 Photonic Laser Propulsion

A relatively novel concept for spacecraft formation flight is that of Photonic Laser Propulsion. This concept establishes an optical cavity between two spacecraft by reflecting light between two mirrors. With each reflection, photons impart some momentum on the mirror and attached spacecraft bus. The resulting force can only be used to establish tension, rather than compression, between the spacecraft. Bae developed a proof-of-concept demonstration of this technology in a terrestrial environment.[22] Tragesser explores the relative motion of a spacecraft formation utilizing PLP with respect to a reference orbit.[13]

Both Bae and Tragesser propose the use of a model for PLP where the effective force produced by the system is invariant as the separation distance between the spacecraft increases.[13,22] For a given relative position vector $\mathbf{r}$ and constant K, the force of spacecraft 1 on spacecraft 2 of a PLP pair is

$$\mathbf{f}_{12} = \frac{K}{r}\mathbf{r} \tag{2.9}$$

The potential function $\mathcal{V}_l$ producing this force is

$$\mathcal{V}_l = -Kr \tag{2.10}$$

While this force model has yet to be verified for large-separation distances, it represents a practical stand-in model for examining the algorithms developed in Chapters 5 and 6.

2.4 Magnetic Flux Pinning

MFP corresponds to a unique interaction that establishes a passively stable relative position and orientation between a high-temperature superconductor (HTSC) and magnetic field source. This equilibrium is established based on the system configuration at the time that the HTSC passes below its critical temperature. Hellman *et al.* describe a current-vortex model incorporating separation distance and superconductor thickness.[23] Tsuchimoto, Kojima, Takeuchi, and Honma describe the resulting vertical levitation force through numerical analysis.[24] Hull and Cansiz experimentally determined vertical and lateral forces of a test setup.[25] While the work described so far has examined forces produced by MFP, a torque relationship is also expected to establish an equilibrium relative orientation as well.

Kordyuk decomposes the MFP interaction by representing the imbedded magnetic field of the HTSC as the sum of two "image" dipoles.[26] One of these, termed the "mobile" image corresponds to the reflection of the magnetic dipole's current position and orientation over the HTSC plane. The second "static" image is the reflection of the opposite of the dipole moment and its position relative to the HTSC at the point when the HTSC passes below its critical temperature. Shoer and Peck experimentally verify the applicability of this model for close-proximity spacecraft operations.[27,28]

The locations and moments of these dipole images for use in Kordyuk's model relative to the HTSC are described by Fig. 2.2 and Eq. (2.11).

$$\boldsymbol{\mu}^* = \boldsymbol{\mu} - 2(\boldsymbol{\mu}\cdot\mathbf{n})\mathbf{n} \qquad \mathbf{r}^* = \mathbf{r} - 2(\mathbf{r}\cdot\mathbf{n})\mathbf{n} \qquad \boldsymbol{\rho}_1 = \mathbf{r} - \mathbf{r}^* = 2(\mathbf{r}\cdot\mathbf{n})\mathbf{n} \tag{2.11a}$$

$$\boldsymbol{\mu}_i^* = \boldsymbol{\mu}_i - 2(\boldsymbol{\mu}_i\cdot\mathbf{n})\mathbf{n} \qquad \mathbf{r}_i^* = \mathbf{r}_i - 2(\mathbf{r}_i\cdot\mathbf{n})\mathbf{n} \qquad \boldsymbol{\rho}_2 = \mathbf{r} - \mathbf{r}_i^* \tag{2.11b}$$

The force and torque between the HTSC and magnetic dipole can then be modeled as the sum of the interactions between the dipole pairs ($\boldsymbol{\mu}$, $\boldsymbol{\mu}^*$) and ($\boldsymbol{\mu}$, $-\boldsymbol{\mu}_i^*$) given by Eq. (2.5). In an effort to move to an energetic description of the interaction, this dissertation utilizes Eq. (2.12) as a candidate equation describing the potential energy associated with a flux pinning interface between a HTSC and magnetic dipole.

$$\mathcal{V}_{fp} = -\frac{1}{2}\boldsymbol{\mu}\cdot\mathbf{B}(\boldsymbol{\mu}^*,\boldsymbol{\rho}_1) + \boldsymbol{\mu}\cdot\mathbf{B}(\boldsymbol{\mu}_i^*,\boldsymbol{\rho}_2) \tag{2.12}$$

The use of this particular function is motivated by the potential energy associated with a dipole moment existing in a magnetic field given by (2.4). The first term accounts for the magnetic field generated by the 'mobile' dipole image , and the second term represents the interaction between the dipole and the field generated by the 'frozen' dipole image. The factor of 1/2 preceeding

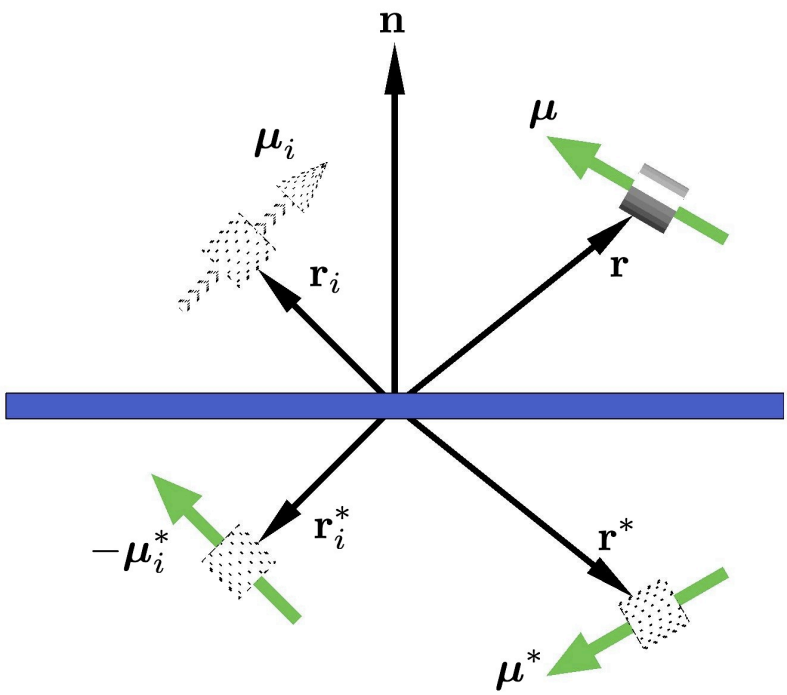

Figure 2.2: Layout of a semi-infinite HTSC and magnetic dipole for use in the image model of magnetic flux pinning. μ_i is included as a reference for defining the dipole μ_i^* and does not produce a magnetic field on its own.

the first term is associated with the fact that the effective separation between $\boldsymbol{\mu}^*$ and $\boldsymbol{\mu}$ is twice the distance between the HTSC surface and $\boldsymbol{\mu}$.

The vectors pointing between the images and the actual dipole locations have lengths and directions given by (2.13).

$$\rho_1 = 2\,(\mathbf{r}\cdot\mathbf{n}) \qquad \hat{\boldsymbol{\rho}}_1 = \mathbf{n} \tag{2.13a}$$

$$\rho_2 = \left(r^2 + r_i^2 - 2\mathbf{r}\cdot\mathbf{r}_i^*\right)^{1/2} \qquad \hat{\boldsymbol{\rho}}_2 = \boldsymbol{\rho}_2/\rho_2 \tag{2.13b}$$

Substituting the vector definitions of (2.11) and (2.13) into the individual

terms of (2.12) results in the energetic contributions of the two images to the flux pinning effect.

$$\begin{aligned}\mathcal{V}_1 &= -\frac{1}{2}\boldsymbol{\mu}\cdot\mathbf{B}\left(\boldsymbol{\mu}^*,\boldsymbol{\rho}_1\right)\\ &=\frac{\mu_0}{8\pi\rho_1^3}\left(\boldsymbol{\mu}^*\cdot\boldsymbol{\mu}-3\left(\boldsymbol{\mu}^*\cdot\hat{\boldsymbol{\rho}}_1\right)\left(\hat{\boldsymbol{\rho}}_1\cdot\boldsymbol{\mu}\right)\right)\\ &=\frac{\mu_0}{64\pi\left(\mathbf{r}\cdot\mathbf{n}\right)^3}\left(\mu^2+\left(\boldsymbol{\mu}\cdot\mathbf{n}\right)^2\right) \qquad (2.14a)\\ \mathcal{V}_2 &=\boldsymbol{\mu}\cdot\mathbf{B}\left(\boldsymbol{\mu}_i^*,\boldsymbol{\rho}_2\right)\\ &=\frac{\mu_0}{4\pi\rho_2^5}\left(\boldsymbol{\mu}_i^*\cdot\left(3\boldsymbol{\rho}_2\boldsymbol{\rho}_2-\rho_2^2\mathbb{I}\right)\cdot\boldsymbol{\mu}\right) \qquad (2.14b)\end{aligned}$$

Summing the terms described in (2.14) provide specific function to be evaluated as the potential energy function for a flux-pinned interface.

$$\mathcal{V}_{fp}=\frac{\mu_0}{4\pi}\left(\frac{\mu^2+\left(\boldsymbol{\mu}\cdot\mathbf{n}\right)^2}{16\left(\mathbf{r}\cdot\mathbf{n}\right)^3}+\frac{1}{\rho_2^5}\boldsymbol{\mu}_i^*\cdot\left(3\boldsymbol{\rho}_2\boldsymbol{\rho}_2-\rho_2^2\mathbb{I}\right)\cdot\boldsymbol{\mu}\right) \qquad (2.15)$$

Computing the forces and torques produced by (2.15) and comparing them to those produced directly by the image model verifies it as a valid potential function for flux pinning. These forces and torques correspond to the partial derivatives of the potential function with respect to a scalar coordinate. As (2.15) is naturally expressed as a function of vectors, the chain rule for differentiation provides a means to generate these necessary partial derivatives.

$$\frac{\partial}{\partial q_i}\mathcal{V}_{fp}=\frac{\partial\mathcal{V}_{fp}}{\partial\mathbf{n}}\cdot\frac{\partial\mathbf{n}}{\partial q_i}+\frac{\partial\mathcal{V}_{fp}}{\partial\mathbf{r}}\cdot\frac{\partial\mathbf{r}}{\partial q_i}+\frac{\partial\mathcal{V}_{fp}}{\partial\boldsymbol{\rho}_2}\cdot\frac{\partial\boldsymbol{\rho}_2}{\partial q_i}+\frac{\partial\mathcal{V}_{fp}}{\partial\boldsymbol{\mu}}\cdot\frac{\partial\boldsymbol{\mu}}{\partial q_i}+\frac{\partial\mathcal{V}_{fp}}{\partial\boldsymbol{\mu}_i^*}\cdot\frac{\partial\boldsymbol{\mu}_i^*}{\partial q_i} \qquad (2.16)$$

The vector partial derivatives of $\mathcal{V}_{fp}$ required to compute (2.16) are given in (2.17).

$$\frac{\partial}{\partial\mathbf{n}}\mathcal{V}_{fp}=\frac{\mu_0}{4\pi\left(2\mathbf{r}\cdot\mathbf{n}\right)^3}\left(\frac{\mu^2+\left(\boldsymbol{\mu}\cdot\mathbf{n}\right)^2}{2\mathbf{r}\cdot\mathbf{n}}\mathbf{r}+\left(\boldsymbol{\mu}\cdot\mathbf{n}\right)\boldsymbol{\mu}\right) \qquad (2.17a)$$

$$\frac{\partial}{\partial\mathbf{r}}\mathcal{V}_{fp}=-3\mu_0\frac{\mu^2+\left(\boldsymbol{\mu}\cdot\mathbf{n}\right)^2}{4\pi\left(2\mathbf{r}\cdot\mathbf{n}\right)^4}\mathbf{n} \qquad (2.17b)$$

$$\frac{\partial}{\partial \boldsymbol{\rho}_2}\mathcal{V}_{fp} = \frac{3\mu_0}{4\pi\rho_2^5}\left(\left(\boldsymbol{\mu}_i^* \cdot \boldsymbol{\rho}_2\right)\boldsymbol{\mu} + \left(\boldsymbol{\rho}_2 \cdot \boldsymbol{\mu}\right)\boldsymbol{\mu}_i^* - \left(\boldsymbol{\mu}_i^* \cdot \left(\frac{5}{\rho_2^2}\boldsymbol{\rho}_2\boldsymbol{\rho}_2 - \mathbb{I}\right) \cdot \boldsymbol{\mu}\right)\boldsymbol{\rho}_2\right) \tag{2.17c}$$

$$\frac{\partial}{\partial \boldsymbol{\mu}}\mathcal{V}_{fp} = \frac{\mu_0}{4\pi}\left(\frac{\boldsymbol{\mu} + \left(\boldsymbol{\mu} \cdot \mathbf{n}\right)\mathbf{n}}{\left(2\mathbf{r} \cdot \mathbf{n}\right)^3} + \frac{3\left(\boldsymbol{\mu}_i^* \cdot \boldsymbol{\rho}_2\right)}{\rho_2^5}\boldsymbol{\rho}_2 - \frac{1}{\rho_2^3}\boldsymbol{\mu}_i^*\right) \tag{2.17d}$$

$$\frac{\partial}{\partial \boldsymbol{\mu}_i^*}\mathcal{V}_{fp} = \frac{\mu_0}{4\pi\rho_2^5}\left(3\left(\boldsymbol{\rho}_2 \cdot \boldsymbol{\mu}\right)\boldsymbol{\rho}_2 - \rho_2^2\boldsymbol{\mu}\right) \tag{2.17e}$$

The remaining partial derivatives of the vectors producing $\mathcal{V}_{fp}$ with respect to the coordinate q_i are problem-specific and rely upon the choice of coordinates.

CHAPTER 3

LINEARIZED DYNAMICS AND CONTROL OF TWO FLUX-PINNED SPACECRAFT

Spacecraft formations typically have to rely upon active control methods to maintain stable configurations. This requirement imposes an associated cost on the satellite through fuel expenditure, actuator mass, and computation time for the controller. This paper proposes utilizing the flux-pinning interaction between a high-temperature superconductor and a magnetic field as a means to reduce these costs by passively stabilizing the dynamics governing the relative motion between spacecraft. A simplified model of a flux-pinned spacecraft formation is developed to provide the framework for future analysis. Linearization of this model about an equilibrium state allows for the development of a state-feedback control law. This framework is then applied to a simplified two-spacecraft formation in a nominally circular orbit about a central body and controlled to two distinct equilibrium separations.

3.1 Nomenclature

A State matrix of linearized system

B Input matrix of linearized system

$\mathcal{B}$ Frame in which the unit vectors $\mathbf{b}_1$, $\mathbf{b}_2$, and $\mathbf{b}_3$ are fixed

C Linear damping coefficient of $\dot{\rho}$

d_0 Field-cooled separation between magnetic dipole and high-temperature superconductor surface

δ_i Radius of i^{th} spacecraft

The content of this chapter was published as "A Simplified Model of a Flux-Pinned Spacecraft Formation" in the *Journal of Guidance, Control, and Dynamics* in 2010 (Ref. 29).

$\mathbf{F}_i$	Generalized active force associated with i^{th} partial velocities
$\mathbf{F}_i^*$	Generalized inertia force associated with i^{th} partial velocities
$f(\rho, \dot{\rho})$	Internal forcing between two spacecraft acting along $\mathbf{b}_1$
K	LQR controller gain matrix
m_i	Mass of i^{th} spacecraft
μ	Standard gravitational parameter for the central body
μ_0	Permeability of free space
μ_{FP}	Magnetic moment of dipole in a flux-pinning connection
$\mathcal{N}$	Inertial frame
$\boldsymbol{\omega}$	Angular velocity vector of $\mathcal{B}$ with respect to $\mathcal{RSW}$
Ω	Orbital mean motion of the center of mass on a circular orbit about central body
P_i	Center of mass of i^{th} spacecraft
q_i	i^{th} generalized coordinate
r_{cm}	Distance between formation center of mass and central body
ρ_i	Distance between i^{th} spacecraft's center of mass, P_i, to the formation center of mass
r_i	Distance between P_i and central body
$\mathbf{R}_i$	Resultant of forces applied to i^{th} spacecraft
$\mathcal{RSW}$	Frame rotating with the formation center of mass with fixed unit vectors **r**, **s**, and **w**
θ_1	Angle between unit vector $\hat{\mathbf{s}}$ and $\mathbf{b}_2$ about $\hat{\mathbf{w}}$
θ_2	Angle between unit vector $\hat{\mathbf{w}}$ and $\mathbf{b}_3$ about $\mathbf{b}_1$
u_i	i^{th} generalized speed
$\mathbf{v}_i^{P_j}$	The i^{th} partial velocity of P_j in $\mathcal{N}$

3.2 Introduction

By dividing a task between spatially separated modules, a given mission stands to obtain increased performance and mission lifespan. The concept of utilizing formations to affect these gains has already found utility in applications ranging from urban search and rescue operations to space-based observational platforms. Employing several robotic agents in a search and rescue operation not only increases the observational capacity of the operation but also has demonstrated an increase in human performance and communication, suggesting a hybrid team of humans and multiple vehicles coordinating to complete the task.[30] One of the more prominent examples of a planned space-based formation is that of the Terrestrial Planet Finder (TPF). The TPF aims to create an effective observational platform by combining data from several spacecraft in formation to synthesize an image that would otherwise require a much larger monolithic spacecraft to collect.[31] The DARPA F6 program has further enhanced the interest and visibility of spacecraft formations by encouraging research in areas such as communication networking, close- and long-range formation flight, and collision avoidance in formation flight.[2] Spacecraft formations also introduce opportunities for modularization and reduced total system weight through the removal of mechanical linkages. These advantages in turn likely reduce launch costs, extend system life, and simplify component repair procedures.

One of the specific challenges that spacecraft formation flight poses is that of relative motion control. Gravitational and environmental effects tend to disperse uncontrolled and dynamically unlinked spacecraft, requiring either a control input to the system or additional dynamics linking the states of

the vehicles together in a manner to maintain formation integrity. Specific solutions to the control aspect of this problem focus on the development of state-feedback controllers based on model linearization or suitable nonlinear controls schemes.[5,32–35] Most of these solutions require constant or periodic actuation of the system, translating into an increased mission cost through fuel expenditure and computational time. These penalties suggest instead the addition of dynamics to the system to create the desired formation. Most of the concepts in this area focus on utilizing electromagnetic effects to couple the states of spatially separated spacecraft together, effectively adding dynamics to the system without requiring a physical linkage between the vehicles. One concept proposes the creation of a virtual coulomb structure where each spacecraft is given a charge, resulting in electrostatic attraction and repulsion.[8] Another similar concept focuses on electrically-charged spacecraft formations in orbit about a central body with a magnetic field.[36] In this case, the vehicles utilize the Lorentz force to change their orbital velocity to match that of the formation. The attraction between electromagnets has also been studied for application to long-range formation flight.[17] While these solutions do add dynamics to the system in order to create a multi-vehicle formation, Earnshaw's Theorem still requires active control of any electromagnetically interacting system attempting to maintain relative position or follow an arbitrary path.[37] As a result, a controller still needs to be developed to regulate the formation shape in these solutions.

The flux pinning effect that occurs between a magnetic field and a high temperature superconductor (HTSC) sidesteps this issue by instead being characterized by the change of magnetic flux through the HTSC surface rather than straight electromagnetic attraction, making it an attractive candidate

for creating static connections between spacecraft or complete non-contacting kinematic mechanisms.[28,38] While the dependence of a flux-pinned interface upon the change in magnetic flux through a surface places limitations on effective range of the connection, many formation tasks, such as docking, are based on the close-proximity of the relevant vehicle. In order to analyze a formation tied together with flux pinning interfaces, we first need to adopt an appropriate mathematical model of the interaction and integrate it with a dynamics model of the formation.

3.3 Model Setup

Flux pinning refers to the interaction between a magnetic field and a HTSC. Motion of the magnetic field induces current vortices inside the HTSC, which then react to changes in the magnetic flux passing through the HTSC surface and establish passively stable relative separation and attitude between HTSC and magnetic field source. The electrical resistance within the HTSC is negligible under appropriate temperature conditions, so these vortices persist for extended periods of time. Creating an accurate physics-based model of this interaction between these vortices and the original magnetic field represents a dauntingly complex task. Several groups have worked on creating models based on approximations or around specific setups.[24,25,39–41] Kordyuk proposed a particularly general model of the flux pinning effect termed the frozen image model. This model approximates the magnetic field due to sources inside the HTSC as the sum of two fields based on the current relative position and the field-cooled relative position of the field with respect to the HTSC surface.[26]

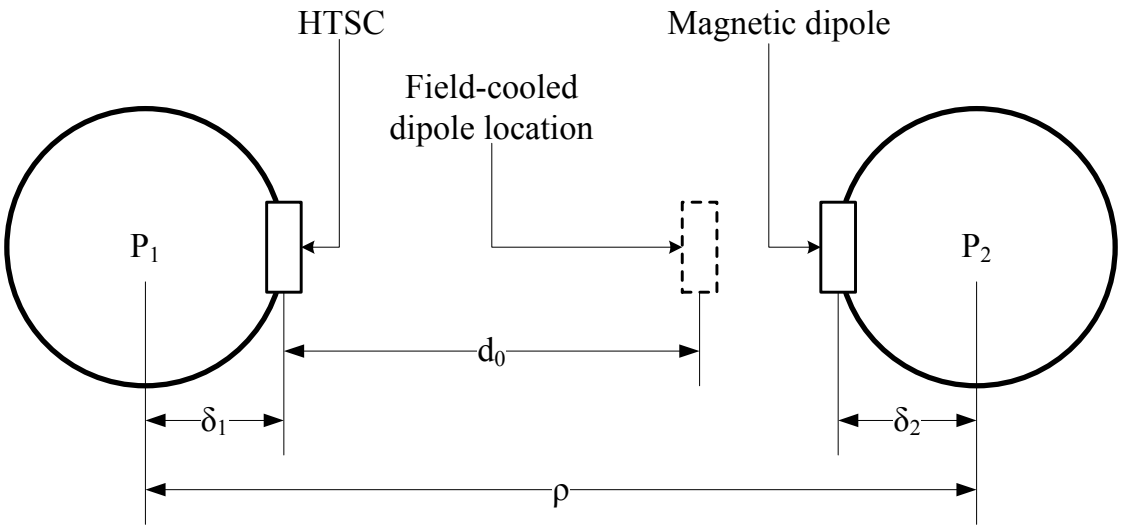

Figure 3.1: A depiction of the relevant distances associated with the simplified image model. The force is assumed to always act along a vector pointing between P_1 and P_2 and produce no internal torques between the spacecraft.

Figure 3.1 describes the general setup of the image model for this analysis. Two assumptions serve to simplify the forcing model: assuming the magnetic dipole vector is parallel to one pointing between the centers of mass P_1 and P_2 of the spacecraft and that the force is applied over the minimal separation distance between the spacecraft surfaces removes any torque interactions due to flux pinning. Furthermore, assuming spherical spacecraft of radii δ_1 and δ_2 with uniform mass distributions allows for simple determination of the separation between the magnetic dipole and HTSC surface. As neither gravity nor flux pinning will result in a torque applied to the individual spacecraft, the attitudes of the two spacecraft will not vary. This reduces the number of states for consideration while still allowing some fidelity in the dynamics governing the relative separation between the vehicles. While not examined explicitly in the context of orbiting bodies, experimental observations by Shoer and

Peck demonstrate effectively rotational stiffness and damping between a flux-pinned HTSC and magnetic dipole pair for small angle perturbations, implying inherent disturbance rejection capabilities and passive attitude stability for appropriate separation distances.[28]

The internal force produced by flux pinning under the image model depends upon the field-cooled separation d_0 of the setup: the distance between the magnetic field source and the HTSC when the HTSC is initially chilled to its superconducting state. The damping associated with flux pinning depends upon the HTSC properties, and can be modified to some extent by introducing eddy current damping by placing some aluminum near the HTSC. Shoer and Peck observe that in cases where the magnetic field source and HTSC remain in the vicinity of their field-cooled locations, the damping due to flux pinning is approximately linear.[28] With the separation between P_1 and P_2 described as ρ, a simplified version of Kordyuk's image model with damping takes the following form:

$$f(\rho, \dot{\rho}) = \frac{3\mu_0 \mu_{FP}^2}{2\pi} \left(\frac{1}{(\rho - \delta_1 - \delta_2 + d_0)^4} - \frac{1}{16(\rho - \delta_1 - \delta_2)^4} \right) + C\dot{\rho} \tag{3.1}$$

It should be noted that utilizing an adapted version of Kordyuk's image model comes with the inherent assumptions of a flat, ideal superconductor and that the field penetration depth is much less than the system's characteristic dimension.[26] These assumptions place some effective limitations on the separation distances for a dipole and superconductor pair over which this force model would be a valid approximation. As the force rapidly decreases with increased separation between the HTSC surface and the dipole, flux pinning would only be appropriate for extremely close-range applications. Shoer and Peck demonstrate this model's viability for their experimental setup for

separations up to 10 cm.[28]

3.4 Relative Motion Formulation

We are interested in examining the dynamics of a flux-pinned connection between vehicles in orbit. Developing a set of equations of motion describing the relative motion of two spherical spacecraft in near-circular orbits is the first step towards analyzing the stability of this simple setup and forms the basis for examining the properties of systems of greater complexity.

Under the assumption that the formation center of mass travels on a circular orbit, we need three generalized coordinates to capture the relative motion of P_1 and P_2. Coordinates ρ, θ_1, and θ_2, as shown in Fig. 3.2, completely and uniquely describe the range of possible configurations of the system where θ_1 and $-\theta_2$ constitute a 3-2 Euler angle sequence:

$$q = \begin{bmatrix} q_1 \\ q_2 \\ q_3 \end{bmatrix} = \begin{bmatrix} \theta_1 \\ \theta_2 \\ \rho \end{bmatrix} \tag{3.2}$$

This same circular orbit assumption defines the angular velocity of frame $\mathcal{RSW}$ relative to the inertial frame $\mathcal{N}$ as a vector with constant magnitude Ω and direction $\mathbf{w}$. We choose generalized speeds as the vector measures of the inertial time derivative of the vector $\boldsymbol{\rho}$ pointing between P_1 and P_2 in terms of $\mathbf{b}_1$, $\mathbf{b}_2$, and $\mathbf{b}_3$.

$$\begin{bmatrix} u_1 \\ u_2 \\ u_3 \end{bmatrix} = \begin{bmatrix} 0 & 0 & 1 \\ c_2 q_3 & 0 & 0 \\ 0 & q_3 & 0 \end{bmatrix} \begin{bmatrix} \dot{q}_1 \\ \dot{q}_2 \\ \dot{q}_3 \end{bmatrix} + \begin{bmatrix} 0 \\ \Omega c_2 q_3 \\ 0 \end{bmatrix} \text{ where } c_2 = \cos q_2 \tag{3.3}$$

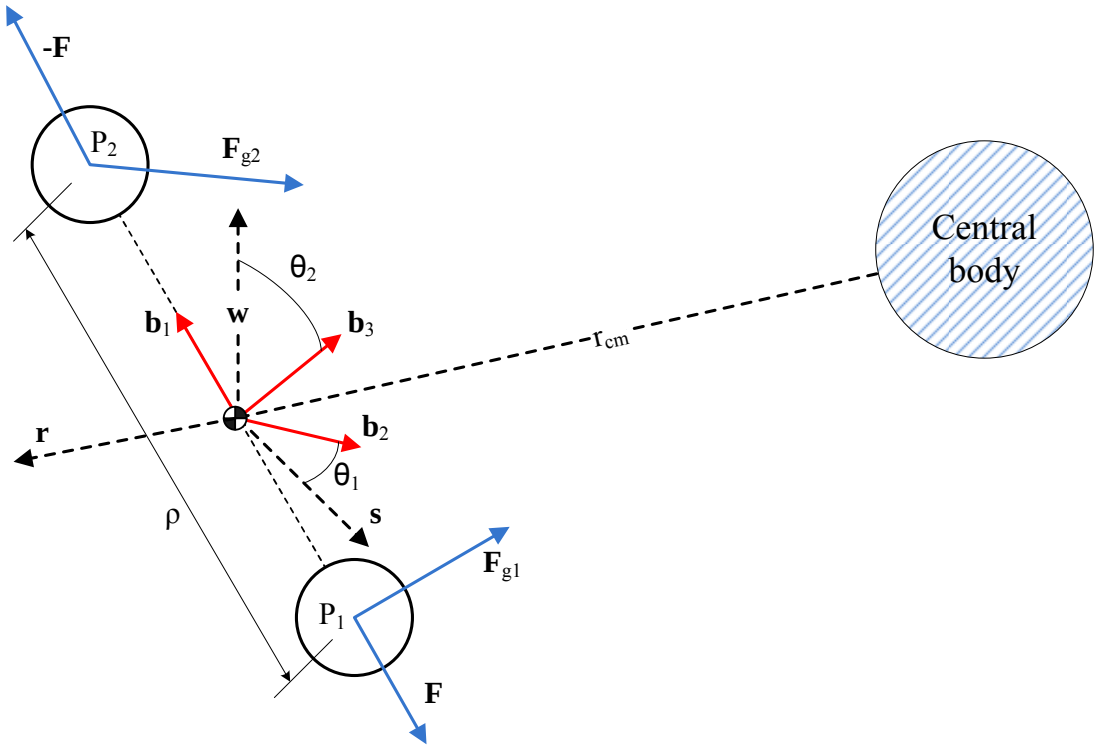

Figure 3.2: The layout of the system modeled. ρ, θ_1, and θ_2 describe the configuration of the system relative to the system center of mass, assumed to travel on a circular orbit.

Solving for the time derivative of the generalized coordinates,

$$\begin{bmatrix} \dot{q}_1 \\ \dot{q}_2 \\ \dot{q}_3 \end{bmatrix} = \begin{bmatrix} 0 & 1/c_2 q_3 & 0 \\ 0 & 0 & 1/q_3 \\ 1 & 0 & 0 \end{bmatrix} \begin{bmatrix} u_1 \\ u_2 \\ u_3 \end{bmatrix} - \begin{bmatrix} \Omega \\ 0 \\ 0 \end{bmatrix} \tag{3.4}$$

The two spacecraft considered in this analysis are under the influence of the gravitational attraction to a central body and an internal force acting between the two vehicles. With the choice of generalized coordinates and speeds from Eqs. (3.2) and (3.3), applying these forces to the system results in the following equations of motion:

$$\dot{u}_1 = \frac{1}{q_3}\left(u_2^2 + u_3^2\right) - \mu\left(r_{cm} c_1 c_2 \left(\frac{1}{r_2^3} - \frac{1}{r_1^3}\right) + \frac{q_3}{M}\left(\frac{m_1}{r_2^3} + \frac{m_2}{r_1^3}\right)\right) \tag{3.5a}$$

$$- \frac{M}{m_1 m_2} f(q,u)$$

$$\dot{u}_2 = -\frac{1}{q_3}(u_1 - t_2 u_3)\, u_2 + \mu r_{cm} s_1 \left(\frac{1}{r_2^3} - \frac{1}{r_1^3}\right) \tag{3.5b}$$

$$\dot{u}_3 = -\frac{1}{q_3}\left(u_1 u_3 + t_2 u_2^2\right) + \mu r_{cm} c_1 s_2 \left(\frac{1}{r_2^3} - \frac{1}{r_1^3}\right) \tag{3.5c}$$

where $c_1 = \cos q_1$, $t_2 = \tan q_2$, $M = m_1 + m_2$, r_{cm} is the constant radius of the formation center of mass' orbit, and r_1 and r_2 are functions of the generalized coordinates that describe the scalar radial distance of P_1 and P_2 to the central body. Appendix A derives in detail Eqs. (3.5a), (3.5b), and (3.5c). Together, Eqs. (3.4), (3.5a), (3.5b), and (3.5c) fully describe the nonlinear dynamics of the model. These equations depend upon the system conforming to the assumptions inherent in the flux pinning model and the magnetic dipole having a negligible interaction with the ambient magnetic field. It should be noted that the representation of the equations of motion is dependent upon the variables chosen. While an alternate set of equations may have more compact representations, our choice of u_1, u_2, and u_3 provide intuitive insight to the motion of the separation vector relative to a frame rotating with the formation in terms of Cartesian coordinates.

3.5 Linearized System

The effects of the gravity-gradient torque applied across the two spacecraft establishes an equilibrium orientation of the formation and in tandem with the inter-vehicle force $\mathbf{F}$ defines an equilibrium separation distance. These conditions correspond to the following nominal generalized coordinates and

speeds

$$\bar{q} = \begin{bmatrix} \bar{q}_1 \\ \bar{q}_2 \\ \bar{q}_3 \end{bmatrix} = \begin{bmatrix} 0 \\ 0 \\ \rho_0 \end{bmatrix} \text{ and } \bar{u} = \begin{bmatrix} \bar{u}_1 \\ \bar{u}_2 \\ \bar{u}_3 \end{bmatrix} = \begin{bmatrix} 0 \\ \Omega\rho_0 \\ 0 \end{bmatrix} \tag{3.6}$$

which, in combination with setting $\dot{\bar{q}} = 0$ and $\dot{\bar{u}} = 0$ as required for an equilibrium and a nominal dipole moment $\bar{\mu}_{FP}$ satisfy Eqs. (3.5a), (3.5b), and (3.5c). Considering perturbations to the state q^*, and u^*, and to the control input μ^*_{FP} from the solution $\bar{q}$, $\bar{u}$, and $\bar{\mu}_{FP}$, we can form the linearized equations of motion about the equilibrium point based on Eq. (A.26)):

$$\dot{q}_1^* = \frac{1}{\rho_0} u_2^* - \frac{\Omega}{\rho_0} q_3^* \tag{3.7a}$$

$$\dot{q}_2^* = \frac{1}{\rho_0} u_3^* \tag{3.7b}$$

$$\dot{q}_3^* = u_1^* \tag{3.7c}$$

$$\begin{aligned} \dot{u}_1^* = &\left[\frac{\mu}{M} \left(3r_{cm}^2 \left(\frac{m_1}{\bar{r}_2^5} + \frac{m_2}{\bar{r}_1^5} \right) + \frac{m_1}{\bar{r}_2^3} \left(1 + 3 \left(\frac{m_1\rho_0}{M\bar{r}_2} \right)^2 \right) \right. \right. \\ &\left. \left. + \frac{m_2}{\bar{r}_1^3} \left(1 + 3 \left(\frac{m_2\rho_0}{M\bar{r}_1} \right)^2 \right) \right) - \Omega^2 - \frac{M}{m_1 m_2} \frac{\partial f}{\partial q_3} \right] q_3^* - \frac{M}{m_1 m_2} C u_1^* + 2\Omega u_2^* \\ &- \frac{3M\mu_0 \bar{\mu}_{FP}}{m_1 m_2 \pi} \left(\frac{1}{(\rho_0 - \delta_1 - \delta_2 + d_0)^4} - \frac{1}{16\,(\rho_0 - \delta_1 - \delta_2)^4} \right) \mu_{FP}^* \end{aligned} \tag{3.7d}$$

$$\dot{u}_2^* = \mu r_{cm} \left(\frac{1}{\bar{r}_2^3} - \frac{1}{\bar{r}_1^3} \right) q_1^* - \Omega u_2^* \tag{3.7e}$$

$$\dot{u}_3^* = \left(\mu r_{cm} \left(\frac{1}{\bar{r}_2^3} - \frac{1}{\bar{r}_1^3} \right) - \Omega^2 \rho_0 \right) q_2^* \tag{3.7f}$$

Setting the time derivatives of the generalized coordinates and speeds to zero in Eqs. (3.3), (3.5a), (3.5b), and (3.5c) produces a set of equations which define states of equilibrium about which a linearization of the system can occur. Setting the angles θ_1 and θ_2 to zero as in Eq. (3.6) corresponds to a gravity gradient stabilized orientation of the formation and satisfies the equilibrium condition for Eqs. (3.5b) and (3.5c). However, substituting these values

into Eq. (3.5a) reveals that there are potentially more than one equilibrium separation distance between the two vehicles in orbit. This result arises from the flux pinning interaction working in tandem with the effect of gravitational attraction to the central body. It should be noted that these equilibrium locations strongly depend upon the system satisfying the assumptions of Kordyuk's image model.[26] Figure 3.3 graphs the $\bar{\mu}_{FP}$ required to establish a given surface

Table 3.1: Example parameters for linearization and simulation

Parameter	Value	
m_1	100	kg
m_2	100	kg
δ_1	0.3	m
δ_2	0.3	m
d_0	0.02	m
μ_{FP}	0.2212	J/T
C	1	N-s/m
Orbit altitude	600	km

separation and field-cooled separation between the HTSC and dipole. The zero-crossings of Fig. 3.4) are the equilibrium separation distances in a specific case corresponding to the parameters in Table 3.1.

3.6 Simulation and Control

One possible use of the linearized model described in the previous section is the development of a state-feedback controller. Continuing to use the parameters from Table 3.1 and linearizing about an equilibrium state associated with a

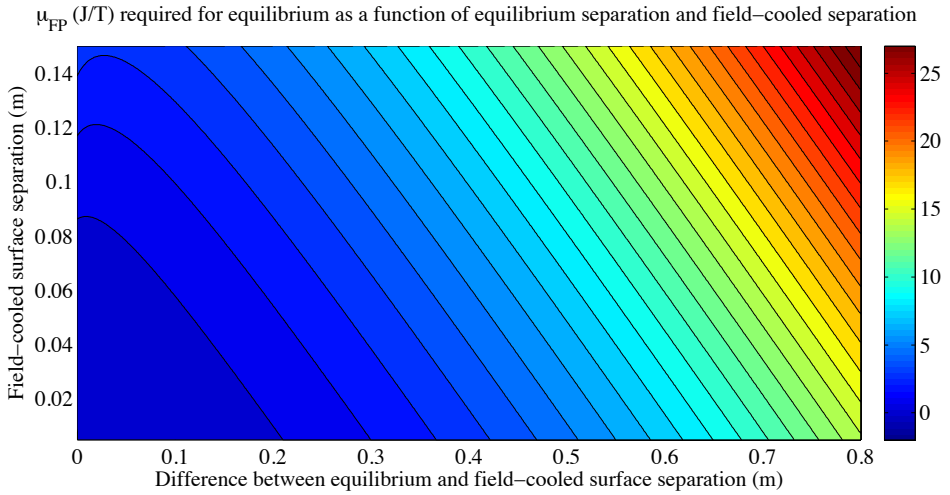

Figure 3.3: $\bar{\mu}_{FP}$ (J/T) required to establish a given equilibrium separation with a given field-cooled HTSC-dipole separation d_0.

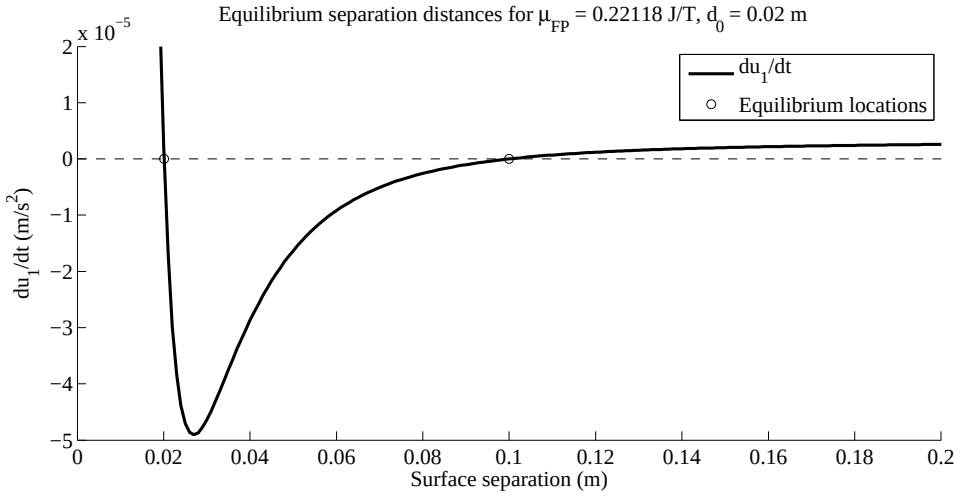

Figure 3.4: Finding the zeros of $\dot{u}_1$ defines the equilibrium separation distances for a particular setup. Note the horizontal axis is in terms of surface separation, $\rho - \delta_1 - \delta_2$. In this case, using the parameters from Table 3.1 locates the equilibrium separation between P_1 and P_2 at distances of 0.6201 m and 0.7000 m.

nominal separation distance found from Fig. 3.4 creates a state space model of the linearized system. Applying LQR control synthesis to this linear system creates a basic linear state-feedback control law of the form

$$\mu_{FP} = -K \begin{bmatrix} q^* \\ u^* \end{bmatrix} + \bar{\mu}_{FP} \tag{3.8}$$

where $\bar{\mu}_{FP}$ is the input required to establish the desired equilibrium separation. This constant input could be provided by either a permanent magnet or electromagnetic source.

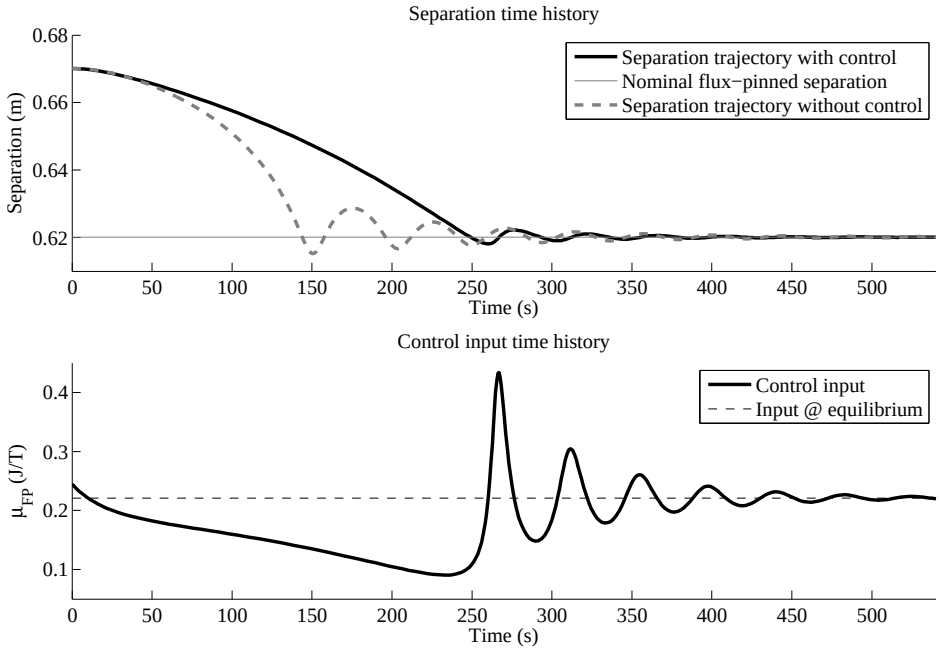

Figure 3.5: Time history of the separation distance between P_1 and P_2 given parameters described in Table 3.1 for both an uncontrolled and state-feedback controlled response to the same initial condition. *Top*: Separation time history between P_1 and P_2. *Bottom*: Control input time history of μ_{FP}. The desired equilibrium state is described in Eq. (3.9).

Figure 3.5 depicts the separation time history of the two spacecraft described

by the parameters in Table 3.1 resulting from an initial displacement from the equilibrium state both with and without a state-feedback controller. In this case, the desired equilibrium state corresponds to

$$\bar{q} = \begin{bmatrix} 0.0 \text{ rad} \\ 0.0 \text{ rad} \\ 0.6201 \text{ m} \end{bmatrix}, \bar{u} = \begin{bmatrix} 0.0 \\ 0.0006717 \\ 0.0 \end{bmatrix} \text{ m/s, and } \bar{\mu}_{FP} = 0.2212 \text{ J/T} \tag{3.9}$$

and the control law chosen is encapsulated in the gain matrix K in Eq. (3.8)

$$K = \begin{bmatrix} 0.003317 & 0.0 & -0.4607 & -435.4 & -0.03819 & 0.0 \end{bmatrix} \tag{3.10}$$

The large-magnitude fourth component of K corresponds to the perturbation u_1^* and effectively adds damping to the system, reducing the frequency of the oscillations compared to the uncontrolled case. Examining the eigenvalues of the A matrix defined in Eq. (A.26) and of $A - BK$ for the controlled system determines the stability of the linearized dynamics. The eigenvalues for the uncontrolled and state-feedback controlled systems linearized about Eq. (3.9) and the gain matrix K from Eq. (3.10) are given in Table 3.2. The lack of

Table 3.2: Sample linear system eigenvalues about marginally stable equilibrium

Open-Loop Eigenvalues	Closed-Loop Eigenvalues
$-3.379 \cdot 10^{-10} + 0.001876$ i	$-5.826 \cdot 10^{-9} + 0.001876$ i
$-3.379 \cdot 10^{-10} - 0.001876$ i	$-5.826 \cdot 10^{-9} - 0.001876$ i
$-.001000 + 0.1483$ i	$-0.01443 + 0.1479$ i
$-.001000 - 0.1483$ i	$-0.01443 - 0.1479$ i
$0 + 0.002166$ i	$0 + 0.002166$ i
$0 - 0.002166$ i	$0 - 0.002166$ i

positive real components of the eigenvalues for either A or $A - BK$ in Table 3.2 indicates neither linear system is unstable. The final two eigenvalues with

real components equal to zero, however, imply marginal stability for the linear system, which leaves the overall stability of the nonlinear system undetermined. The modes associated with these eigenvalues correspond to the out-of-plane motions of the system described by the θ_2 coordinate and its time derivative, $\dot{\theta}_2$, which are known to act similar to a simple harmonic oscillator in the absence of perturbations.

The second equilibrium point found in Fig. 3.4 represents an opportunity to command the system in such a way as to maintain a separation distance significantly farther away than the nominal flux-pinned separation. In this specific case, the second equilibrium state corresponds to

$$\bar{q} = \begin{bmatrix} 0.0 \text{ rad} \\ 0.0 \text{ rad} \\ 0.7000 \text{ m} \end{bmatrix}, \bar{u} = \begin{bmatrix} 0.0 \\ 0.0007583 \\ 0.0 \end{bmatrix} \text{ m/s, and } \bar{\mu}_{FP} = 0.2212 \text{ J/T} \tag{3.11}$$

Linearizing about this equilibrium state, we can again develop a state-feedback control law:

$$K = \begin{bmatrix} 0.1277 & 0.0 & -35.47 & -1097 & -97.37 & 0.0 \end{bmatrix} \tag{3.12}$$

Table 3.3 lists the eigenvalues of the controlled and uncontrolled linear system about this equilibrium state. The positive real component of one of the eigenvalues of the uncontrolled system indicates that without control, the system is unstable. This eigenvalue is associated with a combined motion of ρ and θ_1. In the controlled system, however, we see that none of the eigenvalues has a positive real component, again implying marginal stability.

Figure 3.6 depicts a sample time history of ρ with and without the controller responding to non-equilibrium initial conditions. With the state-feedback control, the system reaches the nominal desired equilibrium value. Without

Table 3.3: Sample linear system eigenvalues about unstable equilibrium state

Open-Loop Eigenvalues	Closed-Loop Eigenvalues
$-0.02336 + 0\,\mathrm{i}$	$-0.02486 + 0.009544\,\mathrm{i}$
$0.003403 + 0\,\mathrm{i}$	$-0.02486 - 0.009544\,\mathrm{i}$
$-1.988 \cdot 10^{-5} + 0.001920\,\mathrm{i}$	$-6.144 \cdot 10^{-6} + 0.001877\,\mathrm{i}$
$-1.988 \cdot 10^{-5} - 0.001920\,\mathrm{i}$	$-6.144 \cdot 10^{-6} - 0.001877\,\mathrm{i}$
$0 + 0.002166\,\mathrm{i}$	$0 + 0.002166\,\mathrm{i}$
$0 - 0.002166\,\mathrm{i}$	$0 - 0.002166\,\mathrm{i}$

it, however, the system drifts away from the prescribed equilibrium separation, as predicted in the eigenvalues of Table 3.3.

3.7 Conclusion

Flux pinning has the potential to passively stabilize the relative motion of individual non-contacting components in a generalized system. In order to demonstrate some of the properties of a flux-pinned system, we created a simplified model of a two-craft formation in a nominally circular orbit. The flux pinning interaction between the spacecraft in combination with the effects of gravitational attraction to a common central body establish dynamic equlibria. While the effects of the gravity gradient torque acting across the two vehicles establish the equilibrium of the attitude states, some parameter choices describing the flux-pinning connection have the potential to establish two equilibrium separation distances.

The first equilibrium separation is typically close to the field-cooled

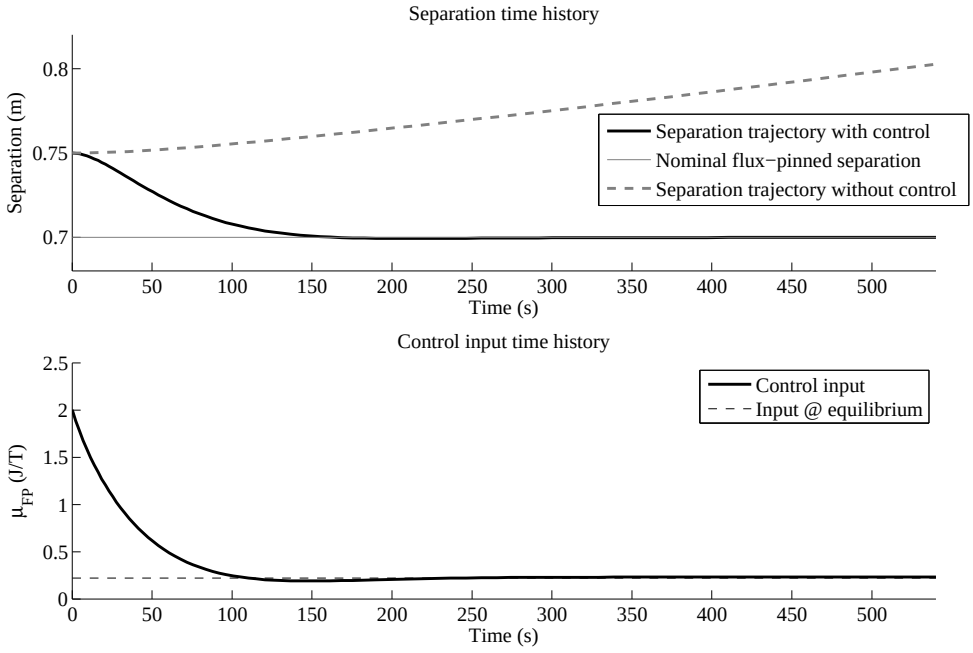

Figure 3.6: Time history of the separation distance between P_1 and P_2 given parameters described in Table 3.1 for both an uncontrolled and state-feedback controlled response to the same initial condition. *Top*: Separation time history between P_1 and P_2. *Bottom*: Control input time history of μ_{FP}. The desired equilibrium state is described in Eq. (3.11).

separation and appears to be asymptotically stable with respect to the vehicle separation but marginally stable in some of the attitude motions. These stability properties are analogous to the effects of the gravity gradient torque on a rigid body. The second equilibrium separations are farther away than the field-cooled separation and appear to be unstable in the absence of control. These additional, more distant equilibria are created by the interaction between the internal force due to flux pinning and the effects of gravitational attraction to the central body. By implementing a simple linear state-feedback control law about these additional equilibrium states, we maintain separations between the

vehicles greater than the field-cooled separations established with the cooling of HTSC.

The mathematical framework developed provides a basis for modeling more complex formations and for linear analysis of this particular model. The flux pinning forcing function utilized is a simplification of a complicated interaction with several active alternative descriptions with a variety of assumptions. The simplifications to our flux pinning model effectively negate the torque interaction between the vehicles. In combination with the spherical spacecraft assumption, the lack of internal torques allows us to ignore the relative attitude between the vehicles and focus instead on the relative position of the two spacecraft. While the uncontrolled separation trajectories simulated in the paper suggest that flux-pinned vehicles in orbit form passively stable arrangements, they do not definitively prove that to be the case.

CHAPTER 4

NATURAL RESPONSE OF A RING FORMATION OF FLUX-PINNED VEHICLES

4.1 Nomenclature

C_r	Rotational damping coefficient
C_t	Translational damping coefficient
$\mathbf{d}$	Position vector relative to formation center of mass
$\mathbf{f}$	A vector representing an applied force
$\mathbf{I}$	Inertia dyadic
J	Cost function
m	Vehicle mass
$\boldsymbol{\mu}$	Vector representation of a magnetic dipole moment
$\boldsymbol{\mu}_0$	Vacuum permeability
n	Number of vehicles
$\hat{\mathbf{n}}$	Unit vector normal to ideal formation plane
$\hat{\mathbf{n}}_{HTSC}$	Unit vector normal to high-temperature superconductor (HTSC) surface
$\boldsymbol{\omega}$	Angular velocity vector
$\mathbf{1}$	Identity dyadic
$\mathbf{r}$	Position vector
R	In-plane radial coordinate
$\boldsymbol{\rho}$	Position vector relative to HTSC
$\boldsymbol{\tau}$	A vector representing an applied torque
θ_i	In-plane angular separation between vehicle i and $i+1$

The content of this chapter was published as "Stationkeeping of a Flux-Pinned Satellite Network" in the *Journal of Guidance, Control, and Dynamics* in 2010 (Ref. 42).

$\mathbf{w}_\tau$ Input disturbance torque

$\mathbf{w}_f$ Input disturbance force

Z Out-of-plane displacement coordinate

4.2 Introduction

Satellite formations offer the promise of meeting requirements for space systems that must achieve large spatial extents, such as sparse-aperture telescopes. Physically separating components enables long-baseline observations without the weight associated with a truss support structure. Additionally, removing mechanical linkages between system elements also introduces opportunities for modularization. These advantages in turn likely reduce launch costs, extend system life, and simplify repair operations.[43] However, by removing these mechanical connections entirely, we eliminate a simple and effective means of constraining the relative position among components, a disadvantage that the present study addresses.

Proposed means of overcoming this disadvantage focus mainly on active control, augmenting the dynamics of the system through additional physics, or a combination of these two approaches. Through active control and independent inputs to the vehicles, a formation can maintain and modify relative positions and orientations of individual spacecraft, but typically necessitates near-constant or frequent actuation to counter environmental forces modifying the relative motion of the formation.[32,33,35] Natarajan and Schaub augment the natural dynamics of a two-vehicle formation in orbit by controlling the Coulomb force acting between electrically-charged spacecraft

and demonstrate the utility of such a control scheme for relative position maintenance.[12] Atchison and Peck propose specific types of formations made possible by using the Lorentz force on a charged object in orbit around a planet with a magnetic field as an input.[36] Ashun and Miller suggest a solution based on electromagnetic attraction among actively controlled magnetic fields.[44] The present study augments this list of possibilities by examining the feasibility of the flux-pinning effect between a magnetic field and a superconductor as a means of establishing an action-at-a-distance force. The primary advantage of using magnetic flux pinning over other approaches is that it creates a passively stable connection between two bodies, making active control of the relative spacecraft states an additional option instead of a necessity. Any solution based on magnetic attraction alone—whether achieved by permanent magnets or electromagnets—cannot be described as passively stable. As a consequence of Earnshaw's Theorem, active control is generally necessary for a system of magnetically interacting components to maintain relative position or follow an arbitrary path.[37] Conceptually, flux pinning sidesteps this issue by depending instead upon forces generated by current loops in the HTSC passively resisting change.

This reaction can be modeled as a multiple degree-of-freedom spring and damper with an equilibrium that corresponds to the pinned position and orientation relative to the source of a magnetic field.[27,28] In unactuated mechanical systems consisting of bodies interconnected by springs, masses, and dampers, the total energy of the system never increases, resulting in an asymptotically stable arrangement. By creating a similar arrangement in orbit, one can take advantage of this passively stable, flux-pinning effect to establish

a virtual structure that maintains relative position and orientation with reduced need for active control.

4.3 The Flux Pinning Effect

Motion of a magnetic field induces current vortices inside a high-temperature superconductor (HTSC), which then react to changes in the magnetic flux passing through the its surface.[23,45] The electrical resistance within the HTSC is negligible when the HTSC is below its so-called transition temperature. As a result, these vortices can persist indefinitely. This interaction establishes an equilibrium position and orientation of the magnetic field relative to the HTSC, in which perturbations are met with a restorative force. This force is hysteretic: its instantaneous direction and magnitude depend upon the history of relative movement.[41] For small motions, however, the flux-pinning reaction force resembles a linear, multiple degree-of-freedom spring-and-damper system. Small perturbations from the initial state result in reaction forces and torques characterized by stiffness and damping values derived by theory or experimentation.[41,45] One particularly important observation of flux-pinned magnet and superconductor pairs that can be verified through experiment is that there is no resistance to any rotation about an axis of symmetry in the magnet's magnetic field as such rotations do not change the flux passing through the HTSC surface.[28,45]

There are many approaches to finding force and torque expressions that have been presented in recent literature.[24,25,39–41,46] Approaching the force and torque interaction from an analytical point of view is often complicated

by a lack of a convenient manner in which to express the currents and their derivatives induced in the HTSC surface. Many of these analyses restrict motion to one degree of freedom, resulting in an absence in the literature of general, analytical expressions for the force and torque interaction required for analysis and simulation.

Kordyuk addresses this issue by developing a model of a magnet and semi-infinite superconductor pair that approximates the interaction through the sum of two conceptual magnetic fields embedded in the HTSC.[26] Figure 4.1 depicts the general concept of this model in the case of a magnetic dipole. This

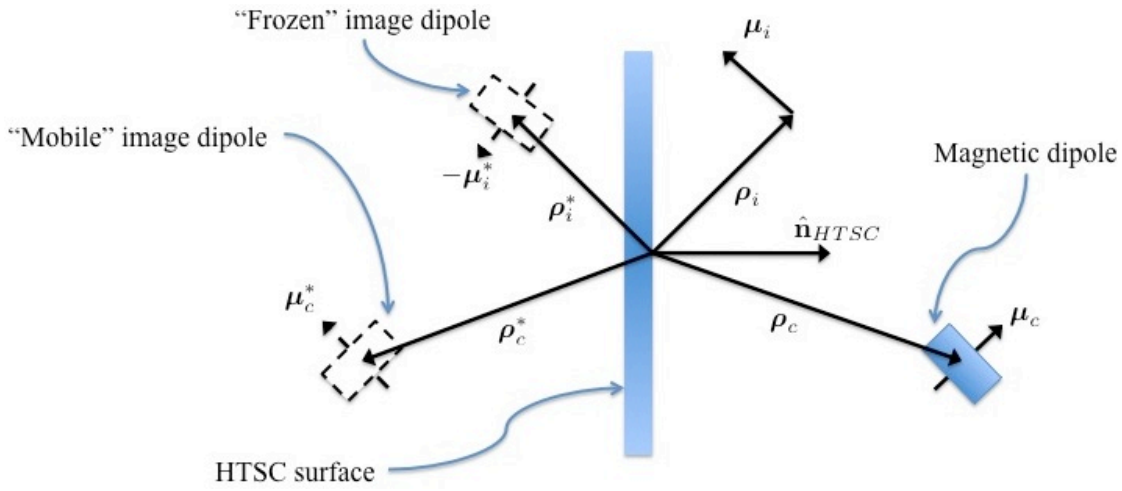

Figure 4.1: Image-dipole model of flux pinning. The frozen and mobile dipole images are representative of the induced external magnetic field of the HTSC. The real magnetic dipole interacts with this field to impart a non-contacting force and torque.

"image" model decomposes the external magnetic field of the HTSC into two components. The "frozen" image depends upon the magnetic field conditions when the HTSC passes its critical temperature. This process of cooling the superconductor in the presence of a magnetic field is termed "field-cooling."

The frozen image has a fixed position relative to the HTSC, $\boldsymbol{\rho}_i^*$, that corresponds to the reflection of the relative position of the field-cooled dipole, $\boldsymbol{\rho}_i$, over the HTSC surface. Its dipole moment vector, $-\boldsymbol{\mu}_i^*$, is the reflection of the opposite of the field-cooled dipole moment vector, $\boldsymbol{\mu}_i$, and is also fixed with respect to the HTSC. Similarly, the "mobile" image of the magnetic dipole has both a position $\boldsymbol{\rho}_c^*$ and dipole moment $\boldsymbol{\mu}_c^*$ corresponding to the reflections of the current relative position $\boldsymbol{\rho}_c$ and dipole moment vector $\boldsymbol{\mu}_c$ of the magnetic dipole over the HTSC surface. In combination, the magnetic fields generated by these two image dipoles establish a potential well that draws the permanent magnet back to its original field-cooled position and orientation.

This image model conveniently predicts forces and torques associated with a magnetic dipole interacting with a semi-infinite, planar HTSC suffering from no hysteresis or damping. As the magnetic field becomes more complex and the assumptions regarding the HTSC less applicable, the model suffers. However, Shoer and Peck demonstrate the validity of the image model supplemented by linear damping for predicting the stiffness of a low-mass magnet and superconductor pair for separation distances on the order of 10 cm.[27,28]

Shoer observes that in cases where the magnetic field source and HTSC remain in the vicinity of their field-cooled locations, the damping force and torque due to hysteresis and other physical effects as approximately linear.[27] As the damping force applied between the HTSC and magnetic field source is internal to the system and cannot change the angular momentum sum, it is assumed to act along the relative separation vector between the objects. We also know that for a symmetric field, such as that for a dipole, rotations cause no torque about the axis of symmetry. Therefore, the damping torque applied is

based on the relative angular velocity of the two objects projected onto a plane normal to the dipole moment vector. The damping coefficients of the interaction can be modified by the introduction of additional material, such as aluminum, to induce eddy current damping.[27]

Combining these damping effects with the magnetic dipole interactions with the frozen and mobile dipole images results in the completed force and torque interaction description between the HTSC and magnetic dipole:[16]

$$\mathbf{f}_m = \mathbf{f}(\boldsymbol{\rho}_c - \boldsymbol{\rho}_i^*, \boldsymbol{\mu}_c, -\boldsymbol{\mu}_i^*) + \mathbf{f}(\boldsymbol{\rho}_c - \boldsymbol{\rho}_c^*, \boldsymbol{\mu}_c, \boldsymbol{\mu}_c^*) - C_t \frac{\boldsymbol{\rho}_c \boldsymbol{\rho}_c}{\boldsymbol{\rho}_c \cdot \boldsymbol{\rho}_c} \cdot \dot{\boldsymbol{\rho}}_c \tag{4.1a}$$

$$\mathbf{f}_h = -\mathbf{f}_m \tag{4.1b}$$

$$\boldsymbol{\tau}_m = \boldsymbol{\tau}(\boldsymbol{\rho}_c - \boldsymbol{\rho}_i^*, \boldsymbol{\mu}_c, -\boldsymbol{\mu}_i^*) + \boldsymbol{\tau}(\boldsymbol{\rho}_c - \boldsymbol{\rho}_c^*, \boldsymbol{\mu}_c, \boldsymbol{\mu}_c^*) - C_r \left(\mathbf{1} - \frac{\boldsymbol{\mu}_c \boldsymbol{\mu}_c}{\boldsymbol{\mu}_c \cdot \boldsymbol{\mu}_c}\right) \cdot \boldsymbol{\omega}_{rel} \tag{4.1c}$$

$$\boldsymbol{\tau}_h = -\boldsymbol{\tau}_m - \boldsymbol{\rho}_c \times \mathbf{f}_m \tag{4.1d}$$

Equation (4.1) depends upon the force and torque interactions between two magnetic dipoles. These relations are given in Landecker[16] in terms of arbitrary vectors $\boldsymbol{\rho}$, $\boldsymbol{\mu}_a$, and $\boldsymbol{\mu}_b$:

$$\mathbf{f}(\boldsymbol{\rho}, \boldsymbol{\mu}_a, \boldsymbol{\mu}_b) = \frac{3\mu_0}{4\pi\rho^4}\left((\hat{\boldsymbol{\rho}} \times \boldsymbol{\mu}_a) \times \boldsymbol{\mu}_b + (\hat{\boldsymbol{\rho}} \times \boldsymbol{\mu}_b) \times \boldsymbol{\mu}_a - 2\hat{\boldsymbol{\rho}}(\boldsymbol{\mu}_a \cdot \boldsymbol{\mu}_b) + 5\hat{\boldsymbol{\rho}}(\hat{\boldsymbol{\rho}} \times \boldsymbol{\mu}_a) \cdot (\hat{\boldsymbol{\rho}} \times \boldsymbol{\mu}_b)\right) \tag{4.2a}$$

$$\boldsymbol{\tau}(\boldsymbol{\rho}, \boldsymbol{\mu}_a, \boldsymbol{\mu}_b) = \frac{\mu_0}{4\pi\rho^3}\left(3(\hat{\boldsymbol{\rho}} \cdot \boldsymbol{\mu}_a)(\boldsymbol{\mu}_b \times \hat{\boldsymbol{\rho}}) + (\boldsymbol{\mu}_a \times \boldsymbol{\mu}_b)\right) \tag{4.2b}$$

4.4 Application to Space Structures

Brown and Eremenko discuss the utility of a fractionated space system to generic mission operation concepts.[43] Flux pinning potentially provides a force to bind together vehicles with a spatial distribution, allowing the system

to inherit some of the benefits of a fractionated architecture. The aim of implementing a flux-pinned connection between individual vehicles is to offer some degree of passive stability to the relative motion of the formation components. By pairing a HTSC on one vehicle with a magnetic field source on a second, we establish flux-pinning connections that tie the dynamics of a fractionated space system together. One critical design parameter for any flux-pinned non-contacting structure is the separation distance between the HTSC on one vehicle and the magnetic field source on its neighbor. Shoer demonstrated a strong dependance of the effective stiffness of the connection upon this distance,[27,28] which in turn relates to the passive disturbance rejection capabilities of the system as a whole. While magnetic flux pinning with permanent magnets potentially provides sufficient passively stable dynamics for relative position and orientation states for a spacecraft formation, additional incorporation of an active feedback control law would further expand the reconfiguration and disturbance rejection capabilities of the formation. The literature describes several feedback control schemes specific to a particular non-contacting force that could be adapted for use with spacecraft dynamically linked by magnetic flux pinning.[12,44]

Applying this simplified stiffness and damping model to a close-proximity formation of vehicles allows for preliminary investigations of the utility of flux pinning for space applications as a passive stationkeeping effect. The example formation chosen is that of a non-contacting ring structure. This particular formation geometry is of interest in the development of sparse-aperture space telescopes and affords a few key advantages such as redundant UV-plane coverage.[47]

The following simulations make a number of assumptions regarding the dynamics of the formation. All vehicles are assumed identical with a single HTSC and a single magnetic dipole which interact via flux pinning with the two closest neighboring vehicles. The simulation treats the formation as free-floating, corresponding to a scenario where the formation is far from any significant gravitational field source. The resulting equations of motion for the i^{th} vehicle are then

$$\mathbf{I}_i \cdot \dot{\boldsymbol{\omega}}_i = -\boldsymbol{\omega}_i \times \mathbf{I}_i \cdot \boldsymbol{\omega}_i + (\boldsymbol{\tau}_{m/i+1} + \mathbf{b}_m \times \mathbf{f}_{m/i+1}) + (\boldsymbol{\tau}_{h/i-1} + \mathbf{b}_h \times \mathbf{f}_{h/i-1}) + \mathbf{w}_{\tau i} \tag{4.3}$$

$$m_i \ddot{\mathbf{r}}_i = \mathbf{f}_{m/i+1} + \mathbf{f}_{h/i-1} + \mathbf{w}_{fi} \tag{4.4}$$

The first scenario consists of the candidate ring formation in the presence of input force and torque disturbances with no forces acting between the satellites. The second introduces a flux-pinned connection between neighboring vehicles. The input disturbance in both cases is modeled with a zero-mean Gaussian distribution with a standard deviation of 1-μN for the force disturbance and 1 μN-m for the torque disturbance as a nominal environmental effects of the same order of magnitude as some non-conservative perturbations, such as solar radiation pressure.[48] Table 4.1 lists the inertia properties and physical dimensions of each of the identical vehicles. In this scenario, 10 vehicles on a planar 3.6 m diameter ring, resulting in 16.14 cm separations between HTSC and magnetic dipoles on neighboring vehicles. Linearizing the dynamics of the system about the nominal ring formation predicts the damped natural frequencies of the structural modes associated with flux pinning to range between 0.00423 Hz and 0.140 Hz. As the stiffness of the flux-pinned connection between vehicles depends upon the separation distance between the magnet and the HTSC,[27] the natural frequencies of these modes can be

Table 4.1: Ring vehicle parameters

Parameter	Value
Total mass (kg)	100
Bounding box dimensions (m^3)	$1.0 \times 1.0 \times 0.2$
Principle moments of inertia (kg-m^2)	[5.8 5.8 10.0]
Magnet location in body coordinates (m)	[-0.5 0.0 0.0]
HTSC location in body coordinates (m)	[0.5 0.0 0.0]
$\hat{\mathbf{n}}_{HTSC}$ in body coordinates	[1.0 0.0 0.0]
$\boldsymbol{\mu}_i, \boldsymbol{\mu}_C$ in body coordinates (J/T)	[100.0 0.0 0.0]
C_t (N-s/m)	0.01
C_r (N-m-s/rad)	0.01

shifted by defining a different ring diameter, and thus vehicle separation, as the equilibrium.

We aim to study the natural behavior of the system due to disturbance inputs in the absence of control. As the sum of the forces and torques due to noise tend to translate the system center of mass and overall orientation, performance parameters of the uncontrolled structure should depend only upon the relative motion of the vehicles. One such set of parameters would be the location of the vehicles relative to the formation center of mass in coordinates minimizing the out-of-plane position of the vehicles as shown in Fig. 4.2. This plane passing through the formation center of mass has a normal vector $\hat{\mathbf{n}}$ that minimizes following cost function:

$$J = \sum_{i=1}^{n} \frac{1}{2} (\hat{\mathbf{n}} \cdot \mathbf{d}_i)^2 = \frac{1}{2} \hat{\mathbf{n}}^T \left[\sum_{i=1}^{n} \mathbf{d}_i \mathbf{d}_i^T \right] \hat{\mathbf{n}}, \text{ where } \hat{\mathbf{n}}^T \hat{\mathbf{n}} = 1 \tag{4.5}$$

The coordinates Z_i, R_i, and θ_i depicted in Fig. 4.2 describe the position of the i^{th} spacecraft in cylindrical coordinates with respect to the center of the formation located by $\mathbf{r}_{cm}$. These measurements correspond to the out-of-plane

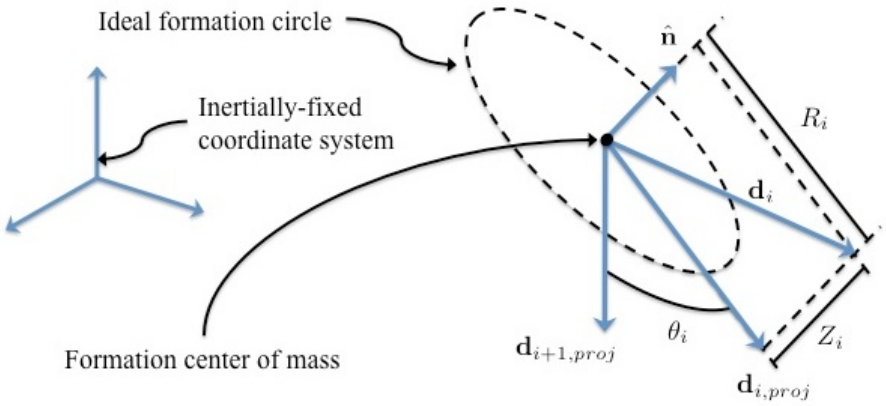

Figure 4.2: Parameters used to determine the relative position of a vehicle to its ideal location on a ring in a plane.

displacement Z_i, the in-plane radial distance to the center of mass R_i, and the in-plane angular separation θ_i between vehicles i and $i+1$.

$$Z_i = \mathbf{d}_i^T \hat{\mathbf{n}} \tag{4.6}$$

$$R_i = \sqrt{\mathbf{d}_i^T \mathbf{d}_i - Z_i^2} \tag{4.7}$$

$$\theta_i = \cos^{-1}\left(\frac{\mathbf{d}_i^T \mathbf{d}_{i+1} - Z_i Z_{i+1}}{R_i R_{i+1}}\right) \tag{4.8}$$

We performed 30 simulations of the ring formation for both the flux-pinned and dynamically-unlinked scenarios corresponding to unique disturbance input time histories. The means and standard deviations of these metrics over all 30 pairs of simulations are given in Fig. 4.3.

4.5 Conclusion

Simulations of a 3.6-m ring formation of 10 vehicles with flux pinning acting between neighboring vehicles confirm that a flux-pinning interface

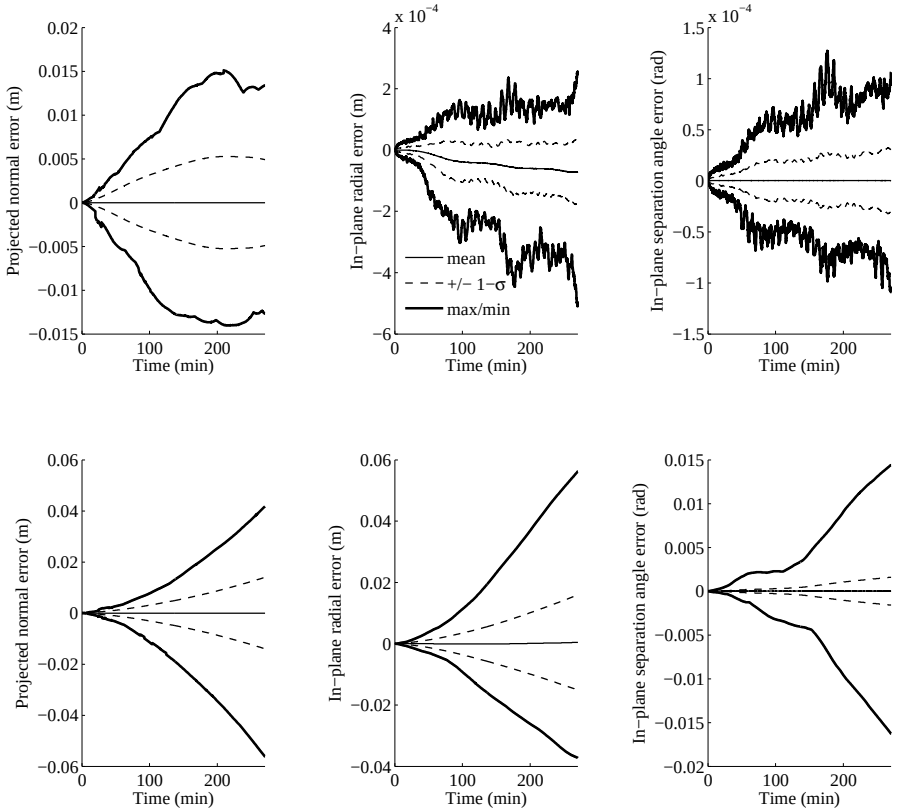

Figure 4.3: Plots of the mean, $\pm 1 - \sigma$ bounds, and min/max values of vehicle position error of the 30 sets of both flux-pinned and dynamically unlinked formations as a result of disturbance forces and torques. The top row of plots correspond to the simulations with flux-pinning interfaces between neighboring vehicles. The bottom row of plots correspond to the unlinked simulations.

can maintain a loose ring shape in the presence of input force and torque disturbances applied to the vehicles individually. The slight decrease in mean ring radius for the flux-pinned formation simulations is attributed to the projection of the relative position vector of the vehicles into a single plane. As expected, the non-interacting simulations resulted in a rapidly increasing

radial position error and wider distribution of the vehicles in the out-of-plane direction. The resulting spatial formation of the vehicles for the non-interacting simulations had no resemblance to the original formation, especially in comparison to the loose ring maintained by the flux-pinned simulations. While the flux pinning force and torque interaction between vehicles passively kept the formation together in a bulk sense, active control would be necessary for any task with strict relative-position requirements.

CHAPTER 5

INTEGRALS OF MOTION FOR PLANAR MULTI-BODY FORMATIONS WITH INTERNAL FORCES

Interest in the use of non-contacting forces between spacecraft has prompted many studies of the dynamics of such formations. While the introduction of such a force potentially complicates the analysis of these systems, integrals of motion still exist for idealized cases. These integrals not only define relationships between the states at two different times, but also provide a means to describe the error introduced through application of simplifying assumptions to the formation dynamics. This paper develops expressions of two integrals of motion for a planar, two-vehicle formation, and examines their evolution under several assumptions pertaining to the motion of the formation center of mass.

5.1 Nomenclature

A, B	Constraint matricies
a_1, a_2	Semimajor axes of spacecraft
C_E	Total mechanical energy
C_H	Total angular momentum magnitude
e_1, e_2	Eccentricities of spacecraft
$\mathbf{e}_x$, $\mathbf{e}_y$, $\mathbf{e}_c$, $\mathbf{e}_\rho$, $\mathbf{e}_\gamma$, $\mathbf{e}_\theta$	Basis vectors
$\mathbf{h}_1$, $\mathbf{h}_2$	Angular momentum vectors of individual spacecraft
$\mathcal{L}$	Lagrangian of dynamics system
m_1, m_2, M	Masses of individual spacecraft, sum of masses

The content of this chapter has been accepted for publication by the *Journal of Guidance, Control, and Dynamics* and is awaiting publication under the title "Integrals of Motion for Planar Multibody Formations with Internal Forces" (Ref. 49).

q	Generalized coordinates
$\tilde{q}$	Constrained generalized coordinates
$\mathbf{r}_1, \mathbf{r}_2, \mathbf{r}_c, \boldsymbol{\rho}$	Position vectors
r_1, r_2, r_c, ρ	Magnitudes of position vectors
$\mathcal{R}$	Interaction potential energy
$\mathcal{T}, \mathcal{V}$	Total kinetic, potential energies
x	System state of original system
$\bar{x}$	System state of simplified system
γ, θ	Angles describing orientation of formation
λ_1, λ_2	Lagrange multipliers
μ	Gravitational parameter

5.2 Introduction

Studying the relative motion of multiple spacecraft in orbit about a common central body has proven useful for such tasks as rendezvous and docking, in-orbit inspection, and mission-enabling formation flight. An examination of the effects of independent control inputs acting on individual spacecraft informs mission planning and controller design by predicting the evolving Keplerian orbits of the vehicles through a maneuver. This classic approach of utilizing external forces as control inputs allows for the arbitrary reconfiguration of the multi-body system. Augmenting the dynamics of a spacecraft formation with an action-at-a-distance force internal to the multi-body system presents a unique opportunity by enabling control of the relative motion of the spacecraft while maintaining certain integrals of motion. This paper examines the dynamics of a planar, two-vehicle formation in orbit about a common central

body with such an internal force acting between the spacecraft. Through this study, integrals of motion are identified and used to describe relationships bounding the system state trajectory and to evaluate a common assumption regarding the motion of the formation center of mass.

While the unperturbed motion of a spacecraft in a Keplerian orbit about a central body is well-known, analytical expressions of its state trajectory do not exist in the presence of arbitrary perturbations. At least two related approaches begin to address this problem. The first approach identifies conserved quantities relating the states, such as with the Jacobi Integral placing bounds on the trajectory of a point mass in the Circular Restricted Three-Body Problem.[50] The second approach linearizes the system's dynamics about an assumed center of mass trajectory, resulting in a set of first-order ordinary differential equations.[6] These simplifying assumptions can be framed as artificially enforcing system state behavior in contrast with the natural known behavior of the unmodified dynamic system. Both of these approaches reduce the total number of states required to represent the dynamics of the system, simplifying controller design and potentially bounding the state trajectory. We address both of the above approaches through the development of a Lagrangian dynamics model. Through this method, integrals of the motion representing conserved quantities can quickly be identified and applied to the example system. In addition to reducing the number of states of the system, these conserved quantities of the original system also provide a means to evaluate the applicability of simplifying assumptions. Applying such an assumption regarding the motion of the system is equivalent to enforcing a constraint on its dynamics, and the resulting hypothetical constraint force potentially modifies the otherwise conserved integrals of motion of the original

system. Several groups have investigated the specific topic of energy- and momentum-conserving integration schemes.[51–54] While these methods could be employed in the analysis of the two-vehicle system under discussion, this paper focuses on the interpretation of the relationship between the error introduced in the generalized coordinates and the conserved quantities under a common simplifying assumption regarding the center of mass motion of the formation.

The paper begins by developing the initial mathematical model of the planar, two-vehicle system dynamics and identifies relevant integrals of motion in section 5.3. Subsequently, section 5.4 examines how these integrals of motion translate into equations relating the osculating orbital elements of the individual vehicles. Section 5.5 then examines some possible assumptions regarding the evolution of the system's state. The impact of a center-of-mass-motion constraint is then examined in terms the effect upon the integrals of motion derived from the original system. The paper then supports the theoretical development through a simulated example formation in section 5.6.

5.3 Dynamics Model Description

Consider the following planar system describing two masses, m_1 and m_2, relative to a large central body. Their locations are described by $\mathbf{r}_1$ and $\mathbf{r}_2$, respectively, and their center of mass is defined by the vector $\mathbf{r}_c$. The vector $\boldsymbol{\rho}$ points from m_1 to m_2. Mathematically, we can describe these vectors in terms of each other.

$$\begin{aligned} \mathbf{r}_c &= \frac{1}{M}\left(m_1\mathbf{r}_1 + m_2\mathbf{r}_2\right) = r_c\mathbf{e}_c & \boldsymbol{\rho} &= \mathbf{r}_2 - \mathbf{r}_1 = \rho\mathbf{e}_\rho \\ \mathbf{r}_1 &= \mathbf{r}_c - \frac{m_2}{M}\boldsymbol{\rho} & \mathbf{r}_2 &= \mathbf{r}_c + \frac{m_1}{M}\boldsymbol{\rho} \end{aligned} \tag{5.1}$$

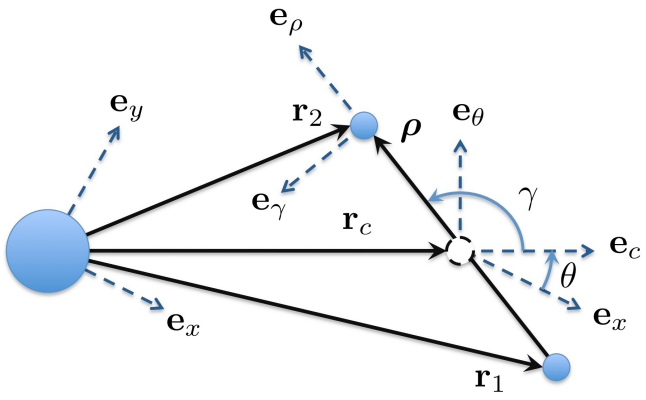

Figure 5.1: Layout of m_1 and m_2 relative to a central body.

From these equations, we can define the inertial time derivatives of $\mathbf{r}_1$ and $\mathbf{r}_2$ in terms of inertial time derivatives of $\mathbf{r}_c$ and $\boldsymbol{\rho}$.

$$\dot{\mathbf{r}}_1 = \dot{\mathbf{r}}_c - \frac{m_2}{M}\dot{\boldsymbol{\rho}} \qquad\qquad \dot{\mathbf{r}}_2 = \dot{\mathbf{r}}_c + \frac{m_1}{M}\dot{\boldsymbol{\rho}} \tag{5.2}$$

Both masses are gravitationally attracted to the central body and experience a conservative force directed along the vector $\mathbf{e}_\rho$ pointing between the two masses. This force is derived from the potential function $\mathcal{R}$ and is assumed to only depend upon the relative separation distance ρ.

5.3.1 Deriving Equations of Motion

The Lagrangian $\mathcal{L}$ is formed from the kinetic and potential energy expressions, $\mathcal{T}$ and $\mathcal{V}$.

$$\mathcal{T} = \frac{1}{2}m_1\dot{\mathbf{r}}_1 \cdot \dot{\mathbf{r}}_1 + \frac{1}{2}m_2\dot{\mathbf{r}}_2 \cdot \dot{\mathbf{r}}_2 \tag{5.3}$$

$$\mathcal{V} = -\mu\left(\frac{m_1}{r_1} + \frac{m_2}{r_2}\right) + \mathcal{R} \tag{5.4}$$

$$\mathcal{L} = \mathcal{T} - \mathcal{V} = \frac{1}{2}m_1\dot{\mathbf{r}}_1 \cdot \dot{\mathbf{r}}_1 + \frac{1}{2}m_2\dot{\mathbf{r}}_2 \cdot \dot{\mathbf{r}}_2 + \mu\left(\frac{m_1}{r_1} + \frac{m_2}{r_2}\right) - \mathcal{R} \tag{5.5}$$

The position vectors of Eq. (5.1) can be expressed in terms of scalar components multiplying basis vectors described in Fig. 5.1.

$$\begin{aligned}\mathbf{r}_1 &= \left(r_c - \frac{m_2}{M}\rho\cos\gamma\right)\mathbf{e}_c - \frac{m_2}{M}\rho\sin\gamma\mathbf{e}_\theta \\ \mathbf{r}_2 &= \left(r_c + \frac{m_1}{M}\rho\cos\gamma\right)\mathbf{e}_c + \frac{m_1}{M}\rho\sin\gamma\mathbf{e}_\theta\end{aligned} \tag{5.6}$$

Similarly, we can write the inertial velocity vectors in terms of orthogonal basis vectors $\mathbf{e}_c$ and $\mathbf{e}_\theta$.

$$\begin{aligned}\dot{\mathbf{r}}_1 = &\left(\dot{r}_c - \frac{m_2}{M}\left(\dot{\rho}\cos\gamma - \rho\left(\dot{\theta}+\dot{\gamma}\right)\sin\gamma\right)\right)\mathbf{e}_c \\ &+ \left(r_c\dot{\theta} - \frac{m_2}{M}\left(\dot{\rho}\cos\gamma + \rho\left(\dot{\theta}+\dot{\gamma}\right)\sin\gamma\right)\right)\mathbf{e}_\theta\end{aligned} \tag{5.7}$$

$$\begin{aligned}\dot{\mathbf{r}}_2 = &\left(\dot{r}_c + \frac{m_1}{M}\left(\dot{\rho}\cos\gamma - \rho\left(\dot{\theta}+\dot{\gamma}\right)\sin\gamma\right)\right)\mathbf{e}_c \\ &+ \left(r_c\dot{\theta} + \frac{m_1}{M}\left(\dot{\rho}\cos\gamma + \rho\left(\dot{\theta}+\dot{\gamma}\right)\sin\gamma\right)\right)\mathbf{e}_\theta\end{aligned} \tag{5.8}$$

Consider the following choice of generalized coordinates:

$$q = \begin{bmatrix} \rho & \gamma & r_c & \theta \end{bmatrix}^T \tag{5.9}$$

We can define the lengths of the vectors $\mathbf{r}_1$ and $\mathbf{r}_2$ in terms of q.

$$\begin{aligned}r_1 = r_1(q) &= (\mathbf{r}_1\cdot\mathbf{r}_1)^{1/2} = \left(q_3^2 - 2\frac{m_2}{M}q_1q_3\cos q_2 + \left(\frac{m_2}{M}q_1\right)^2\right)^{1/2} \\ r_2 = r_2(q) &= (\mathbf{r}_2\cdot\mathbf{r}_2)^{1/2} = \left(q_3^2 + 2\frac{m_1}{M}q_1q_3\cos q_2 + \left(\frac{m_1}{M}q_1\right)^2\right)^{1/2}\end{aligned} \tag{5.10}$$

The expressions for the energy terms and Lagrangian from Eqs. (5.3), (5.4), and (5.5) are then rewritten in terms of the generalized coordinates.

$$\mathcal{T}(q,\dot{q}) = \frac{1}{2}\left(M\left(\dot{q}_3^2 + q_3^2\dot{q}_4^2\right) + \frac{m_1m_2}{M}\left(\dot{q}_1^2 + q_1^2(\dot{q}_2+\dot{q}_4)^2\right)\right) \tag{5.11}$$

$$\mathcal{V}(q) = -\mu\left(\frac{m_1}{r_1} + \frac{m_2}{r_2}\right) + \mathcal{R}(q) \tag{5.12}$$

$$\mathcal{L}(q,\dot{q}) = \frac{1}{2}\left(M\left(\dot{q}_3^2 + q_3^2\dot{q}_4^2\right) + \frac{m_1m_2}{M}\left(\dot{q}_1^2 + q_1^2(\dot{q}_2+\dot{q}_4)^2\right)\right) \tag{5.13}$$

$$+\mu\left(\frac{m_1}{r_1}+\frac{m_2}{r_2}\right)-\mathcal{R}(q)$$

The equation of motion describing the dynamics of the generalized coordinate q_j for a system acted upon only by conservative forces is given by the Lagrange's equation:

$$\frac{d}{dt}\frac{\partial}{\partial\dot{q}_j}\mathcal{L}-\frac{\partial}{\partial q_j}\mathcal{L}=0 \tag{5.14}$$

Applying Eq. (5.14) to Eq. (5.13) provides the set of second-order differential equations describing the dynamics of the system.

$$\ddot{q}_1-q_1\left(\dot{q}_2+\dot{q}_4\right)^2+\frac{\mu}{r_1^3}\left(\frac{m_2}{M}q_1-q_3\cos q_2\right)+\frac{\mu}{r_2^3}\left(\frac{m_1}{M}q_1+q_3\cos q_2\right)$$
$$+\frac{M}{m_1m_2}\frac{\partial}{\partial q_1}\mathcal{R}=0 \tag{5.15}$$

$$q_1^2\left(\ddot{q}_2+\ddot{q}_4\right)+2q_1\dot{q}_1\left(\dot{q}_2+\dot{q}_4\right)+\mu\left(\frac{1}{r_1^3}-\frac{1}{r_2^3}\right)q_1q_3\sin q_2=0 \tag{5.16}$$

$$\ddot{q}_3-q_3\dot{q}_4^2+\mu\frac{m_1m_2}{M}\left(\frac{1}{r_1^3}\left(\frac{M}{m_2}q_3-q_1\cos q_2\right)+\frac{1}{r_2^3}\left(\frac{M}{m_1}q_3+q_1\cos q_2\right)\right)=0 \tag{5.17}$$

$$q_1^2\left(\ddot{q}_2+\ddot{q}_4\right)+2q_1\dot{q}_1\left(\dot{q}_2+\dot{q}_4\right)+\frac{M^2}{m_1m_2}\left(q_3\ddot{q}_4+2q_3\dot{q}_3\dot{q}_4\right)=0 \tag{5.18}$$

5.3.2 Integrals of Motion

Deriving Eqs. (5.15), (5.16), (5.17), and (5.18) by a Lagrangian approach allows for quick identification of two integrals of motion. One of these integrals corresponds to the conservation of mechanical energy. Because the potential energy, $\mathcal{V}$, only depends upon the positions of m_1 and m_2, its time derivative can be written in terms of inertial velocities multiplying partials of $\mathcal{V}$ with respect to the position vectors.

$$\frac{d}{dt}\mathcal{V}=\dot{\mathbf{r}}_1\cdot\frac{\partial\mathcal{V}}{\partial\mathbf{r}_1}+\dot{\mathbf{r}}_2\cdot\frac{\partial\mathcal{V}}{\partial\mathbf{r}_2} \tag{5.19}$$

The forces resulting from the potential function are also related to these partial derivatives of $\mathcal{V}$.

$$m_1\ddot{\mathbf{r}}_1 = -\frac{\partial \mathcal{V}}{\partial \mathbf{r}_1} \qquad\qquad m_2\ddot{\mathbf{r}}_2 = -\frac{\partial \mathcal{V}}{\partial \mathbf{r}_2} \tag{5.20}$$

Incorporating these results into the expression of $\dot{\mathcal{T}}$ reveals a relation between the derivatives of the kinetic and potential energy.

$$\begin{aligned}\frac{d}{dt}\mathcal{T} =& m_1\dot{\mathbf{r}}_1 \cdot \ddot{\mathbf{r}}_1 + m_2\dot{\mathbf{r}}_2 \cdot \ddot{\mathbf{r}}_2 \\ =& -\frac{d\mathbf{r}_1}{dt} \cdot \frac{\partial \mathcal{V}}{\partial \mathbf{r}_1} - \frac{d\mathbf{r}_2}{dt} \cdot \frac{\partial \mathcal{V}}{\partial \mathbf{r}_2} \\ =& -\frac{d\mathcal{V}}{dt}\end{aligned} \tag{5.21}$$

Summing the expressions for the time derivative of the kinetic and potential energies shows that the total energy, C_E, is conserved.

$$\frac{d}{dt}\left(\mathcal{T} + \mathcal{V}\right) = \frac{d}{dt}C_E = 0 \tag{5.22}$$

Equation (5.22) defines C_E as a constant that can be related at different times in the state trajectory time history.

$$C_E = \frac{1}{2}\left(M\left(\dot{q}_3^2 + q_3^2\dot{q}_4^2\right) + \frac{m_1 m_2}{M}\left(\dot{q}_1^2 + q_1^2\left(\dot{q}_2 + \dot{q}_4\right)^2\right)\right) - \mu\left(\frac{m_1}{r_1} + \frac{m_2}{r_2}\right) + \mathcal{R}\left(q\right) \tag{5.23}$$

The lack of q_4 in Eq. (5.13) suggests another integral of motion. Writing Eq. (5.14) for q_4 reveals this second time-independent quantity.

$$\frac{d}{dt}\frac{\partial}{\partial \dot{q}_4}\mathcal{L} - \frac{\partial}{\partial q_4}\mathcal{L} = \frac{d}{dt}\frac{\partial}{\partial \dot{q}_4}\mathcal{L} = 0 \tag{5.24}$$

This equation corresponds to the conservation of total angular momentum of the system.

$$C_H = \frac{\partial}{\partial \dot{q}_4}\mathcal{L} = Mq_3^2\dot{q}_4 + \frac{m_1 m_2}{M}q_1^2\left(\dot{q}_2 + \dot{q}_4\right) \tag{5.25}$$

While neither Eq. (5.23) nor Eq. (5.25) should come as a surprise, the process of defining these quantities in terms of the generalized coordinates will prove useful in the examination of the nonlinear system described by Eqs. (5.15), (5.16), (5.17), and (5.18).

5.4 Bounding System Output

By defining time-independent relationships between the generalized coordinates, C_E and C_H potentially provide a means to glean information about the system at a later time without the need to numerically or analytically integrate the equations of motion. Consider, for example, the evolution of the semimajor axes of m_1 and m_2 through the application of the forces associated with $\mathcal{R}$. Assuming a mission designer has control over the input of this conservative force acting on the two masses, an orbit-change maneuver affecting both vehicles would result from applying the force for only a limited duration. The semimajor axes of m_1 and m_2 are defined by the mechanical energy associated with the inertial velocity and gravitational potential of masses individually in the corresponding two-body problem.[55]

$$m_i\left(\frac{\dot{\mathbf{r}}_i\cdot\dot{\mathbf{r}}_i}{2}-\frac{\mu}{r_i}\right)=-\frac{\mu m_i}{2a_i} \tag{5.26}$$

The total mechanical energy of the system can then be rearranged to include terms associated with the osculating semimajor axis a_i.

$$\begin{aligned} C_E =& m_1\left(\frac{\dot{\mathbf{r}}_1\cdot\dot{\mathbf{r}}_1}{2}-\frac{\mu}{r_1}\right)+m_2\left(\frac{\dot{\mathbf{r}}_2\cdot\dot{\mathbf{r}}_2}{2}-\frac{\mu}{r_2}\right)+\mathcal{R} \\ =& -\frac{\mu}{2}\left(\frac{m_1}{a_1}+\frac{m_2}{a_2}\right)+\mathcal{R} \end{aligned} \tag{5.27}$$

As C_E does not vary with time, this equation can be used to relate changes in the interaction potential, $\mathcal{R}$, to changes in the semimajor axes of m_1 and m_2.

$$-\frac{\mu}{2}\left(\frac{m_1}{a_{1,0}}+\frac{m_2}{a_{2,0}}\right)+\mathcal{R}_0=-\frac{\mu}{2}\left(\frac{m_1}{a_{1,f}}+\frac{m_2}{a_{2,f}}\right)+\mathcal{R}_f \tag{5.28}$$

Another way to interpret Eq. (5.27) is to recognize that the the combination of a_1, a_2, and R need to exist on a surface specified by the constants C_E, μ, m_1, and m_2. Figure 5.2 provides an example surface generated by the simulation parameters from Table 5.1.

A similar derivation relates the total angular momentum of the system to the semimajor axes and orbital eccentricities of m_1 and m_2 under the assumptions of two-body motion. The eccentricity of each mass is defined by an equation depending upon its individual angular momentum and semimajor axis.[55]

$$e_i=\sqrt{1-\frac{\mathbf{h}_i\cdot\mathbf{h}_i}{\mu m_i^2 a_i}} \tag{5.29}$$

The total angular momentum of the system is also defined by summing up the contributions from the individual vehicles. This allows for the expression of the constant angular momentum magnitude, C_H, in terms of semimajor axis and eccentricity parameters.

$$C_H=\sqrt{\mu a_1 m_1^2\left(1-e_1^2\right)}+\sqrt{\mu a_2 m_2^2\left(1-e_2^2\right)} \tag{5.30}$$

Similar to the relation between Eq. (5.27) and Fig. 5.2, Eq. (5.30) describes a hyperdimensional surface parameterized by a_1, a_2, e_1, and e_2 for a given set of constants C_H, μ, m_1, and m_2.

The conservation of energy and angular momentum can be expressed in either generalized coordinates, as in Eqs. (5.23) and (5.25), or in terms of a set of outputs, such as the selection of osculating orbital elements in Eqs. (5.27) and

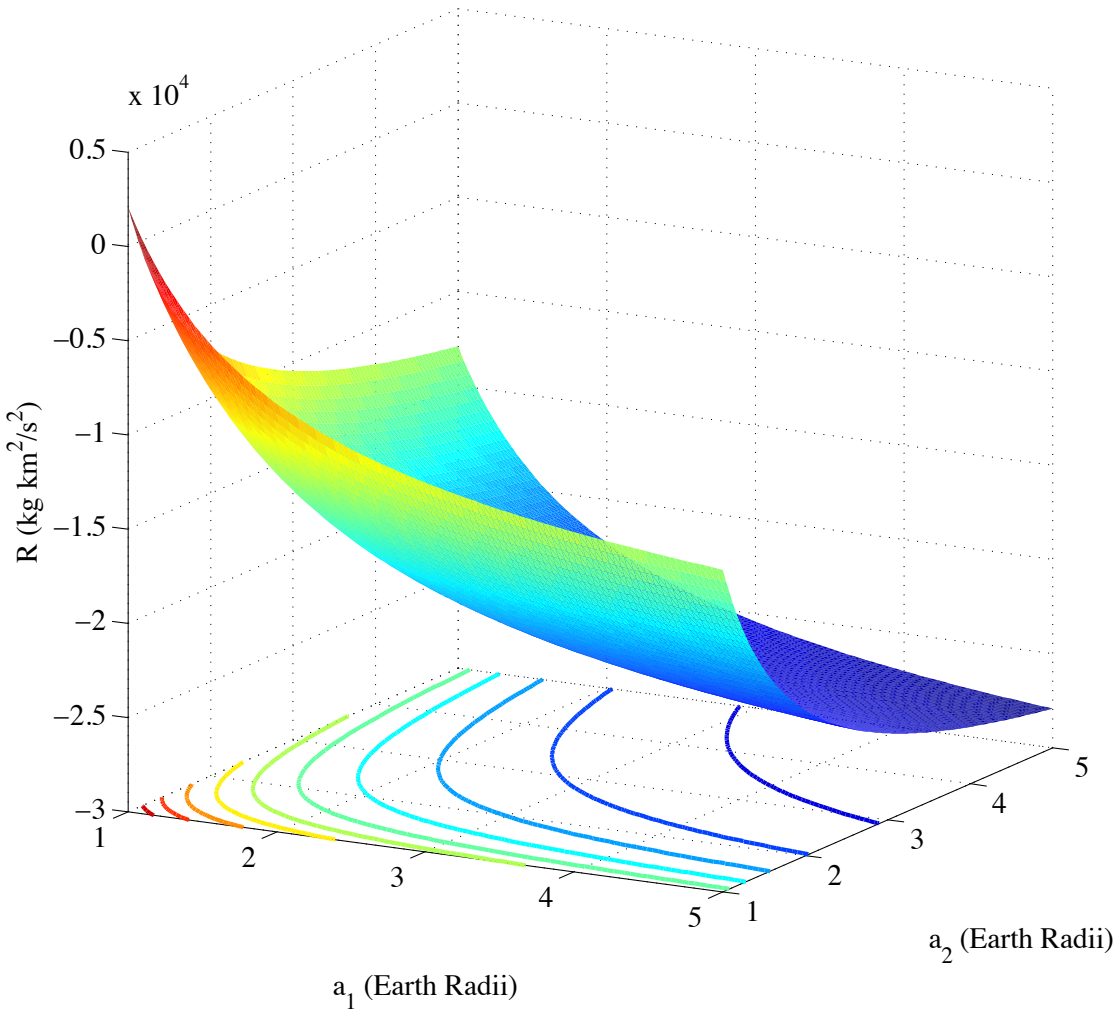

Figure 5.2: Surface and contour plot of interaction potential R in relation to semimajor axes a_1 and a_2 using the parameters from Table 5.1.

(5.30). In either case, these equations provide a means to analytically bound the motion of the system, as any combination of states or outputs violating these conservation laws for a given set of initial conditions cannot be reached.

5.5 Implications for Simplifying Assumptions

Integrals of motion also may be utilized when attempting to simplify the mathematical expression of the dynamics of a system. By defining conserved quantities, such as C_H for Eqs. (5.15), (5.16), (5.17), and (5.18), the time derivative of a particular state can be defined in terms of the remaining states and their time derivatives and can be substituted into the equations of motion, which effectively reduces the number of differential equations to be solved. Mathematically, a similar process occurs when applying constraints to the system dynamics. Defining specified states through constraint equations removes the need to solve for those states by other means. Specifying such constraints, however, generally does not preserve the conservation laws defining the integrals of motion derived for the unconstrained system.

A common set of simplifying assumptions for the relative motion of two spacecraft in orbit restricts the motion of the formation center of mass to follow a defined path, usually a Keplerian orbit.[12,13] This approach is similar to utilizing the Clohessy-Wiltshire equations for relative motion in near-circular orbits.[6] As a result, the relative motion of the two vehicles can be examined independently from the dynamics of the center of mass. The quality and applicability of such constraints could be evaluated by examining the evolution of the integrals of motion of the unconstrained system. Kim and Schaub formulate this problem in terms of orbital element differences and investigate angular momentum conservation for a variety of reference trajectories, including the center-of-mass motion and the mass-averaged orbital elements.[21] As these quantities are not necessarily conserved in the constrained system, their variation is linked to the error between the constrained and unconstrained states.

The equations of motion of a constrained system are derived utilizing Lagrange multipliers.[14] When m constraints applied to a system with n generalized coordinates are linear in the constrained state derivatives, the constraint equations take the following form:

$$\sum_{j=1}^{n} A_{kj}\dot{q}_j + B_k = 0 \qquad\qquad k = 1, 2, ..., m \tag{5.31}$$

The equations of motion of the state q_j of this constrained system then follow the constrained form of Lagrange's equation.

$$\frac{d}{dt}\frac{\partial}{\partial \dot{q}_j}\mathcal{L} - \frac{\partial}{\partial q_j}\mathcal{L} = \sum_{k=1}^{m} \lambda_k A_{kj} \tag{5.32}$$

The λ_k values correspond to the constraint forces and torques applied to the system dynamics.[14]

5.5.1 Constrained Equations of Motion

Consider the same two-vehicle formation in orbit about a common central body as depicted in Fig. 5.1, but with the addition of two constraint equations defining the time history of the center-of-mass motion described by q_3 and q_4.

$$q_3 = \tilde{q}_3 \qquad\qquad q_4 = \tilde{q}_4 \tag{5.33}$$

As the $\tilde{q}_3$ and $\tilde{q}_4$ are assumed to be known functions of time, the time derivatives of q_3 and q_4 are also defined. Reformatting these two constraints results in a set of linear equations conforming to the format of Eq. (5.31).

$$A\dot{q} + B = \begin{bmatrix} 0 & 0 & 1 & 0 \\ 0 & 0 & 0 & 1 \end{bmatrix} \dot{q} - \begin{bmatrix} \dot{\tilde{q}}_3 \\ \dot{\tilde{q}}_4 \end{bmatrix} = 0 \tag{5.34}$$

As the matrix A involves only the states q_3 and q_4, Eqs. (5.15), (5.16), and (5.34) define the dynamics of the constrained system. The λ_k values are defined

through Eq. (5.32).

$$\lambda_1 = \ddot{\tilde{q}}_3 - \tilde{q}_3\dot{\tilde{q}}_4^2 + \mu\frac{m_1 m_2}{M}\left(\frac{1}{\tilde{r}_1^3}\left(\frac{M}{m_2}\tilde{q}_3 - q_1\cos q_2\right) + \frac{1}{\tilde{r}_2^3}\left(\frac{M}{m_1}\tilde{q}_3 + q_1\cos q_2\right)\right) \tag{5.35}$$

$$\lambda_2 = q_1^2\left(\ddot{q}_2 + \ddot{\tilde{q}}_4\right) + 2q_1\dot{q}_1\left(\dot{q}_2 + \dot{\tilde{q}}_4\right) + \frac{M^2}{m_1 m_2}\left(\tilde{q}_3\ddot{\tilde{q}}_4 + 2\tilde{q}_3\dot{\tilde{q}}_3\dot{\tilde{q}}_4\right) \tag{5.36}$$

In the case where the system naturally followed the constraints imposed by Eq. (5.34), λ_1 and λ_2 would be zero for all time. An examination of Eq. (5.36) with the definition of C_H given by Eq. (5.25) defines the time-dependence of the C_H integral of motion of the unconstrained system.

$$\frac{d}{dt}\frac{\partial}{\partial\dot{q}_4}\mathcal{L} - \frac{\partial}{\partial q_4}\mathcal{L} = \frac{d}{dt}C_H = \lambda_2 \tag{5.37}$$

Equation (5.37) demonstrates that for the constrained system and a general choice of $\tilde{q}_3$ and $\tilde{q}_4$ trajectories resulting in a non-zero λ_2, angular momentum is not conserved.

5.5.2 Constrained Equations of Motion Conserving C_H

A possible further constraint to be applied to the original unconstrained system would enforce the conservation of angular momentum. Requiring λ_2 to be zero effectively enforces this constraint. Substituting Eq. (5.34) into Eq. (5.25) and rearranging provides an expression of $\dot{q}_2$ in terms of only q_1 and known quantities. This differential equation and the constrained version of Eq. (5.15) define the state dynamics of the constrained system conserving angular momentum.

$$\ddot{q}_1 - q_1\left(\dot{q}_2 + \dot{\tilde{q}}_4\right)^2 + \frac{\mu}{\tilde{r}_1^3}\left(\frac{m_2}{M}q_1 - \tilde{q}_3\cos q_2\right) + \frac{\mu}{\tilde{r}_2^3}\left(\frac{m_1}{M}q_1 + \tilde{q}_3\cos q_2\right) + \frac{M}{m_1 m_2}\frac{\partial}{\partial q_1}\mathcal{R} = 0 \tag{5.38}$$

$$\dot{q}_2 = \frac{M}{q_1^2 m_1 m_2}\left(C_H - M\tilde{q}_3^2\dot{\tilde{q}}_4\right) - \dot{\tilde{q}}_4 \tag{5.39}$$

While λ_2 is necessarily zero in this formulation, λ_1 is still allowed to be a non-zero value and can still function as a measure of the applicability of the constraining assumptions.

5.5.3 Integrals of Motion and Assumption Quality

Conservation laws, such as those defining C_E and C_H in Eqs. (5.23) and (5.25), are potentially useful for bounding the state or output error of a system under a set of simplifying assumptions. As demonstrated in the derivation of Eq. (5.37), these integrals of motion of the original system are not necessarily conserved in the simplified version. Additionally, the true error in these 'conserved' quantities is directly available for a given state trajectory by evaluating the quantity at a given time and subtracting the evaluation at the simulation's initial conditions.

For a system conserving energy and angular momentum, this error equation takes a simple form. The true state, $x(t) = \begin{bmatrix} q^T & \dot{q}^T \end{bmatrix}^T$, conserves these values for all time, while the state under the simplified system, $\bar{x}(t) = \begin{bmatrix} \bar{q}^T & \dot{\bar{q}}^T \end{bmatrix}^T$, does not necessarily do so.

$$\begin{bmatrix} \Delta C_H(t) \\ \Delta C_E(t) \end{bmatrix} = \begin{bmatrix} C_H(\bar{x}(t)) \\ C_E(\bar{x}(t)) \end{bmatrix} - \begin{bmatrix} C_H(x(t)) \\ C_E(x(t)) \end{bmatrix} = \begin{bmatrix} C_H(\bar{x}(t)) - C_H(\bar{x}(t_0)) \\ C_E(\bar{x}(t)) - C_E(\bar{x}(t_0)) \end{bmatrix} \tag{5.40}$$

Equations (5.23) and (5.25) can be linearized about the state $\bar{x}$, effectively producing a linear relationship of an exactly known error in C_E and C_H to small approximate errors in the states of the simplified system.

$$\begin{bmatrix} \Delta C_H(t) \\ \Delta C_E(t) \end{bmatrix} \approx \begin{bmatrix} \frac{\partial}{\partial q}C_H & \frac{\partial}{\partial \dot{q}}C_H \\ \frac{\partial}{\partial q}C_E & \frac{\partial}{\partial \dot{q}}C_E \end{bmatrix}_{\bar{x}} [\bar{x}(t) - x(t)]^T = H(t)\,\Delta x(t) \tag{5.41}$$

5.6 Simulation Results

This section studies an example formation under an assortment of simplifying assumptions regarding the motion of the center of mass. The original system models a two-vehicle formation with a constant force, K, acting along the separation vector in a nearly circular orbit about the Earth with an altitude of 700 km. This particular forcing model simulates the interaction due to a 100 W Photonic Laser Propulsion (PLP) system acting between the two vehicles.[56] This model is put to further use in Chapter 6. The parameters and initial conditions of the system are given by Table 5.1.

Table 5.1: Simulation parameters

Parameter	Value
μ	3.986×10^5 km^3/s^2
K	0.223 N
m_1	600 kg
m_2	600 kg
ρ_0	100 km
$\dot{\rho}_0$	0 km/s
γ_0	$\pi/2$ rad
$\dot{\gamma}_0$	0 rad/s
$r_{c,0}$	6752 km
$\dot{r}_{c,0}$	0 km/s
θ_0	0 rad
$\dot{\theta}_0$	1.138×10^{-3} rad/s

In addition to simulating the true dynamics of the system given by Eqs. (5.15), (5.16), (5.17), and (5.18), two sets of additional simulations integrate the equations of motion with particular constraints applied to the motion of

the center of mass as described in subsection 5.5.1 of section 5.5. The first set assumes that the center of mass travels on a Keplerian orbit determined by its initial conditions. The second set assumes that the center of mass travels on a path that it would follow for the same system without the internal force acting between the two vehicles. The time histories of the motion of the center of mass for both of these constrained sets of systems are available *a priori*, as they respectively represent the true Keplerian motion of a single mass and the averaged Keplerian motion of two masses. Within each of these two sets of assumptions regarding the motion of the center of mass, a further constraint is optionally included to enforce conservation of angular momentum as described in subsection 5.5.2.

Figure 5.3 depicts the error in the system states of the constrained system where the center of mass follows a Keplerian orbit. Similarly, Figure 5.4 depicts the error in the system states of the constrained system where the center of mass follows the weighted average of the Keplerian motion of the spacecraft without the PLP interaction. Each of these figures individually indicates that the state error of the constrained system is relatively independent of the decision to enforce conservation of angular momentum for the parameters and initial conditions described in Table 5.1. Comparison of the two figures likewise indicates that while both assumptions regarding the motion of the center of mass are similar in error magnitude for the relative position states, ρ and γ, the constrained system producing Fig. 5.4 results in lower state errors for the motion of the center of mass. Figure 5.5 interprets the state error produced by the simulation in terms of the error in the orbital parameters a_1, a_2, e_1, and e_2. While these four quantities do not alone allow for the full reconstruction of the system state, they do highlight significant differences in the error introduced by

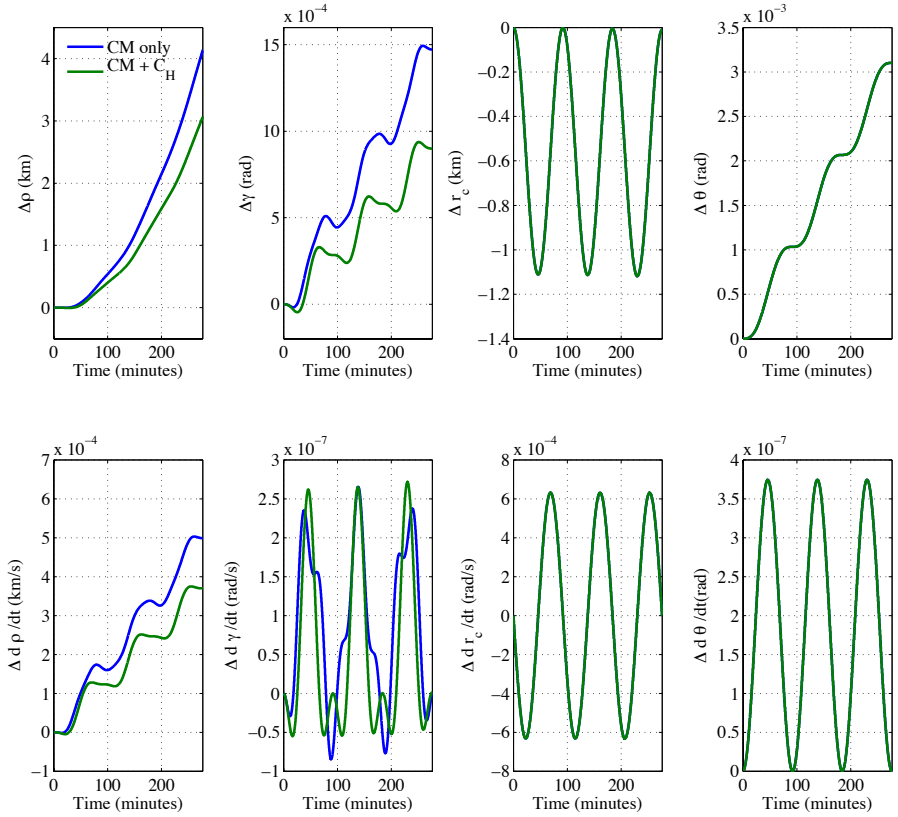

Figure 5.3: State errors due to simplifying the equations of motion by constraining the center of mass to follow a Keplerian orbit and conserve angular momentum.

the center of mass motion assumptions. Utilizing the averaged natural orbital motion of the system in the absence of the PLP input produces significantly lower errors in the evolution of the semimajor axes and eccentricities of the simulated system.

Figure 5.6 describes the true angular momentum and mechanical energy errors, ΔC_H and ΔC_E, and their linear approximations obtained from the simulation results of Figs. 5.3 and 5.4 in combination with Eq. (5.41). The errors

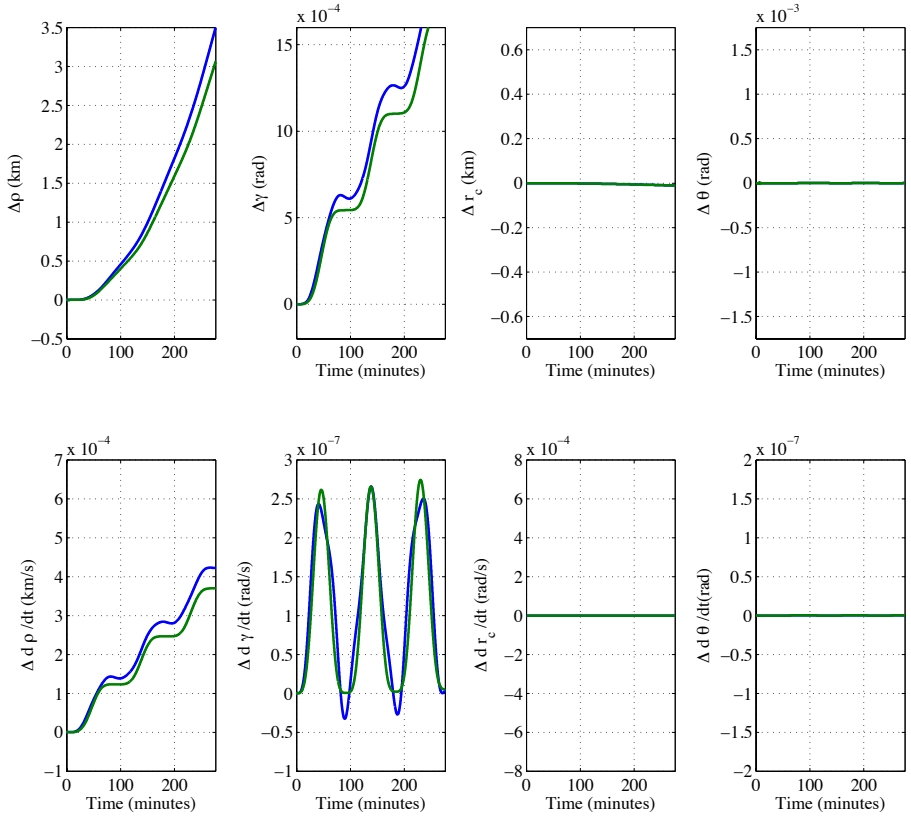

Figure 5.4: State errors due to simplifying the equations of motion by constraining the center of mass to follow its natural motion in the absence of PLP and conserve angular momentum.

observed in the integrals of motion could also be interpreted as how far the approximated motion drifts from the C_E surface in Fig. 5.2 given by Eq. (5.27) and the hyperdimensional surface defined by Eq. (5.30).

A close correlation between the time histories of the true and linear approximation of the error in these integrals of motion would indicate a valid linearizing approximation about the state of the constrained system. By conserving the angular momentum of the system, the system state is forced to

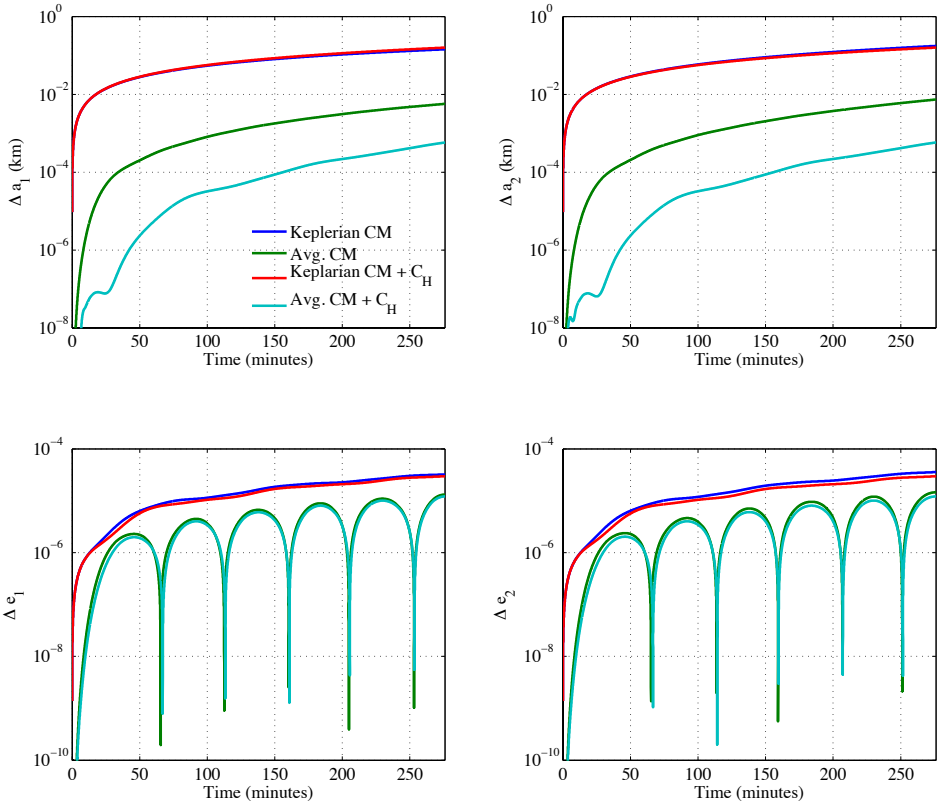

Figure 5.5: Errors in the semimajor axes a_1 and a_2 and eccentricities e_1 and e_2 due to the suite of assumptions regarding center of mass motion and angular momentum conservation.

conform to Eq. (5.25), and the corresponding combinations of orbital elements of the vehicles must also follow the relation described by Eq. (5.30). If similar constraints were imposed to conserve total energy, the same statements could be made regarding the system state and orbital elements with respect to Eqs. (5.23) and (5.27).

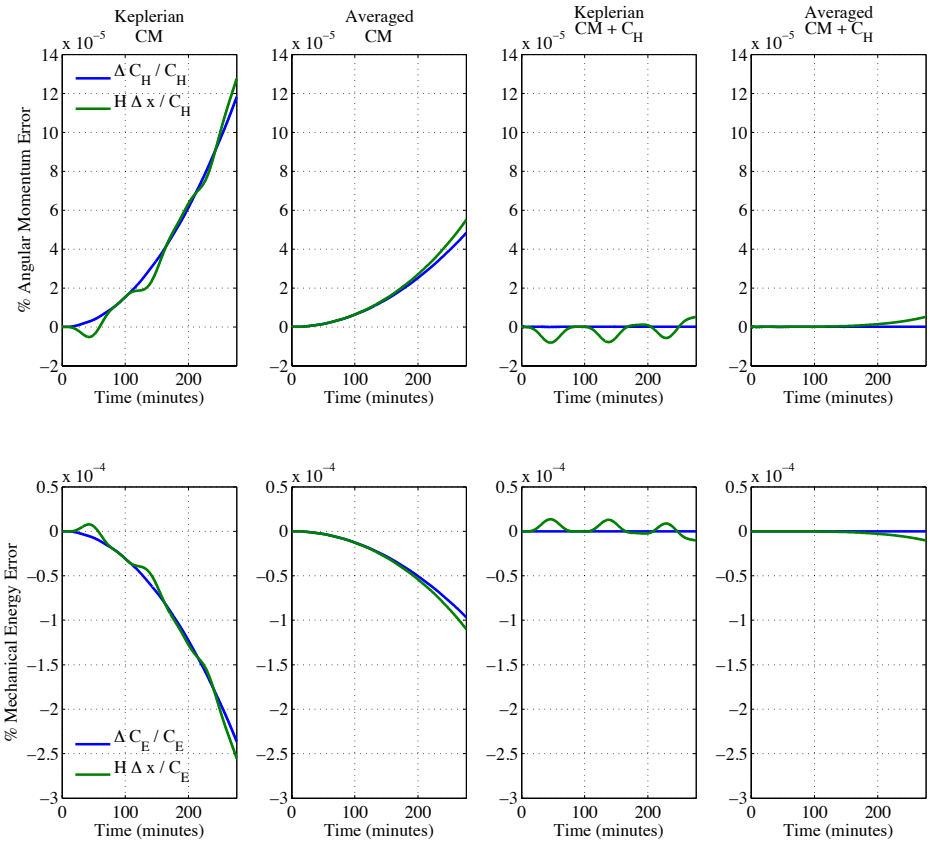

Figure 5.6: Comparing the true error of the integrals of motion, ΔC_E and ΔC_H, of the four simplified systems to the linear approximation of the error given by Eq. (5.41)

5.7 Conclusion

While the differential equations describing the motion of a two-vehicle formation utilizing a conservative, internal force in orbit about a common central body are yet to be solved analytically, integrals of motion exist for this system that bound the state trajectory. Two specific integrals of motion corresponding to mechanical energy and angular momentum are identified. As these time-invariant quantities remain conserved regardless of the choice

of generalized coordinates, they also describe relationships among a subset of the osculating orbital elements of the vehicles.

In addition to relating system states at two distinct times, these conservation laws are also potentially useful in evaluating formations under certain simplifying assumptions. Enforcing the integrals of motion to remain time-invariant allows for the continued use of their defining equations in the analysis of the simplified system state. Furthermore, the error of these integrals of motion due to constraint forces is exactly known for a given state and can be approximated by a linear relationship to the state error between the true and simplified system. Furthermore, the induced error in the integrals of motion can be interpreted as the distance to a hyperdimensional surface described by time-varying orbital elements. While these two integrals of motion described cannot completely determine the error in the individual states, they define mathematical relationships to which the error states must adhere.

CHAPTER 6

COUNTERING ATMOSPHERIC DRAG WITH NON-CONTACTING FORCES

We examine the utility of applying a force between a pair of non-contacting spacecraft for orbit change and maintenance maneuvers. These types of forces are internal to the overall system, allowing them to modify the angular momentum of the individual spacecraft while conserving the angular momentum of the system as a whole. By combining this type of forcing model with equations for the time derivatives of the orbital elements, we identify the relative configurations of the two spacecraft that modify the orbits in a desirable fashion. This type of inter-body interaction is applied to an example case of orbit maintenance in the presence of atmospheric drag.

6.1 Nomenclature

a_j semimajor axis of j^{th} spacecraft

C_j specific orbital energy of j^{th} spacecraft

Δa_j Effective increase in semimajor axis due to ΔV_j

ΔV_j magnitude of instantaneously applied additional velocity of j^{th} spacecraft

e_j eccentricity of j^{th} spacecraft

ϵ_j 6x1 matrix of orbital elements for j^{th} spacecraft

$\mathbf{F}_{Dj}$ environmental disturbance force applied to j^{th} spacecraft

$\mathbf{F}_{gj}$ force applied to j^{th} spacecraft

$\mathbf{F}_j$ additional external force applied to j^{th} spacecraft

The content of this chapter was presented at the 2009 *AIAA Guidance, Navigation, and Control Conference and Exhibition* under the title "Orbit Maneuvers Through Inter-satellite Forcing" (Ref. 57)

γ angle between $\mathbf{r}_2$ and $\mathbf{r}_1$

$\mathbf{h}_j$ specific angular momentum vector of j^{th} spacecraft

i_j inclination of j^{th} spacecraft

K arbitrary scalar function

M_{0j} Mean anomaly at epoch of the j^{th} spacecraft

m_j mass of j^{th} spacecraft

μ standard gravitational parameter of central body

n_j mean orbital rate of j^{th} spacecraft

ν_j true anomaly of j^{th} spacecraft

p_j semiparameter of j^{th} spacecraft

Ω_j longitude of ascending node of j^{th} spacecraft

ω_j argument of pericenter of j^{th} spacecraft

$\mathbf{r}_j$ position vector of j^{th} spacecraft

$\hat{\mathbf{r}}_j$ unit vector pointing from central body to j^{th} spacecraft

$\hat{\mathbf{s}}_j$ unit vector parallel to $\hat{\mathbf{w}}_j \times \hat{\mathbf{r}}_j$

T_j orbital period of j^{th} spacecraft

u_j argument of latitude of j^{th} spacecraft

V_j magnitude of inertial velocity vector of j^{th} spacecraft

$\hat{\mathbf{w}}_j$ unit vector aligned with orbit normal of j^{th} spacecraft

6.2 Introduction

Spacecraft relative motion is becoming a critical topic as missions begin to involve an increasing number of independent vehicles. This field encompasses multibody dynamics, perturbation analysis, formation flight, and technological advances in non-contacting interactions. Many have studied non-contacting

formation flight. Miller *et al* proposes stationkeeping via an electromagnetic interaction among vehicles.[17,44] Schaub *et al* considers a set of vehicles in orbit maintaining separation through electric charges on the spacecraft.[8,12] Chapters 3 and 4, along with work done by Shoer and Peck, focus on how to utilize the idea of flux pinning between a magnet and a superconductor to passively maintain separation in orbit.[27,58] Tragesser looks at what kind of formations are possible utilizing momentum exchange and radiation impingement.[59] All of these approaches apply a force internal to the set of spacecraft to modify the natural motions of the individual vehicles. Tragesser's work in particular applies to our area of interest, as it addresses a non-contacting force applied along a separation vector between vehicles and focuses upon the formation keeping aspects and linear stability analysis of such a non-contacting system.

These previous approaches utilize internal, non-contacting forces to effect a static formation through continuous forcing. Examining the result of a temporary application of this type of interaction informs a different class of problem: what kinds of orbit change maneuvers can be accomplished by allowing the spacecraft to spatially separate? Burns reexamines the classical perturbation equations in an effort to describes the effects of an extra forcing term on the time derivatives of the orbital elements in the two-body problem in physically meaningful quantities.[60] These perturbation equations provide insight into how the orbit of a spacecraft would evolve under the influence of a known force. Assuming the strength of this force and time of application are a user-controlled inputs to the system, these equations aid in the evaluation of particular control time-histories. Combining classical perturbation theory with a generalized description of these internal forces allows us to examine the effects of these interactions on the individual bodies and the system as a whole, with

the goal of devising maneuver strategies from them.

6.3 System Model

We consider two spacecraft on independent, closed orbits about a common central body in Fig. 6.1. These bodies interact via a generic force internal to the set of spacecraft and the orbital elements describing their motion change. The vector equations of motion describing this system are found by setting

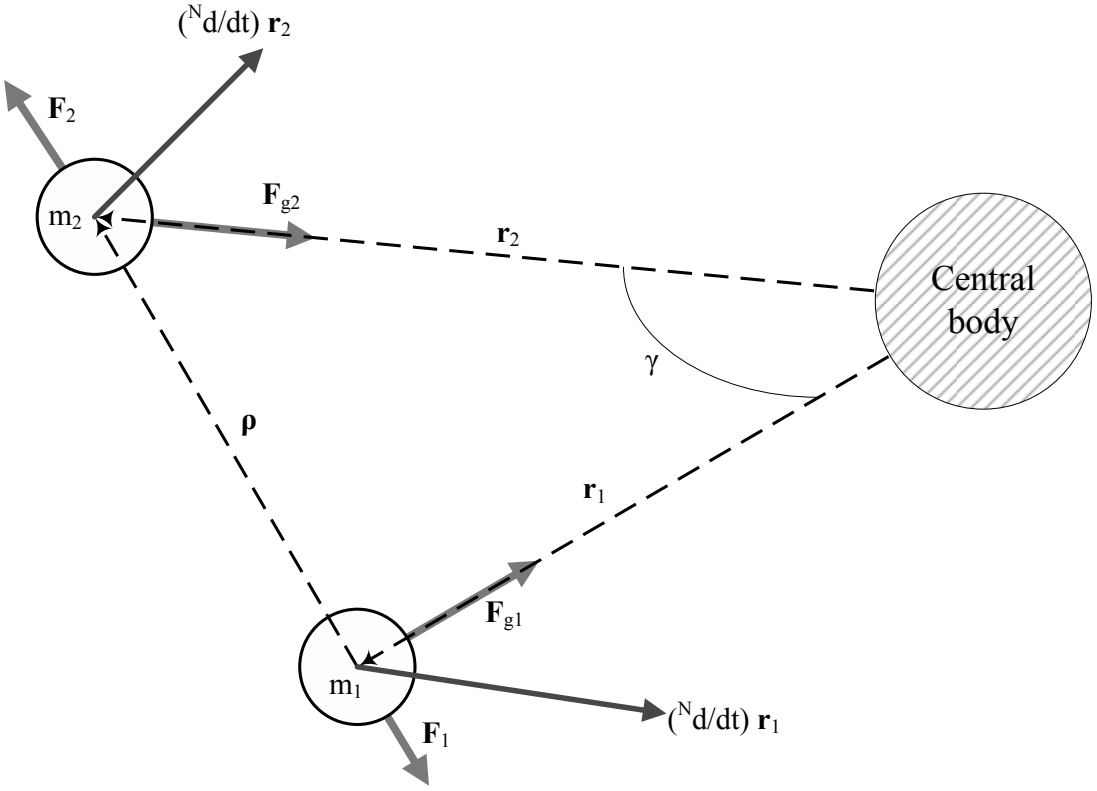

Figure 6.1: Free body diagram describing two point masses in orbit about a central body with a force internal to the system acting upon them

equal the time derivative of linear momentum with the forces acting upon the

objects. Considering only the gravitational attraction to a central point mass and an unspecified force internal to the system that acts between the two point masses with a strength of K, these equations take the following form:

$$\ddot{\mathbf{r}}_1 = \frac{1}{m_1}\left(\mathbf{F}_{g1} + \mathbf{F}_1\right) = -\frac{\mu}{r_1^3}\mathbf{r}_1 - \frac{K}{m_1}\frac{\boldsymbol{\rho}}{\rho} \tag{6.1}$$

$$\ddot{\mathbf{r}}_2 = \frac{1}{m_2}\left(\mathbf{F}_{g2} + \mathbf{F}_2\right) = -\frac{\mu}{r_2^3}\mathbf{r}_2 + \frac{K}{m_2}\frac{\boldsymbol{\rho}}{\rho} \tag{6.2}$$

where vector $\boldsymbol{\rho} = \mathbf{r}_2 - \mathbf{r}_1$ describes the relative position of the two bodies.

As an internal force in a multibody system cannot affect the total angular momentum of the system, we expect this vector to be constant before and after the actuation. While the sum of the angular momentum vectors remains constant, angular momentum can be exchanged among the bodies.

$$m_1\dot{\mathbf{h}}_1 = m_1\mathbf{r}_1 \times \ddot{\mathbf{r}}_1 = m_1\mathbf{r}_1 \times \left(-\frac{\mu}{r_1^3}\mathbf{r}_1 - \frac{K}{m_1}\frac{\boldsymbol{\rho}}{\rho}\right) = -K\mathbf{r}_1 \times \mathbf{r}_2 \tag{6.3}$$

$$m_2\dot{\mathbf{h}}_2 = m_2\mathbf{r}_2 \times \ddot{\mathbf{r}}_2 = m_2\mathbf{r}_2 \times \left(-\frac{\mu}{r_2^3}\mathbf{r}_2 + \frac{K}{m_2}\frac{\boldsymbol{\rho}}{\rho}\right) = K\mathbf{r}_1 \times \mathbf{r}_2 \tag{6.4}$$

$$m_1\dot{\mathbf{h}}_1 + m_2\dot{\mathbf{h}}_2 = 0 \tag{6.5}$$

Non-contacting inter-body forces are typically associated with a maximum effective range, ρ_{max}, determined by parameters specific to the system. When the separation between the pair of spacecraft is larger than ρ_{max}, the effects of the inter-body force are negligible or non-existent, and the evolution of the position and velocity of the spacecraft are governed by gravitational attraction and relevant environmental perturbations. As the separation distance drops below ρ_{max}, however, this additional forcing mechanism augments the dynamics of the system, allowing for modification of orbital elements and other relevant dynamical quantities. Describing these two modes of operation governed by different dynamics and the conditions that must be met to switch between them

establishes some of the basic components of a hybrid system model. Fitting this problem into a hybrid system model potentially opens up avenues of analysis ranging from state reachability to control synthesis.[61,62]

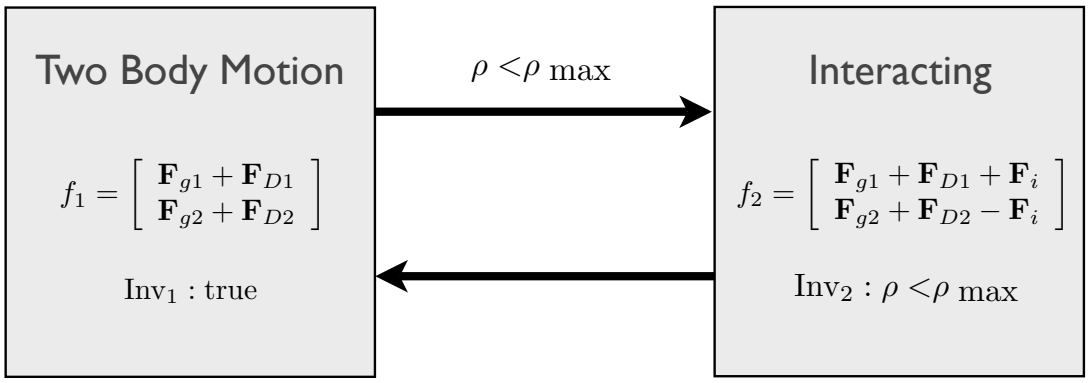

Figure 6.2: Basic depiction of a hybrid system model with two discrete modes of operation governed by different dynamics. In one mode, the dynamics are determined by gravitational attraction to the central body and modeled environmental disturbances. In the second mode, the dynamics are augmented by an inter-body force acting between the spacecraft. The hybrid system transitions between the two modes based on a comparison of the separation distance to a maximum value.

The separation distance ρ between the spacecraft depends upon the lengths of, and the angle between, the spacecraft position vectors measured from the central body.

$$\rho = r_1^2 + r_2^2 - 2r_1 r_2 \cos\gamma \tag{6.6}$$

Assuming simple Keplerian orbits in the absence of any perturbations, the evolution of the separation distance can be propagated forward in time and compared to ρ_{max} to determine at what points in time the two spacecraft are close enough to interact. The ability to interact, however, does not guarantee

that the result of the interaction would be favorable to a given target maneuver.

These possible interactions can be evaluated on the basis of how they would modify quantities of interest if the interaction were to take place. As this perturbing force affects the time derivative of the orbital elements and not the elements themselves, evaluating the sensitivity of these time derivatives to the parameters describing the interaction between two spacecraft indicates what qualitative changes in the system's state we should expect. Examining these sensitivities throughout the range of possible interactions allows one to select the relative configuration best suited to producing the desired changes in the resulting orbits of the spacecraft while minimizing changes deemed detrimental.

6.4 Sensitivities for Coplanar Orbits

If we consider the two spacecraft involved as point masses, we can describe their independent two-body motions as two sets of six orbital elements:

$$\begin{aligned} \epsilon_1 &= \begin{bmatrix} a_1 & e_1 & i_1 & \Omega_1 & \omega_1 & M_{01} \end{bmatrix}^T \\ \epsilon_2 &= \begin{bmatrix} a_2 & e_2 & i_2 & \Omega_2 & \omega_2 & M_{02} \end{bmatrix}^T \end{aligned} \tag{6.7}$$

Many authors have worked towards describing the evolution of orbital elements under perturbations in a clear and physically intuitive manner.[55,60,63] Several important parameters take particular forms while $e < 1$ and can be described in terms of orbital elements:

$$\mu = n_j^2 a_j^3 \tag{6.8a}$$

$$u_j = \omega_j + \nu_j \tag{6.8b}$$

$$h_j = n_j a_j^2 \sqrt{1 - e_j^2} \tag{6.8c}$$

$$C_j = -\frac{\mu}{2a_j} = \frac{v_j^2}{2} - \frac{\mu}{r_j} \tag{6.8d}$$

$$p_j = a_j \left(1 - e_j^2\right) \tag{6.8e}$$

$$r_j = \frac{p_j}{1 + e_j \cos \nu_j} \tag{6.8f}$$

$$T_j = 2\pi \sqrt{\frac{a_j^3}{\mu}} \tag{6.8g}$$

For coplanar orbits, The angle γ between the position vectors of the two spacecraft can then be described in terms of the argument of latitude:

$$\gamma = u_2 - u_1 \tag{6.9}$$

The perturbing accelerations described in Eq. (6.1) can be broken into scalar components:

$$\begin{aligned} \mathbf{A}_1 &= -\frac{K}{\rho m_1}\boldsymbol{\rho} \\ &= \frac{K}{\rho m_1}\left(r_1 - r_2 \cos\gamma\right)\hat{\mathbf{r}}_1 - \frac{K}{\rho m_1} r_2 \sin\gamma \hat{\mathbf{s}}_1 + 0\hat{\mathbf{w}}_1 \\ &= A_{r1}\hat{\mathbf{r}}_1 + A_{s1}\hat{\mathbf{s}}_1 \end{aligned} \tag{6.10}$$

where $\hat{\mathbf{r}}_1$ is a unit vector pointing from the central body to m_1, $\hat{\mathbf{w}}_1$ is a unit vector parallel to the orbit angular momentum, and $\hat{\mathbf{s}}_1 = \hat{\mathbf{w}}_1 \times \hat{\mathbf{r}}_1$. The corresponding perturbing acceleration applied to m_2 in Eq. (6.2) can be similarly decomposed:

$$\begin{aligned} \mathbf{A}_2 = \frac{K}{\rho m_2}\boldsymbol{\rho} &= \frac{K}{\rho m_2}\left(r_2 - r_1 \cos\gamma\right)\hat{\mathbf{r}}_2 + \frac{K}{\rho m_2} r_1 \sin\gamma \hat{\mathbf{s}}_2 + 0\hat{\mathbf{w}}_2 \\ &= A_{r2}\hat{\mathbf{r}}_2 + A_{s2}\hat{\mathbf{s}}_2 \end{aligned} \tag{6.11}$$

Consequently, we can combine the descriptions of the components of the accelerations with Eqs. (6.8a) - (6.8f) and equations for the time derivative of the orbital elements ϵ_1 and ϵ_2 found in Vallado.[63] Taking the partial derivatives of

these equations for $\dot{\epsilon}_1$ and $\dot{\epsilon}_2$ with respect to the strength of the interaction, K, provides the sensitivities we seek:

$$\frac{\partial}{\partial K}\frac{d}{dt}\epsilon_1 = \frac{1}{m_1\rho}\begin{bmatrix} \frac{2a_1^2}{h_1}\left(e_1\sin\nu_1\left(r_1 - r_2\cos\gamma\right) - p_1\frac{r_2}{r_1}\sin\gamma\right) \\ \frac{h_1}{\mu}\left(e_1\sin\nu_1\left(r_1 - r_2\cos\gamma\right) - \left(\cos\nu_1 + \frac{r_1}{p_1}\left(e_1 + \cos\nu_1\right)\right)r_2\sin\gamma\right) \\ 0 \\ 0 \\ \frac{-h_1}{\mu e_1}\left(\cos\nu_1\left(r_1 - r_2\cos\gamma\right) + \left(1 + \frac{r_1}{p_1}\right)r_2\sin\nu_1\sin\gamma\right) \\ \frac{n_1 a_1}{\mu e_1}\left(\left(p_1\cos\nu_1 - 2e_1 r_1\right)\left(r_1 - r_2\cos\gamma\right) + \left(p_1 + r_1\right)r_2\sin\nu_1\sin\gamma\right) \end{bmatrix} \tag{6.12}$$

$$\frac{\partial}{\partial K}\frac{d}{dt}\epsilon_2 = \frac{1}{m_2\rho}\begin{bmatrix} \frac{2a_2^2}{h_2}\left(e_2\sin\nu_2\left(r_2 - r_1\cos\gamma\right) + p_2\frac{r_1}{r_2}\sin\gamma\right) \\ \frac{h_2}{\mu}\left(e_2\sin\nu_2\left(r_2 - r_1\cos\gamma\right) + \left(\cos\nu_2 + \frac{r_2}{p_2}\left(e_2 + \cos\nu_2\right)\right)r_1\sin\gamma\right) \\ 0 \\ 0 \\ \frac{-h_2}{\mu e_2}\left(\cos\nu_2\left(r_2 - r_1\cos\gamma\right) - \left(1 + \frac{r_2}{p_2}\right)r_1\sin\nu_2\sin\gamma\right) \\ \frac{n_2 a_2}{\mu e_2}\left(\left(p_2\cos\nu_2 - 2e_2 r_2\right)\left(r_2 - r_1\cos\gamma\right) - \left(p_2 + r_2\right)r_1\sin\nu_2\sin\gamma\right) \end{bmatrix} \tag{6.13}$$

Similar sensitivities can be derived for quantities such as angular momentum, orbital energy, and orbital period in terms of sensitivities and orbital elements:

$$\frac{\partial}{\partial K}\frac{d}{dt}h_j = \frac{1}{2h_j}\left(\left(1 - e_j^2\right)\left(\frac{\partial}{\partial K}\frac{d}{dt}a_j\right) - 2a_j e_j\left(\frac{\partial}{\partial K}\frac{d}{dt}e_j\right)\right) \tag{6.14}$$

$$\frac{\partial}{\partial K}\frac{d}{dt}C_j = \frac{\mu}{2a_j^2}\left(\frac{\partial}{\partial K}\frac{d}{dt}a_j\right) \tag{6.15}$$

$$\frac{\partial}{\partial K}\frac{d}{dt}T_j = 3\pi\sqrt{\frac{a_j}{\mu}}\left(\frac{\partial}{\partial K}\frac{d}{dt}a_j\right) \tag{6.16}$$

Figure 6.3 plots the separation distance between two nearly-circular orbits, along with the corresponding sensitivity plots for $\dot{a}_1$ and $\dot{e}_1$ as an example of the interaction selection. The separation plot indicates two possible periods when the interaction between the spacecraft can be utilized. Within these two periods, we find that each of these opportunities would result in very different changes

to $\dot{a}_1$ and $\dot{e}_1$. One might, for example, care to only interact during times where the a_1 would increase and e_1 would decrease. Examining these sensitivities allows us to select the times over which this combination of desired outcomes could be achieved. A simple "Bang-Off" controller could be developed that uses this logic. Another subtlety to these systems is that each interaction should ideally set up future interactions so they, too, could effectively work towards some user-defined target end-state. For example, the interactions have the potential to change the semimajor axes of the vehicles, the orbit periods, and the interaction times. In short, the interactions need not only work towards the target orbits of the spacecraft but also ensure the "health" of the system at each step along the way. Balancing and quantifying these requirements represent the next major step along the path to applying this concept to complex orbit problems.

6.5 Simulation Results

This section endeavors to demonstrate the utility of this inter-satellite forcing arrangement through an example mission. Two spacecraft are placed in low-altitude orbits, and internal forcing is used to counteract atmospheric drag. Atmospheric drag plays a crucial role in determining the operational lifetime of spacecraft in low-altitude orbits.[64] Typical solutions to the drag problem are to either restrict the spacecraft to higher-altitude orbits or expend fuel. Both solutions represent a reduction in the mission design space.

Some configurations of spacecraft utilizing these inter-satellite forces, however, may relax the minimum altitude restrictions and fuel expenditure.

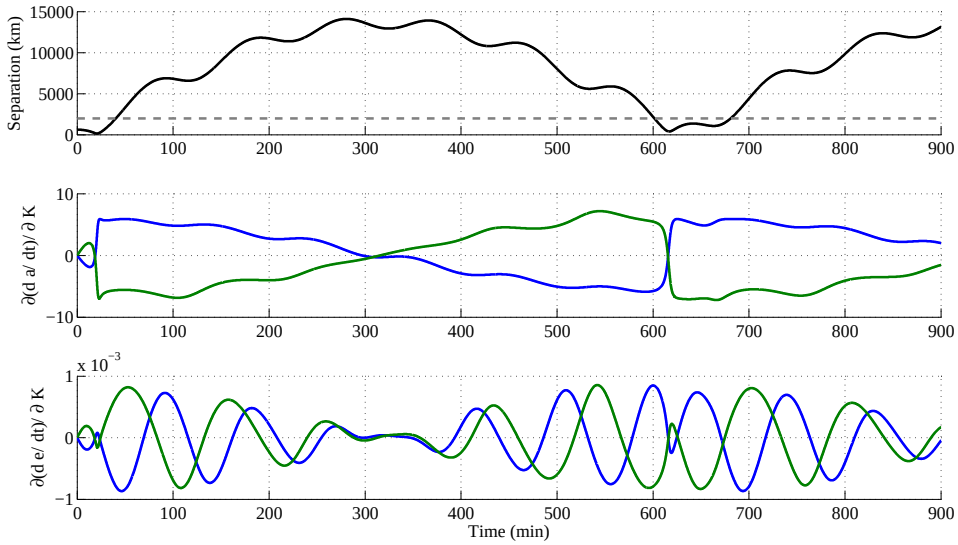

Figure 6.3: *Top*: Plot of separation distance between spacecraft for example case as a function of time without inter-satellite forcing active, and the maximum interaction distance, ρ_{max}. When the plot of the separation distance drops below the line representing ρ_{max}, an interaction can theoretically take place, and the sensitivities of relevant parameters to K, should be examined. *Middle*: A plot of the sensitivity of the semimajor axis of each spacecraft to the inter-satellite forcing strength, K, against time. *Bottom*: A plot of the sensitivity of the orbit eccentricity of each spacecraft to K, against time.

Many of the current technological options for inter-satellite forcing are based on electrical propulsion concepts. Photonic Laser Propulsion (PLP), for example, is a low-thrust, high-I_{sp}, long-range, propellentless propulsion option currently being developed.[56] Utilizing this technology for orbit maneuvers or maintenance would require either continuous or periodic actuation in order to produce useful effects. A pair of spacecraft in similar-sized, circular, coplanar orbits with one having posigrade and the other retrograde motion must pass each other twice per orbit, guaranteeing that opportunities arise for these

interactions to take place as long as we maintain this orbit geometry.

Aside from potentially providing two forcing opportunities per orbit, examination of Eqs. (6.3), (6.4), and (6.5) for this configuration shows that if the forcing takes place as the spacecraft recede from each other, the magnitude of the angular momentum of each spacecraft will increase, resulting in an increase of semimajor axis. This change can also be seen by examining the time derivative of orbital energy described in in Eq. (6.8d), or by examination of the relevant portion of Eqs. (6.12) and (6.13).

Table 6.1 describes the parameters that allow us to set up a simulation of this hybrid system model for a pair of spacecraft in LEO. A PLP system provides an example inter-body force between the two spacecraft and a simple exponential model of the atmosphere with coefficients taken from Vallado produces a drag force on the spacecraft.[63] Here, we increase the strength of the interaction, K,

Table 6.1: Example Orbit and Vehicle Parameters

Parameter	Value
Initial Altitude	400 km
ρ_{max}	2000 km
Vehicle Mass	300 kg
Ballistic Coefficient	22.7 kg/m^2
K	17 – 51 mN

above the experimental setup described by Bae in anticipation of technological developments to implement PLP on the spacecraft scale.[56] A range of constant thrust magnitudes are evaluated.

Prior to initializing a simulation, we examine the predicted periods of

interaction and how the interaction should affect the spacecraft orbit states. During each of those possible interaction times, we predict the relevant sensitivities using Eqs. (6.12) and (6.13). For this example case, we are interested in maintaining the size of the orbit, so we examine the sensitivity of the time derivatives of the semimajor axes of the spacecraft to the inter-satellite force. In the absence of perturbations, the spacecraft follow deterministic Keplerian orbits, and the periods of possible interaction are easily identified without numerical integration.

Figure 6.4 plots these sensitivities for our example mission. An interesting side effect of this configuration is that each potential interaction is identical to the others in terms of their effect on semimajor axis. There is no immediate benefit in choosing a later interaction than the first available. From these plots, we choose to interact only at times when the sensitivity of $\dot{a}_1$ and $\dot{a}_2$ to K is positive, corresponding to the range of times just after a closest approach until the separation distance reaches ρ_{max}.

Once the first interaction has been described, the dynamics of the hybrid system model are propagated forward until after the first interaction has completed and the spacecraft are back in their non-interacting mode. The separation distance and sensitivity plots can then be generated for the then-current orbit conditions to determine the best second interaction time and the process repeated.

Figure 6.5 depicts the simulation time histories of the semimajor axes and the orbit radius at perigee of the two spacecraft. As expected, the inter-satellite force causes sharp periodic increases in a_1 and a_2, allowing it to counteract the gradual decline due to atmospheric drag. As the interactions are for very short

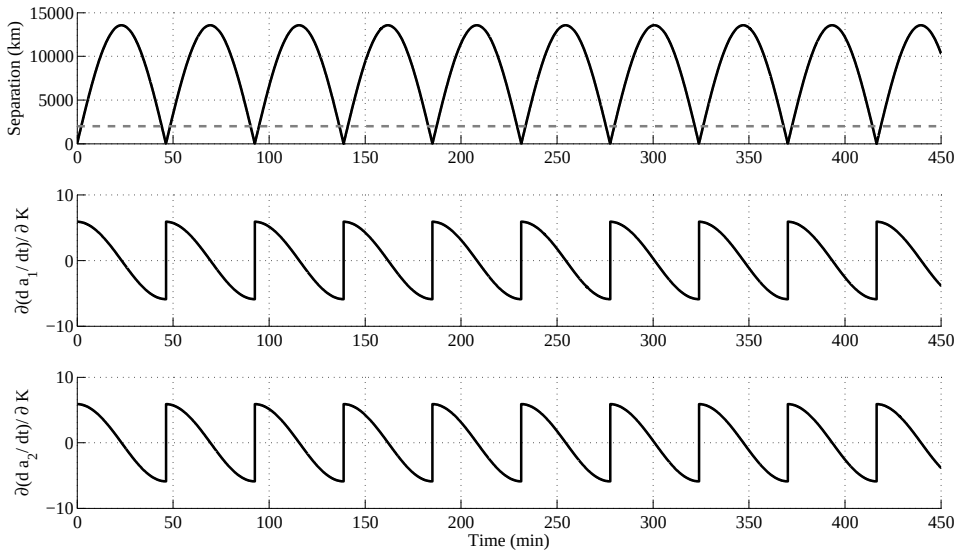

Figure 6.4: *Top*: Plot of separation distance between spacecraft for example case as a function of time in the absence of an inter-body force, and the maximum interaction distance, ρ_{max}. When the plot of the separation distance drops below the dashed line representing ρ_{max}, an interaction can theoretically take place, and the sensitivities of relevant parameters to K, should be examined. *Middle*: A plot of the sensitivity of the semimajor axis of spacecraft 1 to the inter-satellite forcing strength, K, against time. *Bottom*: A plot of the sensitivity of the semimajor axis of spacecraft 2 to K, against time. These plots indicate that with each possible encounter between the spacecraft, they can both decrease their semimajor axis by interacting before they pass each other and the separation distance begins to grow, or they can both increase their semimajor axis by interacting after the pass.

durations compared to the orbit period, we can examine the effective tangential ΔV applied to a spacecraft over a single interaction. Through manipulation of the orbital energy equations the ΔV applied is a solution of the following

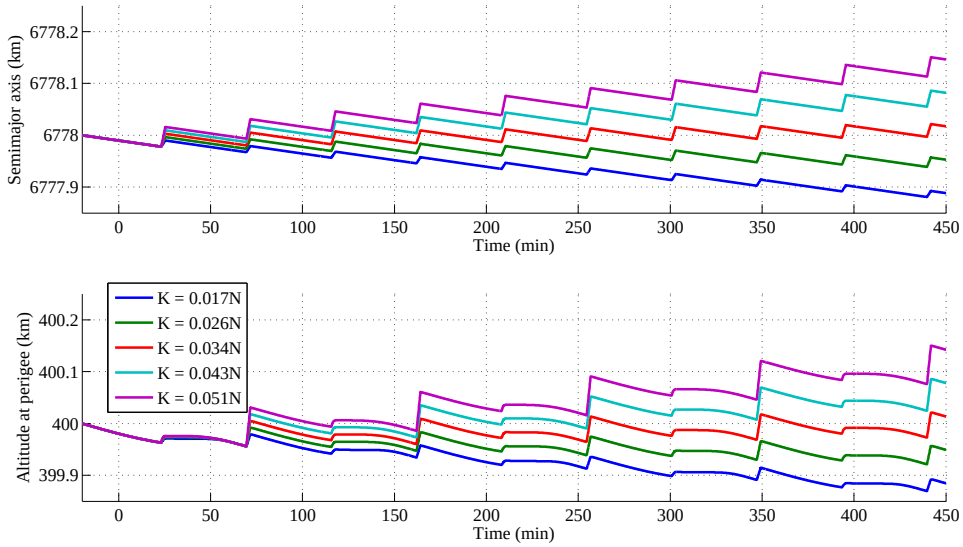

Figure 6.5: *Top*: Simulation time history of the semimajor axis of both spacecraft. *Bottom*: Simulation time history of the radius at perigee of both spacecraft. The configuration in orbit causes the evolution of these parameters to be virtually identical.

quadratic equation:

$$C_{j,init} - C_{j,fin} = \frac{-\mu}{2a_j} + \frac{\mu}{2\left(a_j + \Delta a_j\right)} = \frac{V_j^2}{2} - \frac{\mu}{r_j} - \frac{\left(V_j + \Delta V_j\right)^2}{2} + \frac{\mu}{r} \tag{6.17}$$

$$\frac{\mu}{2}\left(\frac{1}{a_j + \Delta a_j} - \frac{1}{a_j}\right) = -\frac{2V_j\Delta V_j + \Delta V_j^2}{2} \tag{6.18}$$

$$\Delta V_j^2 + 2V_j\Delta V_j + \mu\left(\frac{1}{a_j + \Delta a_j} - \frac{1}{a_j}\right) = 0 \tag{6.19}$$

For our simulation, the equivalent tangential ΔV applied over a single interaction is $\Delta V = 0.0141$ m/s, for a total of 160 m/s applied per year. This is comparable to the ΔV per year required for a satellite of this ballistic coefficient to maintain its altitude.[64]

6.6 Conclusion

New developments in non-contacting interfaces have typically been thought of in terms of how they could be used to aid the formation flight task of vehicle stationkeeping. We propose using non-contacting forces to effect orbit change maneuvers for individual vehicles by pushing off from other bodies in orbit. The differential equations describing the evolution of the orbital elements form the basis of our analysis. We couple the multibody dynamics through force interactions. As these inter-satellite forces are limited in their operational range, the dynamics of the system make discrete switches between two modes of operation and can be modeled in the framework of a hybrid system.

The key to designing a successful spacecraft pair utilizing these inter-satellite forces lies in the appropriate selection of interaction opportunities. The conditions upon the sensitivities of particular parameters to the inter-satellite force enter into the hybrid system model by augmenting the conditions that must be met to switch from one mode of operation to another. With *a priori* knowledge of the interaction states and times, one can ensure that the orbits of the spacecraft evolve as desired.

The motivating example of orbit maintenance in the presence of atmospheric drag demonstrates the utility of this type of system to a real-world challenge. The simulation suggests the capability to maintain two spacecraft in LEO indefinitely-rather than their predicted lifetime, which is on the order of months.[64] Using PLP as an example inter-body force, this arrangement offers the cability to place two spacecraft in a lower-altitude orbit for an indefinite lifetime and no fuel consumption. Through frequent, short interactions, this

relatively weak force is able to produce an important change.

We have developed a set of analysis tools for non-contacting pairs of spacecraft with an inter-satellite force based upon the concept of the sensitivity of relevant orbit parameters to the force strength. These tools allow for the design of configurations that would produce the changes desired to reach a particular goal from an initial state. Future work for this topic includes the expansion of these tools to include controllability, reachability, and observability analyses for these hybrid systems, and for the further development of conditions upon these interactions to maintain system health while working towards a target state.

CHAPTER 7

IN-ORBIT ESTIMATION OF INERTIA AND MOMENTUM-ACTUATOR ALIGNMENT PARAMETERS

Knowledge of the mass distribution and momentum-actuator alignment parameters of a spacecraft is vital to the control of it's attitude motion. The difficulty of measuring the complete set of these quantities prior to launch along with the potential for changes in the spacecraft mass distribution during operations suggests the utility of estimating these parameters in-orbit from available telemetry data. This paper develops a series of possible on-board parameter estimation schemes based on measurement equations describing the angular momentum and kinetic energy states of the rigid-body system. The performance of the algorithms is compared over both a simulated maneuver and a series of data sets from the MESSENGER spacecraft.

7.1 Nomenclature

a_i	Axis of rotation of the i^{th} reaction wheel in body coordinates $\begin{bmatrix} a_{ix} & a_{iy} & a_{iz} \end{bmatrix}^T$
B	A $3m \times 6$ block matrix depending on the measured body rates of a spacecraft
$\bar{c}$	Current best knowledge of arbitrary variable c
f	Discrete-time dynamics function
F_k	State transition matrix between times t_k and t_{k+1}
h	Total angular momentum of a spacecraft in inertial coordinates
H_k	Linearized measurement matrix at time t_k

The content of this chapter has been accepted for publication by the *Journal of Guidance, Control, and Dynamics* and is awaiting publication under the same title (Ref. 65).

$\mathcal{H}$ Discrete-time measurement function

J A $3m \times 3m$ block matrix depending on the measured attitudes of a spacecraft

I Body-fixed spacecraft inertia matrix

$\tilde{I}$ Reorganized inertia parameters $\begin{bmatrix} I_{xx} & I_{yy} & I_{zz} & I_{xy} & I_{xz} & I_{yz} \end{bmatrix}^T$ in body coordinates

$I_{w,i}$ Moment of inertia of the i^{th} reaction wheel

$\sum M$ Sum of external torques acting on a rigid body

n Number of reaction wheels

$\mathcal{O}$ Observability Gramian

p_i Two-parameter Modified Rodriquez Parameter representation of the alignment error of the i^{th} reaction wheel $\begin{bmatrix} p_{i1} & p_{i2} \end{bmatrix}^T$

P Stacked reaction wheel alignment errors $\begin{bmatrix} p_1^T & \cdots & p_n^T \end{bmatrix}^T$

$\hat{Q}$ A $3m \times 3$ block matrix depending on the measured attitudes of a spacecraft

${}^kQ^N$ Direction cosine matrix between an inertially-fixed coordinate set and body coordinates at time index k

${}^kQ^{gi}$ Direction cosine matrix between guessed momentum-actuator coordinates and body coordinates at time index k

T_k Rotational kinetic energy of a rigid body at time t_k

u Discrete-time dynamics input

v Discrete-time process noise

w Discrete-time measurement noise

W A $3m \times 2n$ block matrix depending upon the measured wheel speeds and actuator alignments

W_k Discrete-time measurement noise input matrix

x,y,z Spacecraft body axes

x_e	Estimation state
z_e	Discrete-time system measurement. z_h is an angular momentum measurement and z_T is a kinetic energy measurement
1_j	$j \times j$ identity matrix
Γ_k	Discrete-time process noise input matrix at time t_k
$\phi\left(t_j, t_k\right)$	State transition matrix between times t_k and t_j
Ω	Stacked reaction-wheel speeds $\left[\Omega_1 \quad \cdots \quad \Omega_n\right]^T$
ω	Spacecraft body rate expressed in body coordinates
σ	Standard deviation of a random variable
θ	A 3×1 matrix of small angular rotations about orthogonal axes

7.2 Introduction

Successful spacecraft attitude control and general operations are typically predicated upon knowledge of the mass distribution of the spacecraft and the alignment of relevant actuators. The mass distribution, in the form of a body-fixed inertia matrix, can be predicted to a limited extent by summing contributions from individual components on the basis of their assumed locations. This component-level knowledge, however, is not necessarily always available or accurate (e.g., in the cases of a broken appendage or of modeling fuel distribution, respectively). Modeling errors introduced in the form of an inaccurate mass distribution produce inaccurate predictions of attitude motion under feedback control, resulting in a mismatch between desired and actual spacecraft-pointing performance. Residual attitude-actuator alignment errors after hardware integration and testing can similarly affect closed-loop pointing performance. Developing the capability to estimate

these inertia parameters and actuator-alignment errors in-orbit would not only aid in optimizing spacecraft pointing performance but also provide a means to diagnose erroneous or unexpected rigid-body attitude motion due to mass distribution changes, such as a failed deployment, or attitude-actuator misalignments.

The literature suggests several approaches to estimating these parameters from spacecraft telemetry data. One general set of methods makes use of the rigid body attitude equations of motion described by Euler's equation.

$$I\dot{\omega} + \omega^x I\omega = \sum M \tag{7.1}$$

$$\text{where } \omega^x = \begin{bmatrix} 0 & -\omega_z & \omega_y \\ \omega_z & 0 & -\omega_x \\ -\omega_y & \omega_x & 0 \end{bmatrix}$$

Bergman, Walker, and Levy developed a second-order filter to extract rigid body inertia parameters using Eq. (7.1) that neglected the gyroscopic term in the presence of known thruster inputs and external disturbances, and they tested it on simulated Shuttle orbiter maneuvers.[66] Wilson, Sutter, and Mah similarly developed a filter producing inertia parameters and thruster modeling based on Eq. (7.1) but chose to include the gyroscopic term.[67] Thienel, Luquette, and Sanner developed an adaptive attitude control algorithm based on Eq. (7.1) that concurrently yields an estimate of the spacecraft inertia parameters.[68] Fosbury and Nebelecky limited their approach to determining actuator-alignment parameters in the presence of a known mass distribution noisy telemetry data.[69] As noted by Fosbury and Nebelecky, methods using Eq. (7.1) as the basis for a measurement equation necessarily make use of the time derivative of the body rotation rate, $\dot{\omega}$, a quantity that must be either derived from numerical differentiation or by comparing accelerometer outputs

relative to an estimated center of mass. The amplification of noise introduced in this process either in numerical differentiation or through the center of mass estimate and accelerometer output limits the quality of the estimates produced.

Tanygin and Williams suggested a second approach to the problem of inertia parameter estimation that integrates a projection of the rigid body dynamics to produce an equation relating the rotational kinetic energy of the spacecraft at two times $\tau = 0$ and t to the work done by the actuator inputs.[70]

$$\frac{1}{2}\omega^T I\omega\Big|_t = T|_0 + \int_0^t \omega^T \sum M d\tau \tag{7.2}$$

This projection removes the gyroscopic term and allows for the inertia parameters to enter the measurement equation linearly, naturally lending itself to the formulation of a batch least-squares estimation problem. Tanygin and Williams successfully tested the algorithm on simulated and actual data produced by the Simplified Aid for EVA Rescue (SAFER) system.[70] The algorithm depends, however, upon knowledge of the initial kinetic energy and the accuracy of the numerical integration scheme used to produce the work done by the torque inputs. Simple implementations of such a numerical integration technique requires a small, fixed time step between measurements, especially in the case of a recursive, on-board estimation scheme.

A third approach instead examines the angular momentum of the spacecraft, corresponding to the integral of Eq. (7.1) with respect to time. Under the specialized case where external torques can be neglected, the total angular momentum vector of the spacecraft remains inertially fixed:

$${}^N Q^k \left(I\omega + \sum I_{w,i}\Omega_i a_i\right)\Big|_k = {}^N Q^j \left(I\omega + \sum I_{w,i}\Omega_i a_i\right)\Big|_j \tag{7.3}$$

Peck introduced the use of conservation of angular momentum, described by Eq. (7.3), as the basis of a batch least-squares estimator for spacecraft inertia

parameters.[71–73] The scheme operates by comparing the calculated momentum state at two distinct times and generating suitable inertia parameters by minimizing the resulting error. A distinct advantage of this approach over others is the ability to compare measurements with arbitrary temporal spacing. Peck extended this approach by incorporating the gravity-gradient torque as a known external input.[74] A version of a momentum-based approach with momentum actuators was successfully tested on Cassini flight data.[75] Psiaki further developed this method by including reaction wheel and magnetic torquer alignment and scaling parameters, and he applied it to data from the Wilkinson Microwave Anisotropy Probe (WMAP) spacecraft.[76] Whereas Psiaki compared sequential angular velocity, spacecraft attitude, and actuator input states, in general, the optimal choice of time indices to compare in Eq. (7.3) is unclear: comparing states with large temporal separations may violate the assumption of conservation of angular momentum, but small separations may not provide sufficient information during coasting maneuvers.

This paper proposes a novel momentum-based estimation scheme for inertia and reaction-wheel alignment parameters that addresses several concerns raised by the above approaches. The scheme takes a recursive form and simultaneously estimates the momentum, inertia parameters, and actuator alignment in the presence of additive noise in the spacecraft attitude-dynamics states. Because the measurement equation that describes the angular momentum of the spacecraft is of a form similar to that of Eq. (7.3) rather than torque balance in the form of Eq. (7.1), no numerical time derivatives of wheel speeds or body rates are necessary, and non-uniform temporal separation between measurements is acceptable. Inclusion of the angular momentum state allows for the development of a measurement equation comparing the

calculated angular momentum at a single time index to a simultaneously developed "optimal" angular momentum estimate.

Several variations of the parameter estimator are developed, incorporating different combinations of estimated states and measurement equations. The paper first describes the development of the estimation algorithm and then examines the performance of the proposed algorithm over a simulated maneuver and a series of calibration maneuver data sets from the MErcury Surface, Space ENvironment, GEochemistry, and Ranging (MESSENGER) spacecraft. The paper ends with a summary of the algorithm performance and discussion of the results.

7.3 Algorithm Development

Developing an estimation scheme first requires a suitable description of the measurements observed and the dynamics equations describing the estimator-state time evolution. In the case of the inertia and actuator-alignment parameter estimation problem, the state dynamics are modeled as a discrete-time system, allowing for the implementation of several standard sub-optimal filtering approaches, such as an Extended Kalman Filter (EKF) or Extended Square-Root Information Filter (ESRIF):

$$\begin{aligned} x_e(k+1) &= f(x_e(k), u(k), v(k)) \\ &\approx f(\bar{x}_e(k), u(k), 0) + \left[\frac{\partial f}{\partial x_e}\right]_k (x_e(k) - \bar{x}_e(k)) + \left[\frac{\partial f}{\partial v}\right]_k v(k) \\ x_e(k+1) - \bar{x}_e(k+1) &= F_k(x_e(k) - \bar{x}_e(k)) + \Gamma_k v(k) \\ z_e(k) &= h(x_e(k), w(k)) \end{aligned} \tag{7.4}$$

$$\approx \mathcal{H}\left(\bar{x}_e\left(k\right),0\right)+\left[\frac{\partial \mathcal{H}}{\partial x_e}\right]_k\left(x_e\left(k\right)-\bar{x}_e\left(k\right)\right)+\left[\frac{\partial \mathcal{H}}{\partial w}\right]_k w\left(k\right)$$

$$z_e\left(k+1\right)-\bar{z}_e\left(k+1\right)=H_{k+1}\left(x_e\left(k+1\right)-\bar{x}_e\left(k+1\right)\right)+W_k w\left(k+1\right) \tag{7.5}$$

This paper develops six variations of a recursive inertia estimation algorithm based on an EKF. The first and second of these correspond to recursive formulations of an inertia estimation scheme using only the rotational kinetic energy balance from Eq. (7.2) or the conservation of angular momentum expressed in Eq. (7.3). The third estimator incorporates both the rotational kinetic energy and angular momentum states and measurement equations to produce an estimate of the inertia parameters. The fourth, fifth, and sixth estimators are identical to the initial three with the addition of the momentum-actuator alignment parameters. Table 7.1 summarizes the variations in the estimated states and measurement equations utilized.

Table 7.1: Estimator variation descriptions

	Variant 1	Variant 2	Variant 3	Variant 4	Variant 5	Variant 6
$x_e =$	$\begin{bmatrix} T_k \\ \tilde{I} \end{bmatrix}$	$\begin{bmatrix} h \\ \tilde{I} \end{bmatrix}$	$\begin{bmatrix} h \\ T_k \\ \tilde{I} \end{bmatrix}$	$\begin{bmatrix} T_k \\ \tilde{I} \\ P \end{bmatrix}$	$\begin{bmatrix} h \\ \tilde{I} \\ P \end{bmatrix}$	$\begin{bmatrix} h \\ T_k \\ \tilde{I} \\ P \end{bmatrix}$
$z_e =$	$\begin{bmatrix} T_k \end{bmatrix}$	$\begin{bmatrix} h \end{bmatrix}$	$\begin{bmatrix} h \\ T_k \end{bmatrix}$	$\begin{bmatrix} h \\ T_k \end{bmatrix}$	$\begin{bmatrix} h \\ T_k \end{bmatrix}$	$\begin{bmatrix} h \\ T_k \end{bmatrix}$

The body rates and reaction-wheel speeds reported in the telemetry data are assumed to be corrupted by additive, zero-mean noise that follows a normal distribution. Similarly, the direction cosine matrix ${}^kQ^N$ describing the attitude of the spacecraft with respect to an inertial reference is assumed to be multiplied

by an error rotation matrix that can be represented as a small-angle rotation about an arbitrary axis:

$$\begin{aligned} \Omega(k) &= \bar{\Omega}(k) + \Delta\Omega(k) & \Delta\Omega(k) &\sim \mathcal{N}\left(0, \sigma_\Omega^2 [1_n]\right) \\ \omega(k) &= \bar{\omega}(k) + \Delta\omega(k) & \Delta\omega(k) &\sim \mathcal{N}\left(0, \sigma_\omega^2 [1_3]\right) \\ {}^kQ^N = \Delta Q(k)\, {}^k\bar{Q}^n &\approx (1_3 - \Delta\theta^x(k))\, {}^k\bar{Q}^N & \Delta\theta(k) &\sim \mathcal{N}\left(0, \sigma_\theta^2 [1_3]\right) \end{aligned} \tag{7.6}$$

The estimation schemes developed in this paper do not include states associated with the attitude dynamics variables and therefore rely upon a separate filtering scheme to provide estimates of the attitude quaternion, spacecraft angular velocity, and wheel speeds based off measurements from the relevant hardware sensors. Feeding the sensor output directly into the inertia and momentum-actuator alignment parameter estimators would likely result in a violation of the noise descriptions of (7.6). The literature contains a plethora of filtering options to address the attitude variable filtering problem, and their design is beyond the scope of this paper.[77–81]

7.3.1 Measurement Equations

In the absence of external torques, the total angular momentum of the spacecraft remains inertially fixed and is determined by the sum of contributions from the spacecraft bus and momentum actuators. Because the body rates and reaction-wheel speeds are reported in body-fixed coordinates, the calculation incorporates the spacecraft attitude with respect to inertially fixed references coordinates to rotate the angular momentum to the body-fixed coordinates.

$$z_h(k) = 0 = I\omega(k) - {}^kQ^N h + \sum I_{w,i}\Omega_i(k)\, a_i \tag{7.7}$$

Linearizing Eq. (7.7) about current estimates of the angular momentum, inertia, and actuator-alignment parameters, along with the descriptions of $\bar{a}_i$ and $[\partial a_i/\partial p_i]$ (see Appendix B) equations(B.8) and (B.9), reformats the measurement to match Eq. (7.3):

$$z_h(k) \approx \bar{z}_h(k) + \begin{bmatrix} -{}^k\bar{Q}^N & \tilde{\bar{\omega}}(k) & \left[I_{w,1}\bar{\Omega}_1 \frac{\partial a_1}{\partial p_1}\right]_k & \cdots & \left[I_{w,n}\bar{\Omega}_n \frac{\partial a_n}{\partial p_n}\right]_k \end{bmatrix} \left(\begin{bmatrix} h \\ \tilde{I} \\ P \end{bmatrix} - \begin{bmatrix} \bar{h}_k \\ \tilde{\bar{I}}_k \\ \bar{P}_k \end{bmatrix} \right)$$

$$+ \begin{bmatrix} -\left({}^k\bar{Q}^N \bar{h}_k\right)^x & \bar{I}_k & I_{w,1}\bar{a}_1(k) & \cdots & I_{w,n}\bar{a}_n(k) & 1_3 \end{bmatrix} \begin{bmatrix} \Delta\theta \\ \Delta\omega \\ \Delta\Omega \\ w_h \end{bmatrix} \quad (7.8)$$

$$\text{where } \bar{z}_h(k) = \bar{I}_k\bar{\omega}(k) - {}^k\bar{Q}^N\bar{h}_k + \sum I_{w,i}\bar{\Omega}_i(k)\,\bar{a}_i(k)$$

$$\text{and } \tilde{\bar{\omega}}(k) = \begin{bmatrix} \bar{\omega}_x(k) & 0 & 0 & \bar{\omega}_y(k) & \bar{\omega}_z(k) & 0 \\ 0 & \bar{\omega}_y(k) & 0 & \bar{\omega}_x(k) & 0 & \bar{\omega}_z(k) \\ 0 & 0 & \bar{\omega}_z(k) & 0 & \bar{\omega}_x(k) & \bar{\omega}_y(k) \end{bmatrix}$$

For the estimation schemes that do not include the actuator-alignment parameters in the estimated state, the relevant columns of the matrices in Eq. (7.8) are not included. The $w_h \sim \mathcal{N}\left(0, \sigma_{w_h}^2[1_3]\right)$ term is included as an optional additional source of noise in the angular momentum equation to help account for errors introduced by linearization.

The rotational kinetic energy of the spacecraft bus has a simple form depending only on the angular velocity of the spacecraft:

$$z_T(k) = 0 = T(k) - \frac{1}{2}\omega^T(k)\,I\omega(k) \quad (7.9)$$

The estimator states included in Eq. (7.9) enter linearly. Noise in the angular velocity knowledge and additional measurement noise can be incorporated by linearizing about the current inertia estimate and adding the term $w_T(k) \sim$

$\mathcal{N}\left(0, \sigma_{w_T}^2\right)$ as an optional source of additional measurement noise:

$$z_T(k) \approx T(k) - \frac{1}{2}\bar{\omega}^T(k) I \bar{\omega}(k) - \bar{\omega}^T(k) \bar{I}_k \Delta\omega(k) + w_T(k) \tag{7.10}$$

Equation 7.10 can similarly be reformatted to match the measurement Eq. (7.3):

$$0 = \begin{bmatrix} 1 & -\frac{1}{2}\hat{\bar{\omega}}(k) \end{bmatrix} \begin{bmatrix} T(k) \\ \tilde{I} \end{bmatrix} + \begin{bmatrix} -\bar{\omega}^T(k) \bar{I}_k & 1 \end{bmatrix} \begin{bmatrix} \Delta\omega \\ w_T \end{bmatrix} \tag{7.11}$$

where

$$\hat{\bar{\omega}}(k) = \begin{bmatrix} \bar{\omega}_1^2(k) & \bar{\omega}_2^2(k) & \bar{\omega}_3^2(k) & 2\bar{\omega}_1(k)\bar{\omega}_2(k) & 2\bar{\omega}_1(k)\bar{\omega}_3(k) & 2\bar{\omega}_2(k)\bar{\omega}_3(k) \end{bmatrix}$$

As the actuator-alignment parameters do not explicitly appear in Eq. (7.11), using this equation alone as the basis of an estimator is expected to produce poor estimates of momentum actuator axes.

7.3.2 Discrete-Time Dynamics

Several of the estimation state components are nominally constant parameters associated with the spacecraft attitude dynamics. Including the assumption that they are modified by artificial process noise in the estimator formulation helps prevent the estimates from converging too quickly and not incorporating subsequent measurements.[66,82] This inclusion has the added benefit of allowing these supposed constants to be slowly time-varying. In the case of the inertia and actuator-alignment parameters, this flexibility could help model unexpected variations in the spacecraft mass distribution or configuration. In the absence of external torques, the total angular momentum of the spacecraft expressed in inertial coordinates, h, is invariant over time. The addition of zero-mean, Gaussian artificial process noise to the angular momentum state dynamics, however, partially accounts for unmodeled external environmental

torques:

$$\begin{aligned}
\tilde{I}(k+1) &= \tilde{I}(k) + v_I(k) & v_I(k) &\sim \mathcal{N}\left(0, blkdiag\left(\sigma^2_{v_{IM}}[1_3], \sigma^2_{v_{IP}}[1_3]\right)\right) \\
P(k+1) &= P(k) + v_P(k) & v_P(k) &\sim \mathcal{N}\left(0, \sigma^2_{v_P}[1_{2n}]\right) \\
h(k+1) &= h(k) + v_h(k) & v_h(k) &\sim \mathcal{N}\left(0, \sigma^2_{v_h}[1_3]\right)
\end{aligned} \tag{7.12}$$

The rotational kinetic energy state evolves based on the inputs to the reaction wheels. Projecting Eq. (7.1) onto the body-rate vector, ω, describes the continuous-time dynamics of the rotational kinetic energy:

$$\dot{T}(k) = \omega^T(k)[I]\dot{\omega}(k) = -\omega^T(k)\sum I_{w,i}\dot{\Omega}_i a_i \tag{7.13}$$

Integrating between times t_k and t_{k+1} translates the continuous-time dynamics into a discrete-time form:

$$T(k+1) = T(k) - \int_{t_k}^{t_{k+1}} \omega^T\left(\sum I_{w,i}\dot{\Omega}_i a_i\right) dt \tag{7.14}$$

The integral in Eq. (7.14) requires continuous-time knowledge of ω and $\dot{\Omega}$. In practice, the attitude-dynamics states are known only at discrete times, and the reaction-wheel accelerations, $\dot{\Omega}$, need to be approximated from a known Ω time history, resulting in an approximation of the integral. The required fidelity of the particular integration scheme implemented depends largely on the sampling frequency of the available attitude-dynamics data. The selection of an integration method for this purpose is beyond the scope of this paper.

$$\int_{t_k}^{t_{k+1}} \omega^T\left(\sum I_{w,i}\dot{\Omega}_i a_i\right) dt \approx \mathcal{J}(\omega, \Omega, a_1, ..., a_n) \tag{7.15}$$

Linearizing Eq. (7.15) about the measured attitude-dynamics states, specifically $\bar{\omega}$ and $\bar{\Omega}$, allows for the appropriate incorporation of noise in the body-rate and reaction-wheel speed measurements into the discrete-time

dynamics equation. Additional zero-mean white process noise, $v_T \sim \mathcal{N}\left(0, \sigma_{v_T}^2\right)$, can be incorporated to help minimize the errors introduced with the integration approximation of Eq. (7.15):

$$T(k+1) \approx \bar{T}_k - \mathcal{J}\left(\bar{\omega}, \bar{\Omega}, \bar{a}_1(k), ...\bar{a}_n(k)\right) + \left[1 \quad -\left[\frac{\partial \mathcal{J}}{\partial P}\right]_k\right]\left(\begin{bmatrix} T(k) \\ P \end{bmatrix} - \begin{bmatrix} \bar{T}_k \\ \bar{P}_k \end{bmatrix}\right) + \left[-\left[\frac{\partial \mathcal{J}}{\partial \omega}\right]_k \quad -\left[\frac{\partial \mathcal{J}}{\partial \Omega}\right]_k \quad 1\right]\begin{bmatrix} \Delta\omega \\ \Delta\Omega \\ v_T \end{bmatrix} \tag{7.16}$$

The partial derivatives of $\mathcal{J}$ included in Eq. (7.16) are dependent on the numerical differentiation scheme utilized to produce $\dot{\Omega}$ and the numerical integration scheme used to approximate the integral of Eq. (7.15).

7.3.3 Estimator Observability

A discrete, linear, time-varying system is considered observable on the interval t_k to t_{k+m} if its observability Gramian is nonsingular.[83]

$$O = \sum_{j=k}^{k+m} \Phi\left(t_j, t_k\right)^T H_j^T H_j \Phi\left(t_j, t_k\right) \tag{7.17}$$

$$\Phi\left(t_j, t_k\right) = F_j F_{j-1} \cdots F_{k+1} F_k \tag{7.18}$$

In the context of a linearized estimator for a non-linear problem, such as an EKF, this criterion instead describes whether the state is locally observable near the true state trajectory. As described by Eq. (7.12), the inertia, momentum-actuator alignment parameters, and the angular momentum states are assumed to be constant in the absence of process noise. The rotational kinetic energy state, however, has discrete-time dynamics described by Eq. (7.14). While the linear rotational kinetic energy measurement Eq. (7.11) does not include

momentum-actuator alignment parameters, the F_k matrix produced by Eq. (7.14) does, indicating that these states could potentially influence the rank of the observability Gramian and cause the actuator-alignment parameters to be observable.

Estimator variants not including the rotational kinetic energy state effectively have the identity state transition matrix, and the observability Gramian corresponds to the matrix multiplication of the stacked linear measurement matrices. For the particular case of the momentum-based estimation of both inertia and actuator-alignment parameters, the stacked measurement matrices derived from Eq. (7.8) depend upon the direction cosine matrices defining the attitude, the angular velocity in body coordinates, and the terms associated with actuator-alignment parameters.

$$H_b = \begin{bmatrix} H_1 \\ H_2 \\ \vdots \\ H_m \end{bmatrix} = \begin{bmatrix} -^{k_1}Q^N & \tilde{\omega}_1 & \left[I_{w,1}\Omega_1 \frac{\partial a_1}{\partial p_1}\right]_1 & \cdots & \left[I_{w,n}\Omega_n \frac{\partial a_n}{\partial p_n}\right]_1 \\ -^{k_2}Q^N & \tilde{\omega}_2 & \left[I_{w,1}\Omega_1 \frac{\partial a_1}{\partial p_1}\right]_2 & \cdots & \left[I_{w,n}\Omega_n \frac{\partial a_n}{\partial p_n}\right]_2 \\ \vdots & \vdots & \vdots & & \vdots \\ -^{k_m}Q^N & \tilde{\omega}_m & \left[I_{w,1}\Omega_1 \frac{\partial a_1}{\partial p_1}\right]_m & \cdots & \left[I_{w,n}\Omega_n \frac{\partial a_n}{\partial p_n}\right]_m \end{bmatrix} \tag{7.19}$$

For a set of m measurements, we can then define the block matrices $\hat{Q}$, B, W, and J.

$$\hat{Q} = \begin{bmatrix} ^{k_1}Q^N \\ ^{k_2}Q^N \\ \vdots \\ ^{k_m}Q^N \end{bmatrix} \quad B = \begin{bmatrix} \tilde{\omega}_1 \\ \tilde{\omega}_2 \\ \vdots \\ \tilde{\omega}_m \end{bmatrix} \quad W = \begin{bmatrix} \left[I_{w,1}\Omega_1 \frac{\partial a_1}{\partial p_1}\right]_1 & \cdots & \left[I_{w,n}\Omega_n \frac{\partial a_n}{\partial p_n}\right]_1 \\ \left[I_{w,1}\Omega_1 \frac{\partial a_1}{\partial p_1}\right]_2 & \cdots & \left[I_{w,n}\Omega_n \frac{\partial a_n}{\partial p_n}\right]_2 \\ \vdots & & \vdots \\ \left[I_{w,1}\Omega_1 \frac{\partial a_1}{\partial p_1}\right]_m & \cdots & \left[I_{w,n}\Omega_n \frac{\partial a_n}{\partial p_n}\right]_m \end{bmatrix} \tag{7.20}$$

$$J = \left(1_{3m} - \hat{Q}\hat{Q}^T\right)$$

A few obvious necessary conditions for observability come from this block matrix representation. H_b must have more rows than columns, placing a lower bound on the number of measurements required. The matrices $\hat{Q}$, B, and W

must also individually have a rank equal to the number of columns in each block matrix, 3, 6, and $2n$ respectively. As each direction cosine matrix composing Q is guaranteed to have a rank of 3, the columns of $\hat{Q}$ are also known to be linearly independent. The definition of the $\tilde{\omega}_k$ matrix included in Eq. (7.8) suggests that at least two of submatrices composing B must be linearly independent, corresponding to a change in body rates around all three body axes. This requirement automatically rules attitude dynamics produced by an equilibrium spin as providing sufficiently rich data for full-state observability. The rank of W depends upon the expressions for $\left[I_{w,i}\Omega_i \frac{\partial a_i}{\partial p_i}\right]_k$, which in turn depend upon the current estimate of the momentum-actuator misalignment. Eq. (B.9) indicates that under the assumption of an accurate initial actuator-axis guess corresponding to $p_i = \begin{bmatrix}0 & 0\end{bmatrix}^T$, $[\partial a_i/\partial p_i]$ reduces to two constant and linearly independent columns of ${}^kQ^{gi}$. Under these assumptions, it is necessary (but not sufficient) to command a non-zero wheel speed for each of the momentum actuators at some point over the attitude dynamics trajectory.

Note that the matrix multiplication of $\hat{Q}^T\hat{Q} = m1_3$, as it represents the sum of each direction cosine matrix multiplying its inverse. Combining equations (7.17), (7.19), and (7.20) results in a representation of the observability Gramian in terms of block matrix multiplication.

$$O = H_b^T H_b = \begin{bmatrix} -\hat{Q}^T \\ B^T \\ W^T \end{bmatrix} \begin{bmatrix} -\hat{Q} & B & W \end{bmatrix} = \begin{bmatrix} m1_3 & -\hat{Q}^T B & -\hat{Q}^T W \\ -B^T\hat{Q} & B^T B & B^T W \\ -W^T\hat{Q} & W^T B & W^T W \end{bmatrix} \tag{7.21}$$

Assume the following three block lower triangular matrices L_1, L_2, and L_3 exist:

$$L_1 = \begin{bmatrix} \frac{1}{m}1_3 & 0 & 0 \\ \frac{1}{m}B^T\hat{Q} & 1_6 & 0 \\ \frac{1}{m}W^T\hat{Q} & 0 & 1_{2n} \end{bmatrix}$$

$$L_2 = \begin{bmatrix} 1_3 & 0 & 0 \\ 0 & \left(B^T J B\right)^{-1} & 0 \\ 0 & -WJB\left(B^T JB\right)^{-1} & 1_3 \end{bmatrix}$$

$$L_3 = \begin{bmatrix} 1_3 & 0 & 0 \\ 0 & 1_6 & 0 \\ 0 & 0 & \left(W^T JW - W^T JB\left(B^T JB\right)^{-1} B^T JW\right)^{-1} \end{bmatrix} \tag{7.22}$$

The product of these matrices with the observability Gramian from Eq. (7.21) produces a upper triangular matrix of full rank.

$$L_3 L_2 L_1 O = \begin{bmatrix} 1_3 & -\frac{1}{m}\hat{Q}^T B & -\frac{1}{m}\hat{Q}^T W \\ 0 & 1_6 & \left(B^T JB\right)^{-1} B^T JW \\ 0 & 0 & 1_{2n} \end{bmatrix} \tag{7.23}$$

Provided that the square, lower triangular matrices from Eq. (7.22) exist, the observability matrix is full rank and therefore nonsingular. The existence of L_2 and L_3 is contingent on two smaller matrices, S_1 and S_2, being invertible.

$$S_1^{-1} = \left(B^T JB\right)^{-1} \qquad S_2^{-1} = \left(W^T JW - W^T JB\left(B^T JB\right)^{-1} B^T JW\right)^{-1} \tag{7.24}$$

It can further be recognized that the inverses of S_1 and S_2 existing is equivalent to a particular block matrix inverse existing.

$$S^{-1} = \begin{bmatrix} W^T JW & W^T JB \\ B^T JW & B^T JB \end{bmatrix}^{-1} \tag{7.25}$$

We now have three sets of matrices, O, S, or S_1 and S_2 that could be examined to determine if the angular momentum, inertia, and actuator-alignment states are observable from the conservation of angular momentum equation for a given attitude dynamics trajectory defined by the block matrices $\hat{Q}$, B, and W.

7.4 Representative Algorithm Performance

Examination of the performance of the parameter estimators described by Table 7.1 over computer-generated attitude dynamics histories where the true parameter values are known provides a basis for comparison of the performance of the various schemes. These schemes were implemented as EKFs and utilized trapezoidal integration to approximate changes in the rotational kinetic energy state due to momentum-actuator inputs given by Eq. (7.15) where appropriate. For the simulated spacecraft maneuvers, three cases were considered that varied the initial guess of the assumed momentum-actuator axes and the ambient torque environment. The parameter estimators were also applied to four sets of telemetry data from the MESSENGER spacecraft gathered during calibration maneuvers as examples of algorithm performance with actual data.

7.4.1 Performance over Simulated Maneuvers

The computer-generated attitude dynamics were based on the assumption of a rigid spacecraft and inherently neglect momentum and energy contributions from sources potentially included in higher-fidelity models, such as flexible structural modes or fuel slosh. The simulated maneuver consisted of a sequence of commanded rotations about spacecraft body axes with interspersed rotations about linear combinations of two body axes. Momentum actuators consisted of four reaction wheels. Figure 7.1 plots the time histories of the computer-generated attitude, angular velocity, and wheel speed components in the absence of external torques for the first of the three cases. The attitude dynamics

were sampled at a frequency of 1 Hz. Pittelkau and O'Shaughnessy utilized a similar maneuver to estimate the gyro misalignment for the MESSENGER spacecraft.[84] The three simulated cases shared identical true physical properties

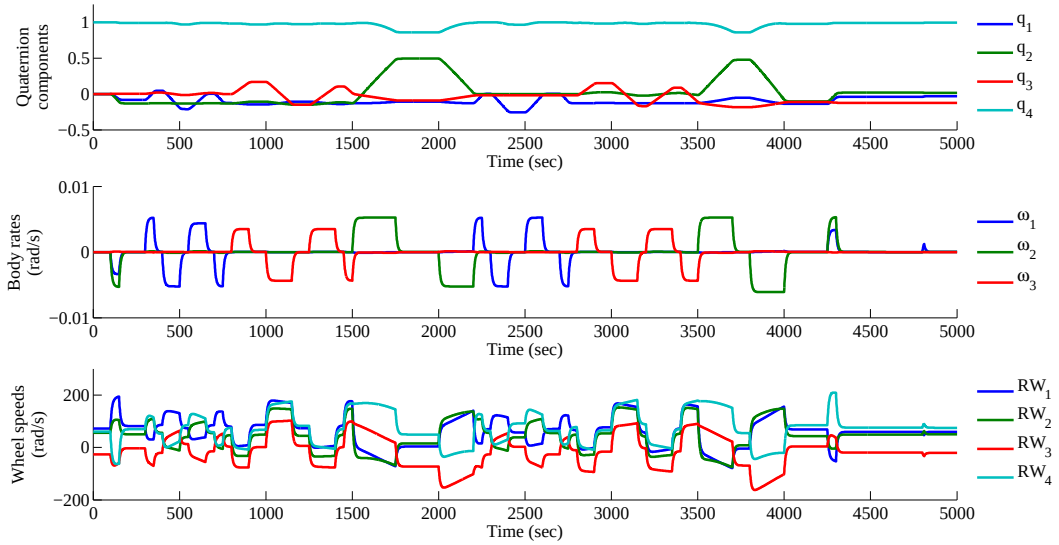

Figure 7.1: Computer-generated attitude-dynamics time histories for a sample maneuver.

as well as the same attitude dynamics noise statistics described by equations (7.6). These physical properties approximate those of the MESSENGER spacecraft on day 222 of 2009, the date of one of the maneuvers considered in section 7.4.2. The true inertia and momentum-actuator alignments do not change over the course of the simulations.

$$I_{true} = \begin{bmatrix} 308.5 & -0.1 & 0.0 \\ -0.1 & 402.1 & 4.5 \\ 0.0 & 4.5 & 508.8 \end{bmatrix} \text{kg m}^2 \quad I_w = \begin{bmatrix} 0.012172 \\ 0.012274 \\ 0.012115 \\ 0.012298 \end{bmatrix} \text{kg m}^2$$

$$a_{true} = \begin{bmatrix} 0.7379 & -0.7025 & 0.7429 & -0.7412 \\ 0.4719 & 0.5204 & -0.4790 & -0.5142 \\ 0.4825 & 0.4854 & 0.4675 & 0.4315 \end{bmatrix} \tag{7.26}$$

$$\sigma_{\theta,true} = 484\ \mu\text{rad} \quad \sigma_{\omega,true} = 1.00\ \text{nrad} \quad \sigma_{\Omega,true} = 1.00\ \text{nrad}$$

All parameter estimators across all of the simulated maneuver cases were initialized with identical state and covariance estimates.

$$\begin{gathered} \bar{T}_0 = 0.0\ \text{J} \quad cov\left(T_0\right) = 10\ \text{J}^2 \\ \bar{h}_0 = \begin{bmatrix} 0 & 0 & 0 \end{bmatrix}^T\ \text{N-m-s} \quad cov\left(\bar{h}_0\right) = 400\,[1_3]\ \text{(N-m-s)}^2 \\ \bar{\bar{I}}_0 = \begin{bmatrix} 0 & 0 & 0 & 0 & 0 & 0 \end{bmatrix}^T\ \text{kg-m}^2 \quad cov\left(\bar{\bar{I}}_0\right) = \begin{bmatrix} 250000\,[1_3] & 0 \\ 0 & 100\,[1_3] \end{bmatrix}\ (\text{kg-m}^2)^2 \\ \bar{P}_0 = \begin{bmatrix} 0 & 0 & 0 & 0 & 0 & 0 & 0 & 0 \end{bmatrix}^T\ \text{rad} \quad cov\left(P_0\right) = 0.0025\,[1_8]\ \text{rad}^2 \end{gathered} \tag{7.27}$$

The initial conditions in Eq. (7.27) correspond to a relatively confident initial guess of the momentum actuator axes but limited initial knowledge of the remaining estimator states. All cases and estimators also assumed identical process and measurement noise covariances.

$$\begin{array}{lll} \sigma_\theta = 484\ \mu\text{rad} & \sigma_\omega = 1.00\ \text{nrad} & \sigma_\Omega = 1.00\ \text{nrad} \\ \sigma_{v_P} = 1.00\ \mu\text{rad} & \sigma_{v_h} = 100\ \mu\text{N-m-s} & \sigma_{v_T} = 1.00\ \mu\text{J} \\ \sigma_{v_{IM}} = 1.00 \times 10^{-6}\ \text{kg-m}^2 & \sigma_{v_{IP}} = 1.00 \times 10^{-7}\ \text{kg-m}^2 & \\ \sigma_{w_h} = 0.01\ \text{N-m-s} & \sigma_{w_T} = 10.0\ \mu\text{J} & \end{array} \tag{7.28}$$

Case 1: True actuator axes, no external torques

The first case assumed that the initial guesses of the actuator axes, encapsulated in the constant direction cosine matrices ${}^kQ^{gi}$, accurately reflected the axes

utilized in the simulation and given in Eq. (7.26).

$$
{}^{k}Q^{g1} = \begin{bmatrix} 0.0416 & -0.6736 & 0.7379 \\ 0.6818 & 0.5590 & 0.4719 \\ -0.7303 & 0.4835 & 0.4825 \end{bmatrix} \quad {}^{k}Q^{g2} = \begin{bmatrix} -0.0191 & -0.7114 & -0.7025 \\ 0.6681 & -0.5318 & 0.5204 \\ -0.7439 & -0.4594 & 0.4854 \end{bmatrix}
$$

$$
{}^{k}Q^{g3} = \begin{bmatrix} -0.0297 & -0.6687 & 0.7429 \\ 0.6742 & -0.5622 & -0.4790 \\ 0.7380 & 0.4866 & 0.4675 \end{bmatrix} \quad {}^{k}Q^{g4} = \begin{bmatrix} -0.0078 & -0.6713 & -0.7412 \\ 0.6496 & 0.5602 & -0.5142 \\ 0.7604 & -0.4853 & 0.4315 \end{bmatrix} \tag{7.29}
$$

No external torques were applied to the rigid body spacecraft during the first simulation. Conceptually, the lack of external torques allows for the direct comparison of the momentum vector in inertial coordinates between two arbitrary times without needing to numerically integrate an input torque. Similarly, this simplification is equivalent to assuming that the only changes to the spacecraft rotational kinetic energy originate from the known momentum-actuator inputs.

The expectation was that this set of initial assumptions would represent the ideal case for all the variants of the parameter estimators, as no errors due to actuator misalignment would be introduced into the algorithms incapable of appropriately compensating for them. Figures 7.2 and 7.3 plot the magnitude of the error in the kinetic energy and angular momentum estimates across the parameter estimators described in Table 7.1 relative to the true angular momentum and rotational kinetic energy trajectories. All four parameter estimator variants including an angular momentum state produce accurate estimates of the spacecraft angular momentum. Examining the 3σ upper bounds on the error, however, separates the state trajectories into two groupings of nearly-identical confidences. The Variant 2 and 3 estimators did not include the momentum-actuator alignment parameter state and produced marginally

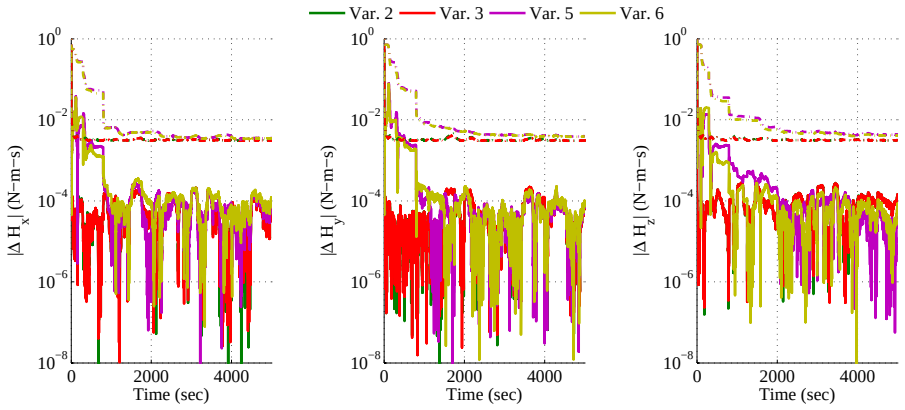

Figure 7.2: Magnitude of errors in angular momentum components for the first simulated maneuver case. 3σ upper bounds on the error are provided as dashed lines.

lower standard deviations than the Variant 5 and 6 estimators. The four

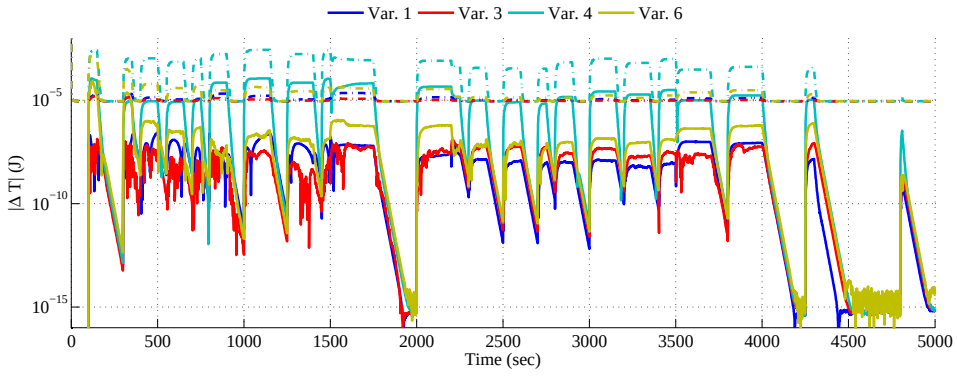

Figure 7.3: Magnitude of errors in the rotational kinetic energy state for the first simulated maneuver case. 3σ upper bounds on the error are provided as dashed lines.

parameter estimator variants including a rotational kinetic energy state were all capable of accurately recreating the true rotational kinetic energy of the rigid body. The 3σ bounds on the error differentiate the estimators, with Variant

3 producing the most accurate estimates and Variant 4 producing the least accurate.

Figures 7.4 and 7.5 describe the magnitude of the error in the inertia and momentum-actuator alignment parameters relative to their true values. Five of

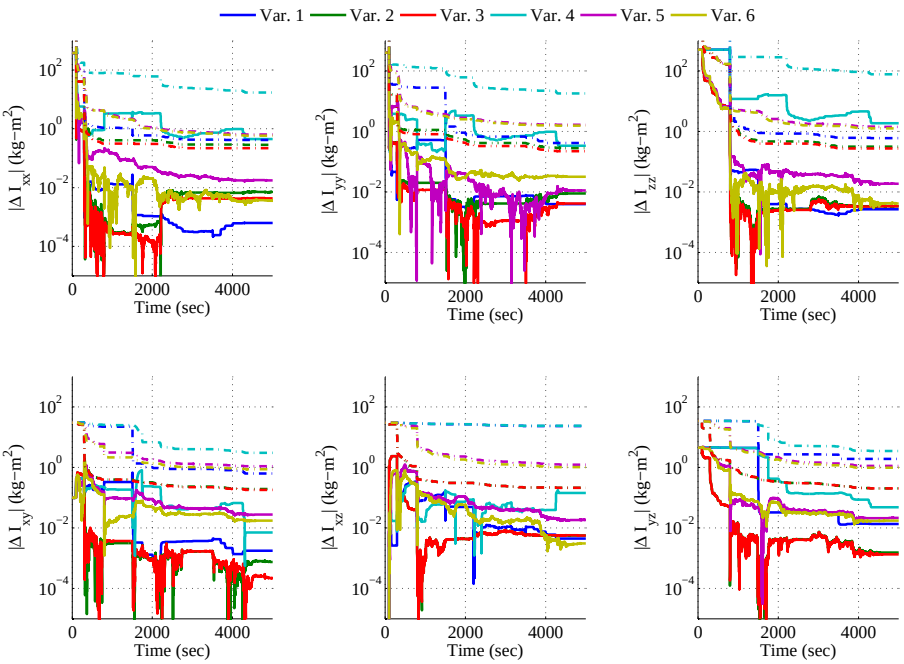

Figure 7.4: Magnitude of errors of the inertia parameter estimates for the first simulated maneuver case. 3σ upper bounds on the error are provided as dashed lines.

the six estimation schemes produced estimates of the moments and products of inertia accurate to under 1 kg-m^2. The Variant 4 estimator again produced significant errors in the estimated states and 3σ bounds for all of the inertia parameters. The low error in the actuator-alignment parameter states for the Variant 5 and 6 estimators indicate that they were capable of identifying that the actuator-alignment matrices from Eq. (7.29) reflected the true reaction wheel

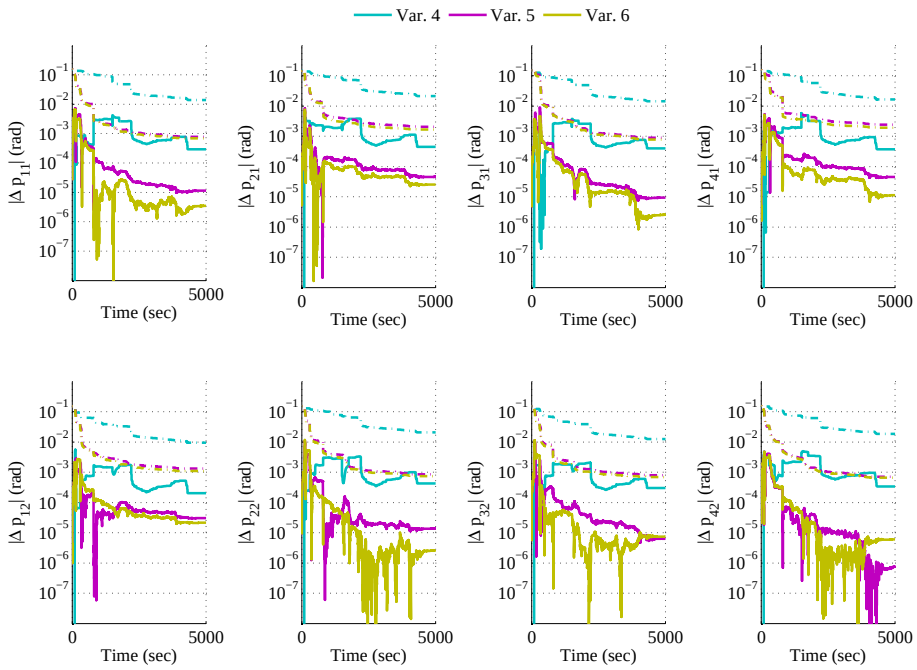

Figure 7.5: Magnitude of errors in the momentum-actuator alignment parameters for the first simulated maneuver case. 3σ upper bounds on the error are provided as dashed lines.

axis directions. The Variant 4 estimator produced significantly larger errors in its estimate of P.

Comparing the errors graphed in Figures 7.2, 7.3, 7.4, and 7.5 provides insight into the performance of the six estimator variants under the assumptions of no external torques and accurate knowledge of the momentum-actuator axes. Tables 7.2 and 7.3 list the final estimated inertia and actuator-alignment parameters for the six estimator variants under the assumptions of no external torques and accurate knowledge of the momentum-actuator axes.

Variant 3 combined both rotational kinetic energy and angular momentum measurement equations without including momentum-actuator alignment

Table 7.2: Final state inertia and momentum-actuator alignment parameter estimates of the Variant 1, 2, and 3 filters for the first simulated maneuver case. Standard deviations are included for each parameter in parenthesis.

		Truth	Var. 1	Var. 2	Var. 3
I_{xx}	(kg-m^2)	380.500	380.501(0.140)	380.507(0.093)	380.504(0.071)
I_{yy}		402.100	402.096(0.137)	402.109(0.091)	402.104(0.072)
I_{zz}		508.800	508.803(0.202)	508.803(0.104)	508.803(0.090)
I_{xy}		-0.100	-0.098(0.207)	-0.099(0.064)	-0.100(0.061)
I_{xz}		0.000	-0.004(7.723)	0.006(0.069)	0.006(0.069)
I_{yz}		4.500	4.486(0.632)	4.498(0.068)	4.499(0.067)

Table 7.3: Final state inertia and momentum-actuator alignment parameter estimates of the Variant 4, 5, and 6 filters for the first simulated maneuver case. Standard deviations are included for each parameter in parenthesis.

		Truth	Var. 1	Var. 2	Var. 3
I_{xx}	(kg-m^2)	380.500	380.946 (5.557)	380.518(0.209)	380.504(0.194)
I_{yy}		402.100	402.435 (5.837)	402.111(0.547)	402.132(0.502)
I_{zz}		508.800	506.921(25.352)	508.819(0.470)	508.804(0.419)
I_{xy}		-0.100	-0.107 (1.018)	-0.072(0.356)	-0.083(0.287)
I_{xz}		0.000	-0.144 (7.809)	-0.018(0.407)	-0.003(0.337)
I_{yz}		4.500	4.452 (1.146)	4.479(0.369)	4.482(0.317)
p_{11}	(mrad)	0.000	-0.289 (4.572)	-0.011(0.257)	-0.003(0.230)
p_{12}		0.000	-0.440 (6.887)	-0.046(0.675)	-0.025(0.550)
p_{21}		0.000	0.395 (4.630)	0.009(0.293)	0.003(0.260)
p_{22}		0.000	-0.373 (5.403)	0.045(0.794)	0.011(0.641)
p_{31}		0.000	-0.202 (3.065)	0.031(0.428)	0.021(0.356)
p_{32}		0.000	0.429 (6.752)	-0.014(0.277)	-0.003(0.248)
p_{41}		0.000	0.299 (4.006)	0.006(0.262)	-0.007(0.226)
p_{42}		0.000	0.340 (6.019)	0.001(0.237)	0.006(0.220)

states. This can be thought of as representing a combination of the Variant 1 and 2 estimators, both of which Variant 3 outperforms or matches the error across all estimated states. This suggests that combining both measurement equations results in slightly higher fidelity state estimates. In general, Variants 1, 2, and 3 produced lower state errors than Variants 4, 5, and 6, suggesting that inclusion of the momentum-actuator alignment states slightly degrades the inertia parameter estimates when the guessed actuator axes are known accurately *a priori*.

Case 2: False actuator axes, no external torques

The second case differs from the first by introducing an error in the guessed actuator axes.

$$
{}^{k}Q^{g1} = \begin{bmatrix} 0.000 & -0.6614 & 0.7500 \\ 0.6547 & 0.5669 & 0.5000 \\ -0.7559 & 0.4910 & 0.4330 \end{bmatrix} \quad {}^{k}Q^{g2} = \begin{bmatrix} 0.000 & -0.6614 & -0.7500 \\ 0.6547 & -0.5669 & 0.5000 \\ -0.7559 & -0.4910 & 0.4330 \end{bmatrix} \tag{7.30}
$$

$$
{}^{k}Q^{g3} = \begin{bmatrix} 0.000 & -0.6614 & 0.7500 \\ 0.6547 & -0.5669 & -0.5000 \\ 0.7559 & 0.4910 & 0.4330 \end{bmatrix} \quad {}^{k}Q^{g4} = \begin{bmatrix} 0.000 & -0.6614 & -0.7500 \\ 0.6547 & 0.5669 & -0.5000 \\ 0.7559 & -0.4910 & 0.4330 \end{bmatrix}
$$

The expectation was that this error would result in poor inertia parameter estimates for the filter variants that did not include the actuator-alignment parameters as estimator states. The error in the initial actuator-axis estimates correspond to angular offsets of 3.3355°, 4.2198°, 2.3492°, and 0.9645° from their true directions. The maneuver itself is otherwise identical to that of the first case.

Figures 7.6 and 7.7 plot the magnitude of the error in the kinetic energy and angular momentum estimates across the parameter estimators described in

Table 7.1 relative to the true angular momentum and rotational kinetic energy trajectories. Without the inclusion of the actuator alignment states, the Variant

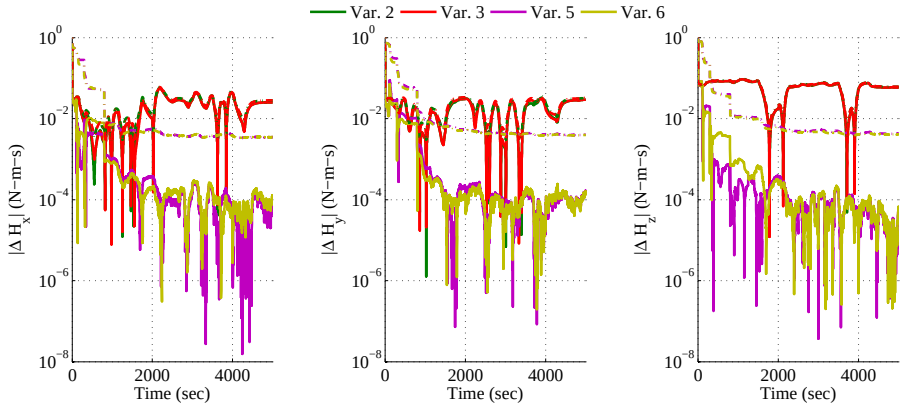

Figure 7.6: Magnitude of errors in angular momentum components for the second simulated maneuver case. 3σ upper bounds on the error are provided as dashed lines.

2 and 3 result in an angular momentum estimate approximately two orders of magnitude greater than the Variant 5 and 6 errors. With respect to the rotational

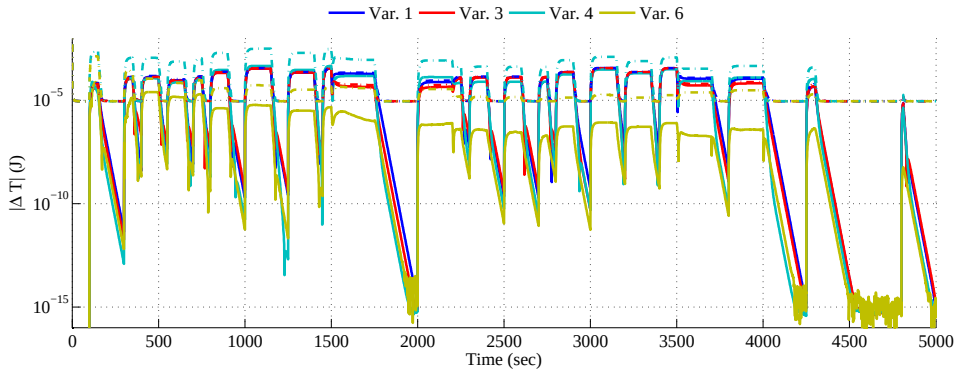

Figure 7.7: Magnitude of errors in the rotational kinetic energy state for the second simulated maneuver case. 3σ upper bounds on the error are provided as dashed lines.

kinetic energy state, the Variant 6 estimator produces significantly lower error than the other variants including the rotational kinetic energy state.

Figures 7.8 and 7.9, respectively, compare the magnitude of the inertia and alignment-parameter errors across the implemented estimation schemes. As

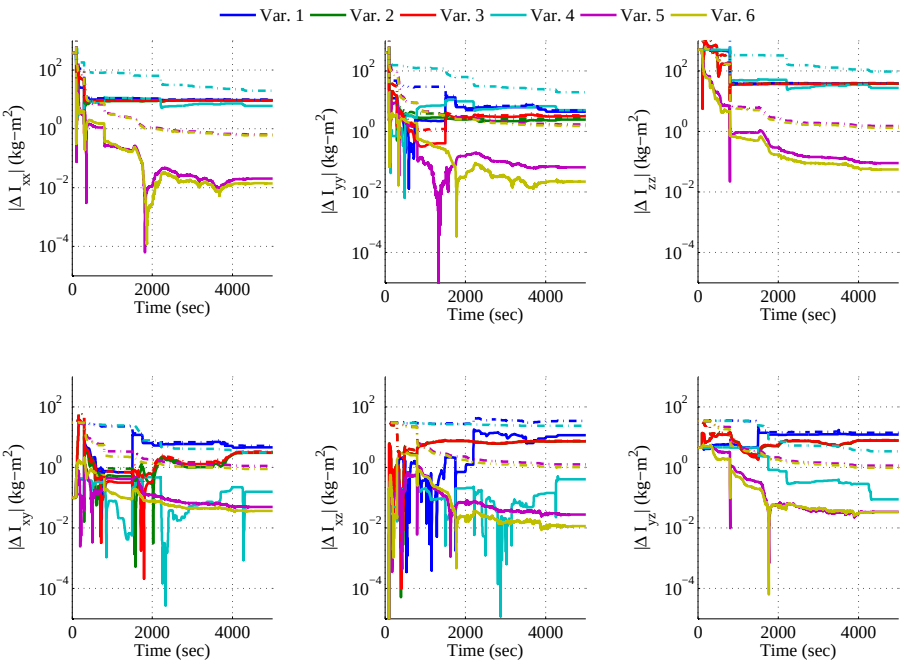

Figure 7.8: Magnitude of errors of the inertia parameter estimates for the second simulated maneuver case. 3σ upper bounds on the error are provided as dashed lines.

expected, Fig. 7.8 demonstrates the error in the inertia parameter estimates introduced by inaccurate initial actuator axis knowledge. These errors appear in the state estimates produced by the Variant 1, 2, and 3 estimation schemes. The Variant 4 estimator also produced comparatively poor inertia estimates. The Variant 5 and 6 estimators performed nearly equivalently, reducing the inertia parameter error to a level comparable to that seen in Figure 7.4. Variant 5 and

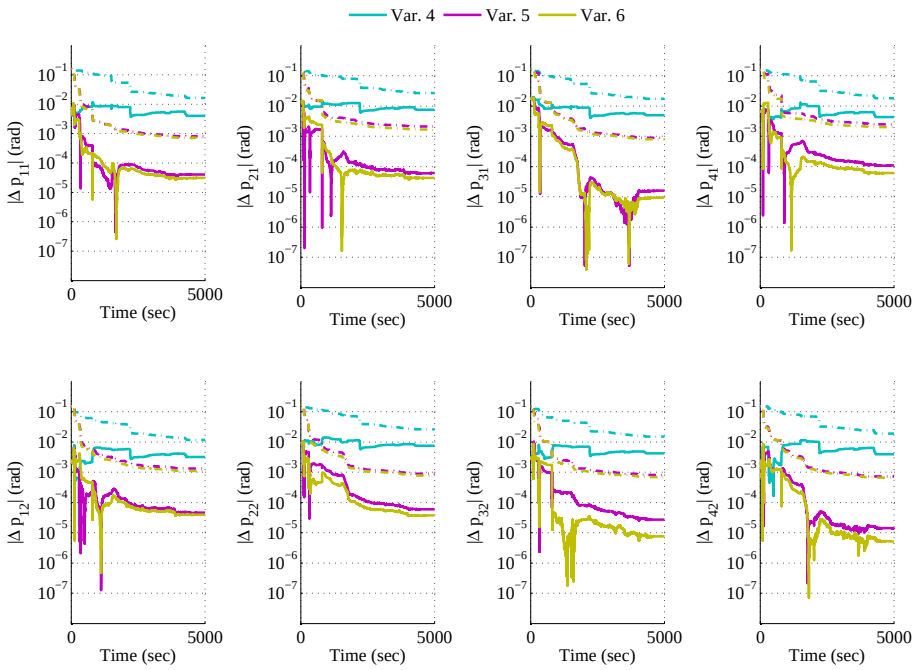

Figure 7.9: Magnitude of errors in the momentum actuator alignment parameters for the second simulated maneuver case. 3σ upper bounds on the error are provided as dashed lines.

6 both accurately reproduced the actuator misalignment. Variant 4 produced actuator-alignment estimates with several orders of magnitude greater error than than of Variant 5 or 6.

Tables 7.4 and 7.5 describe the final inertia and actuator alignment state and standard deviation estimates. Not including the actuator alignment parameters in the state estimate resulted in an erroneous terminal inertia matrix estimates and inappropriate filter-produced state standard deviations, indicating estimator inconsistency. While the Variant 5 and 6 estimators produced more accurate state estimates than those of Variant 4, all three of these variants produced state estimate errors of an appropriate magnitude in

Table 7.4: Final state inertia and momentum actuator alignment parameter estimates of the 1, 2, and 3 filters for the second simulated maneuver case. Standard deviations are included for each parameter in parenthesis.

		Truth	Var. 1	Var. 2	Var. 3
I_{xx}		380.500	389.972(0.140)	389.669(0.093)	389.753(0.071)
I_{yy}		402.100	406.625(0.137)	404.581(0.091)	405.259(0.072)
I_{zz}	(kg-m^2)	508.800	469.956(0.202)	471.293(0.104)	470.784(0.090)
I_{xy}		-0.100	-4.673(0.207)	-3.164(0.064)	-3.240(0.061)
I_{xz}		0.000	-11.553(7.723)	-7.292(0.069)	-7.289(0.069)
I_{yz}		4.500	-7.640(0.632)	-3.227(0.068)	-3.307(0.067)

Table 7.5: Final state inertia and momentum actuator alignment parameter estimates of the Variant 4, 5, and 6 filters for the second simulated maneuver case. Standard deviations are included for each parameter in parenthesis.

		Truth	Var. 4	Var. 5	Var. 6
I_{xx}		380.500	386.458 (4.672)	380.520(0.209)	380.514(0.194)
I_{yy}		402.100	407.199 (4.918)	402.035(0.547)	402.078(0.503)
I_{zz}	(kg-m^2)	508.800	481.416(22.777)	508.889(0.473)	508.855(0.423)
I_{xy}		-0.100	-0.257 (0.992)	-0.050(0.356)	-0.064(0.286)
I_{xz}		0.000	-0.402 (7.807)	-0.028(0.408)	-0.012(0.337)
I_{yz}		4.500	4.413 (1.105)	4.466(0.368)	4.466(0.316)
p_{11}		4.095	0.106 (4.099)	4.054(0.255)	4.064(0.229)
p_{12}		13.967	6.394 (6.323)	13.907(0.674)	13.925(0.547)
p_{21}		-17.204	-12.308 (4.131)	-17.188(0.293)	-17.195(0.260)
p_{22}	(mrad)	6.567	2.269 (4.552)	6.674(0.794)	6.627(0.641)
p_{31}		2.428	-0.732 (2.860)	2.474(0.428)	2.467(0.354)
p_{32}		-9.959	-2.425 (6.186)	-10.019(0.277)	-9.996(0.249)
p_{41}		-3.302	0.903 (3.560)	-3.275(0.262)	-3.294(0.227)
p_{42}		2.609	6.564 (5.019)	2.595(0.237)	2.604(0.220)

comparison with the filter covariance.

Case 3: True actuator axes, external torque

The third case differs from the first two by applying a disturbance torque to the simulated spacecraft taking the form of zero-mean white noise.

$$\sum M \sim \mathcal{N}\left(0, \sigma_M^2 \left[1_3\right]\right) \qquad \sigma_M = 1.0 \times 10^{-4} \text{ N-m} \tag{7.31}$$

The initial conditions given to the filters is otherwise identical to that of first case, providing the estimation algorithms with accurate momentum actuator axes from Eq. (7.29). The simulated maneuver itself commands the same spacecraft body rates as the first two cases and has the momentum actuators account for the additional angular momentum accumulated due to the external torque. More complicated and realistic models accounting for gravity gradient, solar, and other torques could be incorporated through the state dynamics function in Eq. (7.3). Tanygin and Williams and later Peck addressed the incorporation of general external torques to energy- and angular momentum-based inertia estimation methods, respectively.[70,74] For the purposes of this paper, a simple external torque model provides an acceptable basis for comparison between the filter variants when the angular momentum vector has state dynamics.

Figures 7.10 and 7.11 describe the errors encountered in the angular momentum and rotational kinetic energy quantities for the filter variants including those states. Qualitatively, the angular momentum state error in Figure 7.10 is similar to that seen in Figure 7.2. Again, a distinction is made between the variants including the momentum-actuator alignment states and

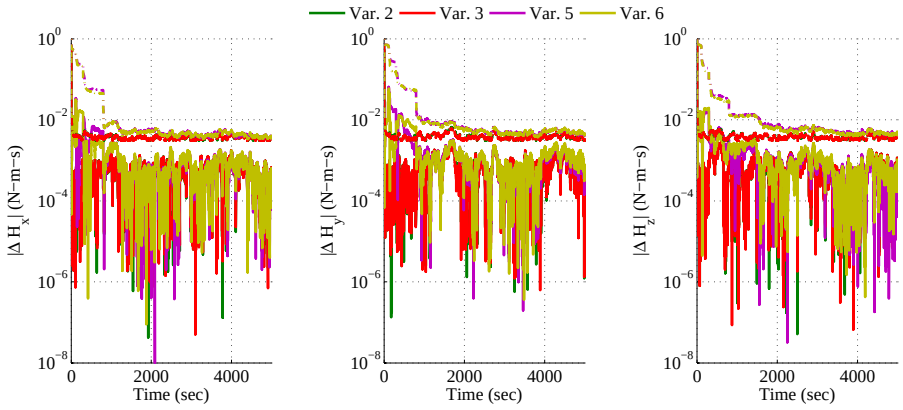

Figure 7.10: Magnitude of errors in angular momentum components for the third simulated maneuver case. 3σ upper bounds on the error are provided as dashed lines.

those that do not account for this source of error. Variants 5 and 6 produced slightly greater uncertainties associated with the angular momentum states and took slightly longer to converge. The error in the rotational kinetic energy states

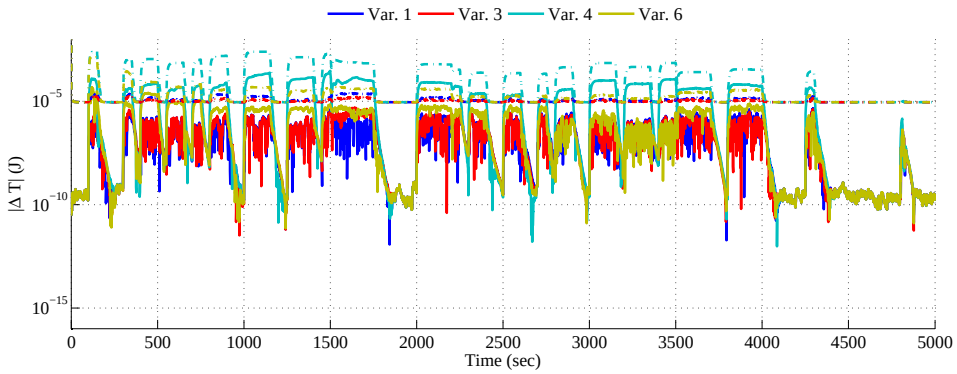

Figure 7.11: Magnitude of errors in the rotational kinetic energy state for the third simulated maneuver case. 3σ upper bounds on the error are provided as dashed lines.

increased for all filter variants after the introduction of the external torque.

Figures 7.12 and 7.13 plot the magnitude of the error encountered in the inertia and momentum actuator alignment parameter states. Similar to the first

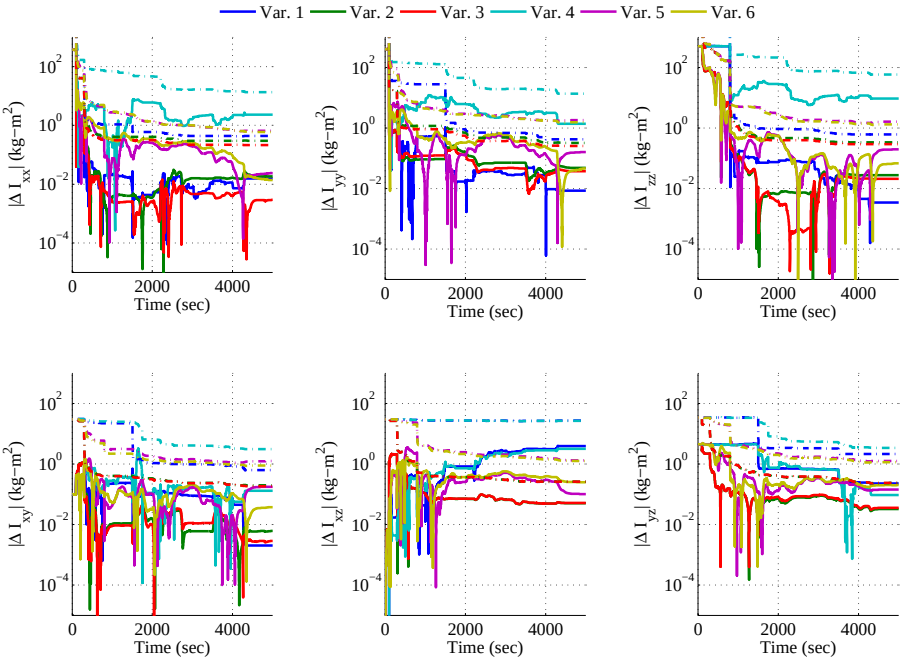

Figure 7.12: Magnitude of errors of the inertia parameter estimates for the third simulated maneuver case. 3σ upper bounds on the error are provided as dashed lines.

case, all estimator variants produced accurate inertia and actuator alignment parameter estimates, while Variant 4 developed significant errors.

Tables 7.6 and 7.7 describe the final state error and standard deviations of the inertia and momentum actuator alignment parameters. When compared with Tables 7.2 and 7.3, the final state error increased across all filter variants, with the most substantial changes occurring in the Variant 4 final states. Combining both measurement equations in Variants 3 and 6 produced slightly better final state estimates than just using the angular momentum measurement, as was the

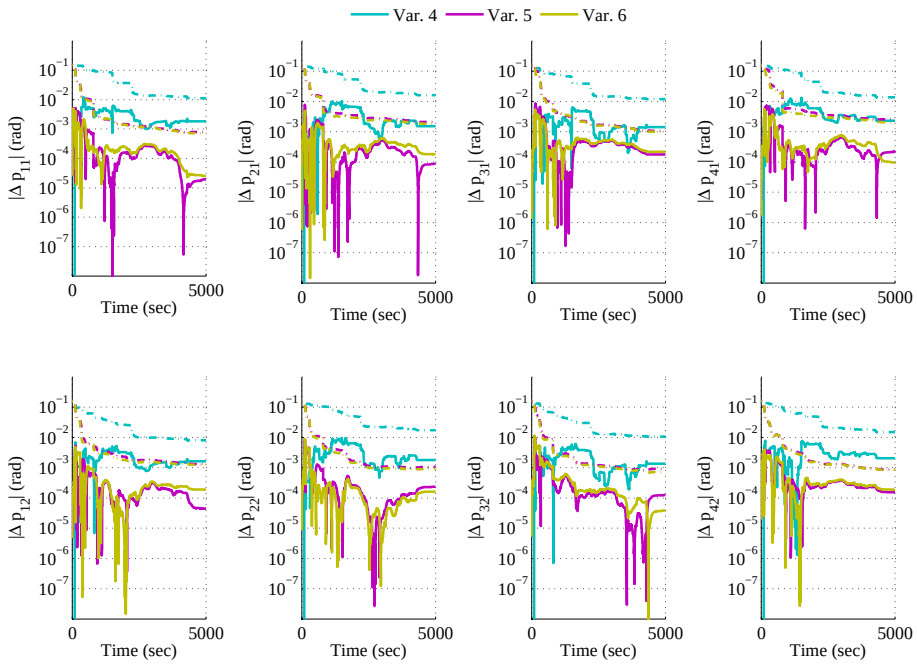

Figure 7.13: Magnitude of errors in the momentum actuator alignment parameters for the second simulated maneuver case. 3σ upper bounds on the error are provided as dashed lines.

Table 7.6: Final state inertia and momentum actuator alignment parameter estimates of the Variant 1, 2, and 3 filters for the third simulated maneuver case. Standard deviations are included for each parameter in parenthesis.

	Truth	Var. 4	Var. 5	Var. 6
I_{xx}	380.500	380.516(0.140)	380.518(0.093)	380.497(0.071)
I_{yy}	402.100	402.092(0.138)	402.052(0.091)	402.063(0.072)
I_{zz}	508.800	508.797(0.202)	508.828(0.104)	508.821(0.090)
I_{xy} (kg-m^2)	-0.100	-0.102(0.208)	-0.094(0.064)	-0.097(0.061)
I_{xz}	0.000	3.945(7.715)	0.051(0.069)	0.051(0.069)
I_{yz}	4.500	4.274(0.633)	4.467(0.068)	4.464(0.067)

Table 7.7: Final state inertia and momentum actuator alignment parameter estimates of the Variant 4, 5, and 6 filters for the third simulated maneuver case. Standard deviations are included for each parameter in parenthesis.

		Truth	Var. 4	Var. 5	Var. 6
I_{xx}	(kg-m^2)	380.500	382.816 (3.709)	380.524(0.210)	380.486(0.195)
I_{yy}		402.100	403.478 (4.119)	401.938(0.550)	402.054(0.502)
I_{zz}		508.800	499.405(16.309)	508.999(0.474)	508.869(0.421)
I_{xy}		-0.100	-0.231 (0.999)	0.078(0.357)	-0.063(0.287)
I_{xz}		0.000	3.200 (7.801)	0.101(0.410)	0.251(0.341)
I_{yz}		4.500	4.406 (1.112)	4.642(0.369)	4.700(0.318)
p_{11}	(mrad)	0.000	-1.815 (3.155)	-0.019(0.258)	0.025(0.231)
p_{12}		0.000	-1.510 (4.858)	-0.086(0.676)	0.179(0.553)
p_{21}		0.000	1.419 (3.515)	-0.176(0.295)	-0.216(0.262)
p_{22}		0.000	-2.326 (3.800)	0.215(0.799)	-0.096(0.645)
p_{31}		0.000	-1.636 (2.108)	-0.044(0.427)	-0.188(0.356)
p_{32}		0.000	1.763 (5.156)	-0.231(0.277)	-0.162(0.248)
p_{41}		0.000	1.340 (3.073)	0.123(0.265)	0.038(0.228)
p_{42}		0.000	2.047 (4.343)	0.153(0.239)	0.187(0.221)

case for Variants 2 and 5, and significantly better state estimates than just using the rotational kinetic energy, as was the case for Variants 1 and 4.

These three simulated maneuvers highlight both strengths and weaknesses of the six estimator variants. Variant 1, roughly corresponding to a recursive formulation of Tanygin and Williams' batch inertia parameter estimator, performed well when the momentum actuator axes were accurately known.[70] Variant 2 also performed well in the first case, and combining both rotational kinetic energy and angular momentum measurements in Variant 3 resulted in a slight improvement in the final estimated state. These first three variants,

however, all failed to provide consistent estimates in the second case, where the guesses of the actuator axes were incorrect. As these estimator variants did not include states designed to account for this type of error, the inertia parameter estimates diverged from their true values. The first three variants again produced reasonable estimates of I when the axes were correctly known and in the presence of an external torque.

The Variant 4 estimator deserves special attention, as it performed comparatively poorly in all three cases. The consistently large error in the estimates of T_k, I and P suggests that the single scalar rotational kinetic energy measurement in combination with the chosen trapezoidal integration scheme results in poor observability of the estimated state. It should be noted, however, that while the magnitude of the state error was large in all cases, Variant 4 also produced appropriate standard deviations for its states, indicating that at least the uncertainty in the estimate could be recognized by the user. This is particularly important in the context of the second case, where the user unknowingly supplies incorrect actuator axes to the parameter estimator. Variants 1, 2, and 3 were falsely confident in their incorrect estimated inertia parameters, while Variant 4 maintained a large uncertainty consistent with its large state error.

The Variant 5 and 6 estimators corresponded to implementations of the Variant 2 and 3 estimators with the inclusion of the P states representing momentum actuator alignment parameters. While these additional states slightly degraded performance when examining the results of Tables 7.2, 7.3, 7.6, and 7.7, estimator Variant 5 and 6 were the only filters to produce accurate estimates of I and P with an incorrect initial guess of the actuator axes. In each

of the three cases, both variants produced approximately the same magnitude of state error as each other.

7.4.2 Performance with MESSENGER Data

The MESSENGER spacecraft launched on August 3, 2004, and entered Mercury orbit in March 2011. Flight operations to date have included several attitude maneuvers designed to improve star tracker and gyro alignment knowledge.[84] Figure 7.14 plots the relevant attitude dynamics variables over one of the four similar maneuvers considered. At each of the four maneuvers, an estimate

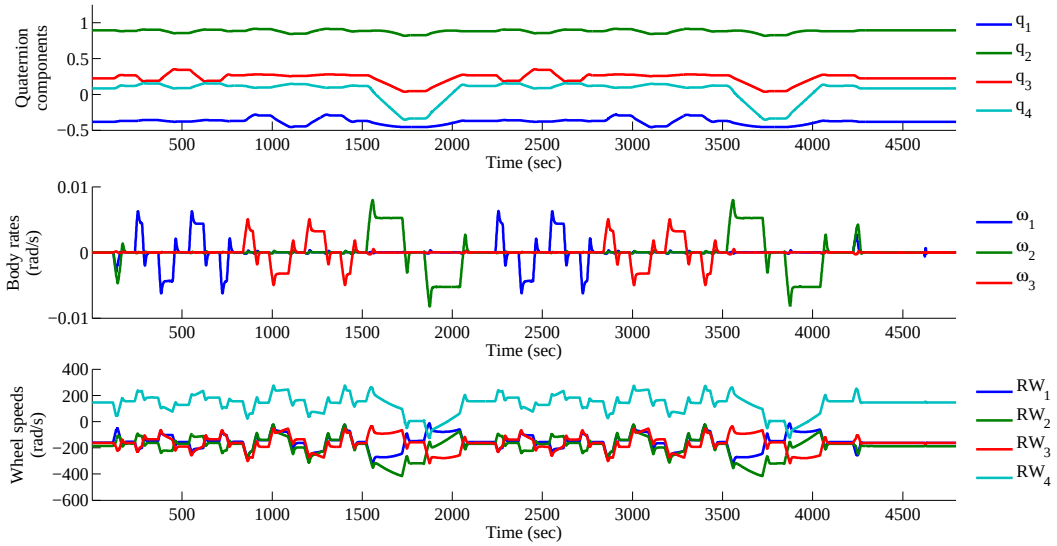

Figure 7.14: Attitude telemetry data from the MESSENGER calibration maneuver that occurred on day 262 of 2007.

of the inertia parameters of the spacecraft can be constructed from pre-launch knowledge of the mechanical properties and expected location of individual

rigid components and fuel. The presumed mechanical alignment of the reaction wheels is also available and is described by the third columns of the rotation matrices in Eq. (7.30). The filter configurations described by Table 7.1 used the telemetry data generated by these maneuvers sampled at 1 Hz to form estimates of the inertia parameters and momentum-actuator axes.

The guessed actuator alignments of Eq. (7.30) correspond to the presumed orientation of MESSENGER's reaction wheels relative to body coordinates. Each of the estimator variants on each of the maneuver data sets was initialized with the same conditions, which differed slightly from those of the simulated cases.

$$\begin{gathered}
\bar{T}_0 = 0.0 \text{ J} \quad cov(T_0) = 10 \text{ J}^2 \\
\bar{h}_0 = \begin{bmatrix} 0 & 0 & 0 \end{bmatrix}^T \text{ N-m-s} \quad cov\left(\bar{h}_0\right) = 400\,[1_3] \text{ (N-m-s)}^2 \\
\bar{\bar{I}}_0 = \begin{bmatrix} 0 & 0 & 0 & 0 & 0 & 0 \end{bmatrix}^T \text{ kg-m}^2 \quad cov\left(\bar{\bar{I}}_0\right) = \begin{bmatrix} 640000\,[1_3] & 0 \\ 0 & 100\,[1_3] \end{bmatrix} \text{ (kg-m}^2\text{)}^2 \\
\bar{P}_0 = \begin{bmatrix} 0 & 0 & 0 & 0 & 0 & 0 & 0 & 0 \end{bmatrix}^T \text{ rad} \quad cov(P_0) = 1.0 \times 10^{-12}\,[1_8] \text{ rad}^2
\end{gathered} \tag{7.32}$$

These initial conditions reflect high uncertainty in the moments of inertia and confidence in the initial guess of the momentum actuator axes. The process and measurement noises assumed by filters also differed slightly from the simulated data sets.

$$\begin{gathered}
\sigma_\theta = 484\ \mu\text{rad} \qquad \sigma_\omega = 1.00 \text{ nrad} \qquad \sigma_\Omega = 1.00 \text{ nrad} \\
\sigma_{v_P} = 1.00\ \mu\text{rad} \qquad \sigma_{v_h} = 0.10\ \mu\text{N-m-s} \qquad \sigma_{v_T} = 0.10 \text{ mJ} \\
\sigma_{v_{IM}} = 1.00 \times 10^{-6} \text{ kg-m}^2 \qquad \sigma_{v_{IP}} = 1.00 \times 10^{-7} \text{ kg-m}^2 \\
\sigma_{w_h} = 0.01 \text{ N-m-s} \qquad \sigma_{w_T} = 1.00 \text{ mJ}
\end{gathered} \tag{7.33}$$

The process noise associated with the angular momentum state was decreased, corresponding to an assumption of a lower magnitude ambient torque

environment. Additionally, the standard deviation of the process and measurement noises associated with the rotational kinetic energy state were increased to accommodate additional uncertainty introduced by the trapezoidal integration scheme propagating that state's discrete-time dynamics.

The trajectories of the estimated inertia and actuator alignment parameter states were qualitatively similar across all three maneuvers, so only those for the 2007 Day 262 maneuver are included in Figures 7.15 and 7.16. These figures plot the magnitude of the difference between the filter-produced state estimates and the inertia estimates assumed by looking at the expected mechanical configuration of the spacecraft. Unlike the simulated cases in section 7.4.1, this magnitude difference cannot be assumed to be the true error in each of the states, as the mechanical estimate itself in an assumed quantity not necessarily accurately reflecting the truth. The individual state difference trajectories are difficult to visually resolve in Figure 7.15 because the performance of several of the variants are effectively identical to each other. Variants 1 and 4 produced nearly identical trajectories, as did the pairs of Variants 2 and 3 and Variants 5 and 6. Similarly, the Variant 5 and 6 trajectories in Figure 7.16 are nearly indistinguishable.

Tables 7.8, 7.9, 7.10, 7.11, 7.12, 7.13, 7.14, and 7.15 describe the final state estimates of the inertia and actuator-axis parameters along with their filter-produced standard deviations.

Estimator variants including the angular momentum state produced inertia parameter estimates reasonably consistent with each other and with the mechanical team's estimates. The Variant 1 and 4 estimators, however, produced significantly different inertia parameter estimates and larger standard

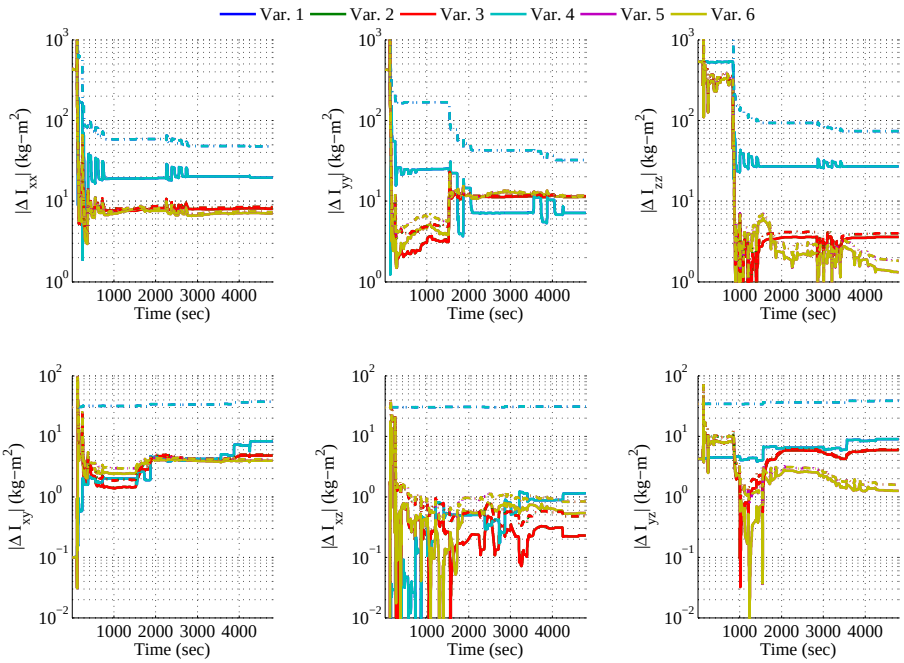

Figure 7.15: Magnitude of difference between the mechanical estimate and the filter-produced estimates of the inertia parameter states for the MESSENGER calibration maneuver that occurred on day 262 of 2007. 3σ upper bounds on the error are provided as dashed lines.

Table 7.8: Inertia parameter estimates produced by filter Variants 1, 2, and 3 from MESSENGER data on day 262 of 2007. Filter-produced standard deviations are provided for each parameter in parenthesis.

	Mech. Est.	Var. 1	Var. 2	Var. 3
I_{xx}	429.0	409.403 (9.322)	437.082(0.107)	437.079(0.107)
I_{yy}	427.2	420.071 (8.380)	438.479(0.075)	438.478(0.075)
I_{zz}	537.6	510.771(15.625)	534.007(0.132)	534.006(0.132)
I_{xy} (kg-m^2)	-0.10	8.189 (9.584)	-4.882(0.063)	-4.882(0.063)
I_{xz}	0.00	-1.136 (9.966)	-0.228(0.084)	-0.228(0.084)
I_{yz}	4.2	-4.730 (9.886)	10.087(0.063)	10.087(0.063)

Table 7.9: Inertia and actuator alignment parameter estimates produced by filter Variants 4, 5, and 6 from MESSENGER data on day 262 of 2007. Filter-produced standard deviations are provided for each parameter in parenthesis.

		Mech. Est.	Var. 4	Var. 5	Var. 6
I_{xx}	(kg-m^2)	429.0	409.404 (9.322)	436.001(0.117)	435.997(0.117)
I_{yy}		427.2	420.070 (8.382)	438.516(0.144)	438.513(0.144)
I_{zz}		537.6	510.772(15.626)	536.284(0.168)	536.283(0.168)
I_{xy}		-0.10	8.188 (9.584)	-4.057(0.079)	-4.055(0.079)
I_{xz}		0.00	-1.136 (9.966)	-0.541(0.099)	-0.541(0.099)
I_{yz}		4.2	-4.730 (9.886)	5.453(0.109)	5.452(0.109)
p_{11}	(mrad)	0.000	-0.001 (0.122)	-1.079(0.082)	-1.080(0.082)
p_{12}		0.000	0.000 (0.122)	-1.637(0.095)	-1.637(0.095)
p_{21}		0.000	-0.002 (0.122)	0.389(0.059)	0.389(0.059)
p_{22}		0.000	-0.004 (0.122)	-2.596(0.078)	-2.597(0.078)
p_{31}		0.000	0.003 (0.122)	3.226(0.078)	3.227(0.078)
p_{32}		0.000	-0.002 (0.122)	-1.164(0.079)	-1.165(0.079)
p_{41}		0.000	0.006 (0.122)	-0.213(0.081)	-0.212(0.081)
p_{42}		0.000	-0.005 (0.122)	-3.510(0.069)	-3.511(0.069)

Table 7.10: Inertia parameter estimates produced by filter Variants 1, 2, and 3 from MESSENGER data on day 182 of 2008. Filter-produced standard deviations are provided for each parameter in parenthesis.

		Mech. Est.	Var. 1	Var. 2	Var. 3
I_{xx}	(kg-m^2)	399.5	369.471 (8.306)	405.878(0.093)	405.874(0.093)
I_{yy}		404.8	409.153 (8.430)	430.383(0.064)	430.382(0.064)
I_{zz}		527.9	488.010(14.695)	510.953(0.111)	510.952(0.111)
I_{xy}		-0.10	1.868 (9.252)	-3.263(0.053)	-3.263(0.053)
I_{xz}		0.00	-0.525 (9.969)	0.298(0.071)	0.298(0.071)
I_{yz}		4.50	-0.993 (9.983)	8.664(0.056)	8.664(0.056)

Table 7.11: Inertia and actuator alignment parameter estimates produced by filter Variants 4, 5, and 6 from MESSENGER data on day 182 of 2008. Filter-produced standard deviations are provided for each parameter in parenthesis.

		Mech. Est.	Var. 4	Var. 5	Var. 6
I_{xx}	(kg-m^2)	399.5	369.470 (8.306)	406.635(0.116)	406.629(0.116)
I_{yy}		404.8	409.151 (8.431)	430.458(0.171)	430.456(0.171)
I_{zz}		527.9	488.017(14.697)	507.180(0.232)	507.186(0.232)
I_{xy}		-0.10	1.868 (9.252)	-4.253(0.064)	-4.253(0.064)
I_{xz}		0.00	-0.525 (9.969)	0.144(0.088)	0.144(0.088)
I_{yz}		4.50	-0.993 (9.983)	6.207(0.100)	6.207(0.100)
p_{11}	(mrad)	0.000	0.001 (0.122)	-1.680(0.097)	-1.679(0.097)
p_{12}		0.000	0.001 (0.122)	-1.629(0.099)	-1.627(0.099)
p_{21}		0.000	-0.000 (0.122)	2.205(0.087)	2.204(0.087)
p_{22}		0.000	0.001 (0.122)	-1.779(0.087)	-1.778(0.087)
p_{31}		0.000	0.001 (0.122)	-0.722(0.079)	-0.722(0.079)
p_{32}		0.000	-0.002 (0.122)	0.789(0.084)	0.788(0.084)
p_{41}		0.000	-0.001 (0.122)	-2.289(0.079)	-2.290(0.079)
p_{42}		0.000	-0.003 (0.122)	-1.734(0.085)	-1.736(0.085)

Table 7.12: Inertia parameter estimates produced by filter Variants 1, 2, and 3 from MESSENGER data on day 184 of 2008. Filter-produced standard deviations are provided for each parameter in parenthesis.

		Mech. Est.	Var. 1	Var. 2	Var. 3
I_{xx}	(kg-m^2)	399.5	393.143 (8.313)	406.595(0.093)	406.593(0.093)
I_{yy}		404.8	424.006 (8.500)	431.209(0.066)	431.208(0.066)
I_{zz}		527.9	500.215(14.635)	512.045(0.115)	512.044(0.115)
I_{xy}		-0.10	-2.530 (9.253)	-2.827(0.054)	-2.827(0.054)
I_{xz}		0.00	0.727 (9.957)	0.055(0.073)	0.055(0.073)
I_{yz}		4.50	0.499 (9.968)	6.884(0.057)	6.884(0.057)

Table 7.13: Inertia and actuator alignment parameter estimates produced by filter Variants 4, 5, and 6 from MESSENGER data on day 184 of 2008. Filter-produced standard deviations are provided for each parameter in parenthesis.

		Mech. Est.	Var. 4	Var. 5	Var. 6
I_{xx}	(kg-m^2)	399.5	393.142 (8.313)	407.227(0.111)	407.225(0.111)
I_{yy}		404.8	424.006 (8.501)	432.482(0.167)	432.482(0.167)
I_{zz}		527.9	500.220(14.637)	507.184(0.195)	507.185(0.195)
I_{xy}		-0.10	-2.530 (9.253)	-4.024(0.065)	-4.024(0.065)
I_{xz}		0.00	0.727 (9.957)	-0.033(0.089)	-0.033(0.089)
I_{yz}		4.50	0.499 (9.968)	4.875(0.106)	4.875(0.106)
p_{11}	(mrad)	0.000	-0.000 (0.121)	-2.111(0.094)	-2.110(0.094)
p_{12}		0.000	0.003 (0.121)	-1.449(0.099)	-1.448(0.099)
p_{21}		0.000	-0.001 (0.121)	2.282(0.083)	2.281(0.083)
p_{22}		0.000	0.002 (0.121)	0.088(0.088)	0.088(0.088)
p_{31}		0.000	0.001 (0.121)	-0.844(0.073)	-0.844(0.073)
p_{32}		0.000	0.001 (0.121)	2.539(0.077)	2.539(0.077)
p_{41}		0.000	-0.002 (0.121)	-3.741(0.072)	-3.741(0.072)
p_{42}		0.000	0.001 (0.121)	0.172(0.075)	0.172(0.075)

Table 7.14: Inertia parameter estimates produced by filter Variants 1, 2, and 3 from MESSENGER data on day 222 of 2009. Filter-produced standard deviations are provided for each parameter in parenthesis.

		Mech. Est.	Var. 1	Var. 2	Var. 3
I_{xx}	(kg-m^2)	380.5	355.830 (9.061)	389.014(0.099)	389.010(0.099)
I_{yy}		402.1	410.501 (7.905)	428.471(0.067)	428.469(0.067)
I_{zz}		508.8	469.824(14.969)	496.159(0.113)	496.157(0.113)
I_{xy}		-0.10	0.749 (9.990)	-2.670(0.055)	-2.670(0.055)
I_{xz}		0.00	1.285 (9.992)	0.346(0.074)	0.346(0.074)
I_{yz}		4.50	0.439 (9.990)	7.057(0.057)	7.057(0.057)

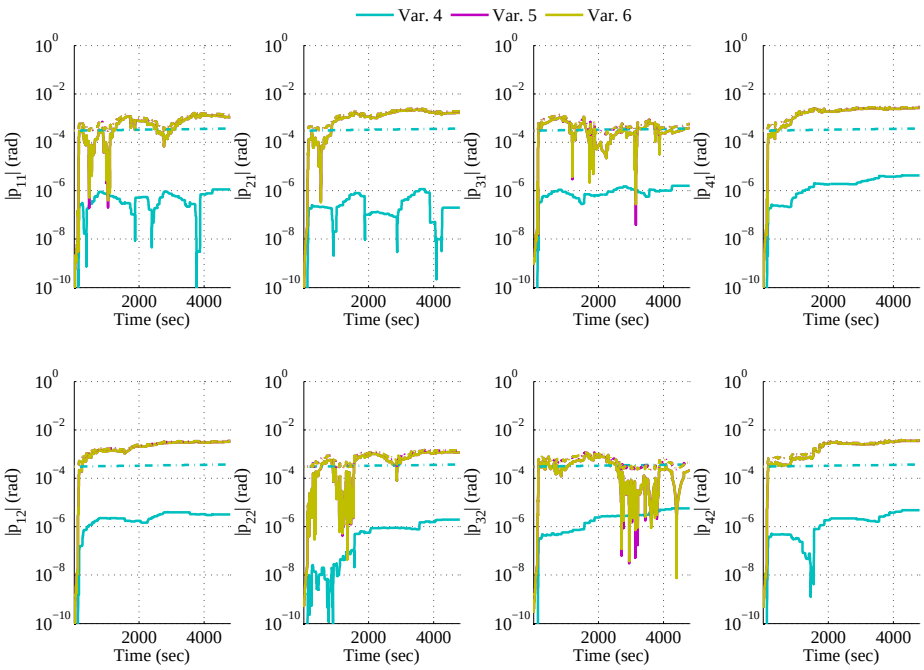

Figure 7.16: Magnitude ofthe momentum actuator alignment parameters for the MESSENGER calibration maneuver that occurred on day 262 of 2007. 3σ upper bounds on the error are provided as dashed lines.

deviations for those parameters when compared to the other estimators. The Variant 2 and 3 estimators produced nearly identical estimates of I and P on a given maneuver date, indicating that the inclusion of rotational kinetic energy in the estimated state had little effect on the produced estimate for the assumed measurement and process noises of the h and T_k states. This observation is further supported by the near-identical performance of the Variant 5 and 6 estimators. The inclusion of P in the estimated states of these two estimators did result in slightly different estimates of the inertia parameters for each of the maneuvers, typically within 2 kg-m^2 of the estimates produced by Variants 2 and 3. Variants 2, 3, 5 and 6 produced similar inertia parameter estimates

Table 7.15: Inertia and actuator alignment parameter estimates produced by filter Variants 4, 5, and 6 from MESSENGER data on day 222 of 2009. Filter-produced standard deviations are provided for each parameter in parenthesis.

		Mech. Est.	Var. 4	Var. 5	Var. 6
I_{xx}	(kg-m^2)	380.5	355.831 (9.061)	389.313(0.118)	389.310(0.118)
I_{yy}		402.1	410.497 (7.907)	428.228(0.178)	428.223(0.178)
I_{zz}		508.8	469.825(14.971)	494.760(0.201)	494.760(0.201)
I_{xy}		-0.10	0.749 (9.990)	-2.787(0.068)	-2.786(0.068)
I_{xz}		0.00	1.285 (9.992)	1.398(0.092)	1.398(0.092)
I_{yz}		4.50	0.439 (9.990)	6.093(0.105)	6.093(0.105)
p_{11}	(mrad)	0.000	-0.004 (0.131)	-3.100(0.082)	-3.102(0.082)
p_{12}		0.000	0.002 (0.131)	1.576(0.086)	1.577(0.086)
p_{21}		0.000	0.000 (0.131)	0.819(0.076)	0.820(0.076)
p_{22}		0.000	0.002 (0.131)	-1.632(0.080)	-1.631(0.080)
p_{31}		0.000	0.001 (0.131)	0.059(0.087)	0.059(0.087)
p_{32}		0.000	0.001 (0.131)	0.685(0.090)	0.685(0.090)
p_{41}		0.000	0.001 (0.131)	-1.672(0.105)	-1.671(0.105)
p_{42}		0.000	0.000 (0.131)	-0.100(0.110)	-0.101(0.110)

across the two-day separation between the calibration maneuvers performed on days 182 and 184 of 2008. As the assumed inertia parameters produced by the mechanical team were identical for these two maneuvers, the consistency of the filter-produced estimates between the two data sets suggest that these inertia parameter estimation methods are reliable.

The reaction wheel axes should not change relative to body coordinates over the four maneuver dates considered. The Variant 4 estimator's actuator-alignment parameter states strongly support this claim, although the overall final state is of questionable quality, since the inertia parameter estimates

differed significantly from the estimates generated by the mechanical team and the other filter variants. The Variant 4 and 5 estimators also support this claim despite the low-magnitude variability in the P parameters at the end of each maneuver.

The observed deviations of the inertia parameters, most noticeably the I_{yy} and I_{zz} terms, from the mechanical prediction could be due to several effects not included in the attitude dynamics model. Imprecise knowledge of the fuel location on the spacecraft can introduce large uncertainties in the inertia parameters. Furthermore, as the estimation methods are for a rigid body spacecraft, motion of the fuel mass or any flexible appendages relative to the spacecraft body create a time-varying angular momentum "sink," whose effects could produce erroneous angular momentum estimates if the motion is of a sufficient magnitude. However, as the mechanical predictions of the MESSENGER spacecraft inertia parameters are still estimates and not necessarily "truth," the actual error in the estimated states is unknown.

7.5 Conclusions

This paper introduces a substantial modification to existing in-orbit inertia parameter estimation techniques by including the angular momentum of the spacecraft as part of the estimated state. This addition is particularly useful for an on-board recursive implementation of the filter, as it allows for the comparison of a predicted spacecraft angular momentum for a given inertia parameter set to an optimal estimate. As the mechanical alignment of momentum actuators on a spacecraft also contributes to the total system

angular momentum, a parameterization of the misalignment error is also included in the estimated state. In addition to an angular momentum-based approach to inertia parameter estimation, the literature also suggests examining the rotational kinetic energy of the spacecraft as a measurement equation for a filtering scheme. While using this scalar measurement equation alone produced generally poor estimates of the actuator-alignment parameters, including both kinetic energy and angular momentum measurement equations in the development of the filter greatly improves the quality of the estimate.

Under simplifying assumptions regarding the torque environment, an estimation scheme based only on an angular momentum measurement equation requires no numerical integration of any of the estimated states, allowing the algorithm to accept infrequent or unevenly-sampled measurements of the spacecraft attitude, angular velocity, and reaction-wheel speeds. Additional artificial process noise affecting the discrete-time dynamics of the angular momentum and inertia parameter states helps compensate for unincorporated, low-magnitude external torques and changes to the physical configuration of the spacecraft. Including kinetic energy as a measurement equation, however, necessitates the numerical integration of the actuator inputs projected onto the spacecraft angular velocity and places more stringent requirements on the sampling frequency of the spacecraft telemetry.

The performance of several parameter estimators including combinations of the angular momentum, kinetic energy, inertia-parameter, and alignment-parameters states were examined over both a simulated maneuver and using telemetry data during maneuvers of the MESSENGER spacecraft. All filters performed satisfactorily when the actuator axes were accurately known in the

simulated data set, but introduction of actuator-alignment errors produced significant deviations from truth in the final state estimates of the filters that did not include an actuator-misalignment parameterization as a state. Additionally, these filters were falsely confident of their estimates, potentially misleading any users of the resulting inertia parameter estimates. Incorporation of the actuator-alignment parameters along with the angular momentum addressed this issue and produced accurate estimates of all quantities. All estimator variations were able to correctly account for the presence of a simple environmental torque model.

All angular momentum-based filters produced reasonable and consistent estimates of the MESSENGER spacecraft inertia parameters over the four calibration maneuvers examined when compared to the estimates obtained by a ground-based calculation based on the presumed configuration of the spacecraft at the time of the maneuvers. The two filters that included actuator-alignment parameters in the estimated state also produced consistent estimates of the actuator axes. The similarity of the inertia estimates produced by the angular momentum-based estimators independent of the inclusion of the actuator-axis alignment parameters suggests that the initial guess of the actuator axes was reasonably accurate. Utilizing only the rotational kinetic energy measurement equation lead to significant deviations from both the estimates produced by the mechanical team and by the other filter variations.

The various filter implementations demonstrated strength in different areas in the simulated maneuvers. When the initial guesses of the actuator axes were correct, leaving the actuator-alignment parameters out of the estimator state resulted in a marginal improvement of the resulting inertia parameter estimates.

Not including these parameters, however, resulted in large errors in the inertia parameters when the initial actuator axes were inaccurately described. When including the alignment parameters, only utilizing the rotational kinetic energy measurement also produced larger errors than filters utilizing the angular momentum measurement equation. Combining both rotational kinetic energy and angular momentum measurements in the estimation algorithm produced slightly improved inertia parameter estimates over only using angular momentum measurements. These algorithms, however, incur additional computational complexity and implementation restrictions due to the real-time numerical integration needed to propagate the rotational kinetic energy state. Without that state, the estimated state have no discrete time dynamics aside from assumed process noise, greatly simplifying implementation. From these observations, the estimation algorithm incorporating angular momentum, inertia, and momentum-actuator alignment parameters represents an optimal combination of parameter estimate quality and ease of implementation. Conditions for determining whether a particular attitude maneuver would result in the inertia and momentum-actuator alignment parameters being observable for this particular estimation algorithm were developed based on an observability Gramian approach.

CHAPTER 8

CONCLUSIONS

This dissertation identifies and examines integrals of motion in the context of fractionated space system architectures. Of specific interest are systems including a non-contacting interaction coupling the dynamics of two spacecraft. Representing forces and torques internal to the larger system, certain integrals of motion, such as angular momentum, are expected to be conserved. Traditional approaches to analyzing the dynamics of these systems, however, rely upon assumptions that violate the conservation of such integrals of motion.

An initial analysis of a model two-spacecraft formation utilizing a novel non-contacting interaction in the form of magnetic flux pinning follows the approach previously examined in the literature. By assuming the center of mass of the formation follows a known Keplerian orbit, the relative motion of the two individual spacecraft can then be described relative to this trajectory and can effectively reduce the size and complexity of the state representing the system configuration. Two equilibrium relative positions with different linear stability properties are identified for this model system. Both of these equilibrium configurations have a separation vector between the spacecraft parallel to the vector locating the formation center of mass relative to the central body, corresponding to a gravity-gradient stabilized orientation. The stable equilibrium configuration corresponds to a separation distance approximately equivalent to the passively stable close-proximity equilibrium separation naturally established by the magnetic flux pinning effect. The unstable equilibrium separation arises from the combined orbital-dynamics and magnetic flux pinning effects. A linear control law is developed to stabilize

this second equilibrium separation and permits stationkeeping of the two-spacecraft formation over larger separations than those suggested by the stable equilibrium.

Study of the magnetic flux pinning effect continues in the approach of the literature by examining a larger formation outside of an orbital context. A system model composed of ten spacecraft in a ring formation connected by magnetic flux pinning is subjected to random disturbance forces and torques. Output parameters that describe the integrity of the ring structure demonstrate the stable equilibrium separation between the spacecraft maintain the desired formation and are compared to the outputs in the absence of the non-contacting interaction.

While these approaches have proven to be of value when examining the relative motion of a fractionated space system, the center of mass motion assumptions impose generalized constraint forces on the system. Energy and momentum integrals of motion for a planar two-spacecraft formation are derived. These conservation laws bound the motion of the system without needing to resort to typical simplifying assumptions. In the presence of these assumptions, the resulting generalized constraint forces introduce a time-dependence to the described integrals of motion. This integral of motion error is directly related to the induced error in the dynamical state due to the center of mass motion assumptions. Linearized expressions for these two forms of error are developed and examined for a simulated system. While the derivation of the integrals of motion in this particular study assumed the use of Photonic Laser Propulsion as the non-contacting interaction, any of the interactions described in Chapter 2 could just as easily be utilized.

The majority of these non-contacting interactions effectively drop off with increased separation distance between spacecraft. This dissertation goes beyond the typical proximity operations problem by instead looking to take advantage of the periodic nature of orbital motion combined with low-thrust non-contacting interactions with limited range. A hybrid systems approach to modeling the dynamics of these systems allows for the representation of different discrete modes with different dynamical functions both with and without the non-contacting interaction. Transitions between these two discrete modes are governed by examining the sensitivities of the orbital parameters of the two spacecraft to the interaction during periods when the spacecraft are in close enough proximity. A sample system utilizing Photonic Laser Propulsion is simulated in an effort to counter atmospheric drag without resorting to traditional chemical or electrical propulsion concepts.

In addition to providing a bounding relationship on the dynamical state of a fractionated space system, integrals of motion are also useful for the purposes of state estimation. This dissertation utilizes the conservation of angular momentum equation for a rigid body in the absence of external torques to extract inertia and momentum actuator alignment parameters from noisy attitude dynamics state measurements. Explicit inclusion of the angular momentum state allows for simple incorporation of both known and random external disturbance torques. Rotational kinetic energy is another measurement equation that could be utilized in this fashion, and several parameter estimator variants are compared over both simulated spacecraft maneuvers and for several telemetry data sets from the MESSENGER spacecraft.

This dissertation provides several avenues for future directions of research.

The development of a relationship between a known error in expressions for the integrals of motion of a fractionated space system and the error in state trajectory introduced by center-of-mass motion assumptions potential validates the simplifications traditionally used to examine the relative motion of fractionated space systems. The hybrid systems model described for countering atmospheric drag utilized a simplified control strategy of interacting whenever the orbital element sensitivities had the correct sign. This approach could be refined by recognizing the periodic nature of the sensitivities. This periodic property allows for development of an approximate control input by splitting the input required to accomplish the desired change in state over a single synodic period of the system. This essentially decomposes the problem into a series of integer programming problems. Finally, integrals of motion can be used for parameter estimation purposes beyond those implemented for a single rigid body spacecraft. As angular momentum is still conserved for these fractionated space systems with a non-contacting interaction, its potential as a measurement equation for a parameter estimator remains.

APPENDIX A

DERIVATION OF EQUATIONS OF MOTION OF A FLUX-PINNED SPACECRAFT PAIR

This appendix formulates in detail both the nonlinear and linearized forms of the equations of motion for the system described in Chapter 3 in the paper.

Configuration Description

The vector $\boldsymbol{\rho}$ that points from the center of mass of the first spacecraft, P_1, to the center of mass of the second spacecraft, P_2, lies parallel to a unit vector $\mathbf{b}_1$ pointing from the center of mass of the formation to either P_1 or P_2.

$$\boldsymbol{\rho} = \boldsymbol{\rho}_2 - \boldsymbol{\rho}_1 = \rho \mathbf{b}_1 = (\rho_1 + \rho_2)\, \mathbf{b}_2 \tag{A.1}$$

From the definition of the formation center of mass, we can define the relation between $\boldsymbol{\rho}_1$ and $\boldsymbol{\rho}_2$:

$$m_1 \boldsymbol{\rho}_1 + m_2 \boldsymbol{\rho}_2 = 0 \tag{A.2}$$

Combining Eqs. (A.1) and (A.2) relates the distance between P_1 and P_2 and the center of mass to the scalar ρ.

$$\rho_1 = \frac{m_2}{M} \rho \tag{A.3a}$$

$$\rho_2 = \frac{m_1}{M} \rho \tag{A.3b}$$

where $M = m_1 + m_2$.

A set of orthonormal basis vectors $\mathbf{b}_1$, $\mathbf{b}_2$, and $\mathbf{b}_3$ are fixed in frame $\mathcal{B}$ that rotates with the formation defined by P_1 and P_2. Similarly, the orthonormal vectors $\hat{\mathbf{r}}$, $\hat{\mathbf{s}}$, and $\hat{\mathbf{w}}$ are fixed in a frame $\mathcal{RSW}$ that rotates with the formation

center of mass. The relative attitude between these two coordinate systems can be described by a direction cosine matrix using two angle measures θ_1 and θ_2:

$$\begin{bmatrix} \mathbf{b}_1 \\ \mathbf{b}_2 \\ \mathbf{b}_3 \end{bmatrix} = \begin{bmatrix} c_1 c_2 & s_1 c_2 & s_2 \\ -s_1 & c_1 & 0 \\ -c_1 s_2 & -s_1 s_2 & c_2 \end{bmatrix} \begin{bmatrix} \hat{\mathbf{r}} \\ \hat{\mathbf{s}} \\ \hat{\mathbf{w}} \end{bmatrix} \tag{A.4}$$

where $s_i = \sin\theta_i$ and $c_i = \cos\theta_i$.

Under the assumption of the formation center of mass traveling on a circular orbit, we need three generalized coordinates to capture the relative motion of P_1 and P_2. Selecting coordinates ρ, θ_1, and θ_2 completely and uniquely describe the range of possible configurations of the system in terms of a spherical coordinate system of two angles and a length:

$$q = \begin{bmatrix} q_1 \\ q_2 \\ q_3 \end{bmatrix} = \begin{bmatrix} \theta_1 \\ \theta_2 \\ \rho \end{bmatrix} \tag{A.5}$$

Velocity Definitions

We can now further define the angular velocity of $\mathcal{B}$ with respect to $\mathcal{N}$ in terms of Ω, $\dot{q}_1$, $\dot{q}_2$, $\mathbf{b}_1$, $\mathbf{b}_2$, and $\mathbf{b}_3$ through use of Eq. (A.4).

$$\begin{aligned} \boldsymbol{\omega} &= (\Omega + \dot{q}_1)\,\hat{\mathbf{w}} - \dot{q}_2 \mathbf{b}_2 \\ &= (\Omega + \dot{q}_1)\, s_2 \mathbf{b}_1 - \dot{q}_2 \mathbf{b}_2 + (\Omega + \dot{q}_1)\, c_2 \mathbf{b}_3 \end{aligned} \tag{A.6}$$

The time derivative of the vector $\boldsymbol{\rho}$ in $\mathcal{B}$ has a simple form:

$$\frac{{}^{B}d}{dt}\boldsymbol{\rho} = \dot{q}_3 \mathbf{b}_1 \tag{A.7}$$

From $\boldsymbol{\omega}$ and ${}^{B}d\boldsymbol{\rho}/dt$, we can define the time derivative of $\boldsymbol{\rho}$ with respect to the inertial frame $\mathcal{N}$:

$$\frac{{}^{N}d}{dt}\boldsymbol{\rho} = \frac{{}^{B}d}{dt}\boldsymbol{\rho} + \boldsymbol{\omega} \times \boldsymbol{\rho}$$

$$= \dot{q}_3 \mathbf{b}_1 + q_3 \left(\Omega + \dot{q}_1\right) c_2 \mathbf{b}_2 + q_3 \dot{q}_2 \mathbf{b}_3 \tag{A.8}$$

Following the method of equation of motion generation outlined by Kane, a set of generalized speeds u_1, u_2, and u_3 need to be defined.[11] These scalar quantities typically represent the measure numbers of a relevant velocity vector expressed in a particular set of basis vectors. Basing the selection of u_1, u_2, and u_3 on the scalar components of ${}^N d\boldsymbol{\rho}/dt$ from Eq. (A.8),

$$u = \begin{bmatrix} u_1 \\ u_2 \\ u_3 \end{bmatrix} = Y(q)\,\dot{q} + Z(q) = \begin{bmatrix} 0 & 0 & 1 \\ c_2 q_3 & 0 & 0 \\ 0 & q_3 & 0 \end{bmatrix} \begin{bmatrix} \dot{q}_1 \\ \dot{q}_2 \\ \dot{q}_3 \end{bmatrix} + \begin{bmatrix} 0 \\ \Omega c_2 q_3 \\ 0 \end{bmatrix} \tag{A.9}$$

Equation (A.9) can be inverted to solve for $\dot{q}$:

$$\dot{q} = W(q)\,\dot{u} + X(q) = \begin{bmatrix} 0 & 1/c_2 q_3 & 0 \\ 0 & 0 & 1/q_3 \\ 1 & 0 & 0 \end{bmatrix} \begin{bmatrix} \dot{q}_1 \\ \dot{q}_2 \\ \dot{q}_3 \end{bmatrix} - \begin{bmatrix} \Omega \\ 0 \\ 0 \end{bmatrix} \tag{A.10}$$

Combining Eqs. (A.3a), (A.3b), (A.8), and (A.9) defines the velocity vectors of P_1 and P_2 relative to their center of mass in the inertial frame $\mathcal{N}$:

$$\frac{{}^N d}{dt}\boldsymbol{\rho}_1 = -\frac{m_2}{M} u_1 \mathbf{b}_1 - \frac{m_2}{M} u_2 \mathbf{b}_2 - \frac{m_2}{M} u_3 \mathbf{b}_3 \tag{A.11a}$$

$$\frac{{}^N d}{dt}\boldsymbol{\rho}_2 = \frac{m_1}{M} u_1 \mathbf{b}_1 + \frac{m_1}{M} u_2 \mathbf{b}_2 + \frac{m_1}{M} u_3 \mathbf{b}_3 \tag{A.11b}$$

These velocities in turn define the partial velocities of P_1 and P_2 in $\mathcal{N}$.

$$\begin{array}{lll} \mathbf{v}_1^{P1} = -\frac{m_2}{M}\mathbf{b}_1 & \mathbf{v}_2^{P1} = -\frac{m_2}{M}\mathbf{b}_2 & \mathbf{v}_3^{P1} = -\frac{m_2}{M}\mathbf{b}_3 \\ \mathbf{v}_1^{P2} = \frac{m_1}{M}\mathbf{b}_1 & \mathbf{v}_2^{P2} = \frac{m_1}{M}\mathbf{b}_2 & \mathbf{v}_3^{P2} = \frac{m_1}{M}\mathbf{b}_3 \end{array} \tag{A.12}$$

Generalized Inertia Forces

From Kane and Levinson, the equations of motion of a system are the sum of the generalized inertia forces and generalized active forces for each of the degrees

of freedom in the system.[11] For an unconstrained system with n generalized speeds and v points of interest, the generalized inertia forces take the following form:

$$\begin{aligned} F_r^* &= \sum_{i=1}^{v} -m_i \mathbf{v}_r^{P_i} \cdot \mathbf{a}_i \\ &= -\frac{1}{2} \sum_{i=1}^{v} m_i \sum_{j=1}^{n} \left(\frac{d}{dt} \frac{\partial}{\partial \dot{q}_j} \mathbf{v}_i^2 - \frac{\partial}{\partial q_j} \mathbf{v}_i^2 \right) W_{jr} \text{ for } r = 1 \ldots n \end{aligned} \tag{A.13}$$

where $\mathbf{v}_i^2$ is the square of the norm of the velocity of P_i, $\mathbf{a}_i$ is the acceleration of P_i, and W_{jr} are elements of the matrix W describing the derivatives of the generalized coordinates in terms of the generalized speeds, as in Eq. (A.10). For the generalized coordinates in Eq. (A.5), generalized speeds in Eq. (A.9), velocities in Eqs. (A.11a) and (A.11b), and partial velocities in Eq. (A.12), the relevant partial derivatives are summed to form the generalized inertia forces of the system:

$$F_1^* = -\frac{m_1 m_2}{M} \left(\dot{u}_1 - \frac{1}{q_3} \left(u_2^2 + u_3^2 \right) \right) \tag{A.14a}$$

$$F_2^* = -\frac{m_1 m_2}{M} \left(\dot{u}_2 + \frac{1}{q_3} \left(u_1 - t_2 u_3 \right) u_2 \right) \tag{A.14b}$$

$$F_3^* = -\frac{m_1 m_2}{M} \left(\dot{u}_3 + \frac{1}{q_3} \left(u_1 u_3 + t_2 u_2^2 \right) \right) \tag{A.14c}$$

where $t_2 = \tan q_2$.

Generalized Active Forces

The generalized active forces associated with a particular generalized speed is the sum of the dot products between force resultants and appropriate partial velocities over all bodies:

$$F_r = \sum_{i=1}^{v} \mathbf{v}_r^{P_i} \cdot \mathbf{R}_i \tag{A.15}$$

The resultants $\mathbf{R}_1$, $\mathbf{R}_2$ are the sum of all forces applied to P_1 and P_2 respectively. In this formulation, these include gravitation ($\mathbf{F}_g$) and the inter-satellite force ($\mathbf{F}$). The gravitational force applied to P_1 can be represented in terms of the generalized coordinates q and constants:

$$\begin{aligned}\mathbf{F}_{g1} &= -\frac{\mu m_1}{r_1^3}\mathbf{r}_1 \\ &= -\mu m_1\left(\left(r_{cm}c_1c_2 - \frac{m_2}{M}q_3\right)\mathbf{b}_1 - r_{cm}s_1\mathbf{b}_2 - r_{cm}c_1s_2\mathbf{b}_3\right)\frac{1}{r_1^3}\end{aligned} \tag{A.16}$$

where $r_1 = \left(r_{cm}^2 - 2r_{cm}\frac{m_2}{M}c_1c_2q_3 + \left(\frac{m_2}{M}q_3\right)\right)^{1/2}$. Similarly, $\mathbf{F}_{g2}$ can be defined in terms of q and constants:

$$\begin{aligned}\mathbf{F}_{g2} &= -\frac{\mu m_2}{r_2^3}\mathbf{r}_2 \\ &= -\mu m_2\left(\left(r_{cm}c_1c_2 + \frac{m_1}{M}q_3\right)\mathbf{b}_1 - r_{cm}s_1\mathbf{b}_2 - r_{cm}c_1s_2\mathbf{b}_3\right)\frac{1}{r_2^3}\end{aligned} \tag{A.17}$$

where $r_2 = \left(r_{cm}^2 + 2r_{cm}\frac{m_1}{M}c_1c_2q_3 + \left(\frac{m_1}{M}q_3\right)\right)^{1/2}$. The inter-spacecraft force $\mathbf{F}$ is assumed to be parallel to and applied at a point along the unit vector $\mathbf{b}_1$ pointing between P_1 and P_2.

$$\mathbf{F} = f(q,u)\,\mathbf{b}_1 \tag{A.18}$$

These force descriptions define of the resultants of P_1 and P_2:

$$\mathbf{R}_1 = \mathbf{F}_{g1} + \mathbf{F} \tag{A.19a}$$

$$\mathbf{R}_2 = \mathbf{F}_{g2} - \mathbf{F} \tag{A.19b}$$

These resultants can then be applied to Eq. (A.15):

$$\mathbf{F}_1 = -\mu\frac{m_1m_2}{M}\left(r_{cm}c_1c_2\left(\frac{1}{r_2^3} - \frac{1}{r_1^3}\right) + \frac{q_3}{M}\left(\frac{m_1}{r_2^3} + \frac{m_2}{r_1^3}\right)\right) - f(q,u) \tag{A.20a}$$

$$\mathbf{F}_2 = \mu\frac{m_1m_2}{M}r_{cm}s_1\left(\frac{1}{r_2^3} - \frac{1}{r_1^3}\right) \tag{A.20b}$$

$$\mathbf{F}_3 = \mu\frac{m_1m_2}{M}r_{cm}c_1s_2\left(\frac{1}{r_2^3} - \frac{1}{r_1^3}\right) \tag{A.20c}$$

Equations of Motion

The equations of motion associated with a particular generalized speed corresponds to the sum of the appropriate generalized inertia force and generalized active force:

$$F_r^* + F_r = 0 \text{ where } r = 1 \ldots 3 \tag{A.21}$$

Summing Eqs. (A.14a) and (A.20a) and solving for $\dot{u}_1$,

$$\dot{u}_1 = \frac{1}{q_3}\left(u_2^2 + u_3^2\right) - \mu\left(r_{cm}c_1c_2\left(\frac{1}{r_2^3} - \frac{1}{r_1^3}\right) + \frac{q_3}{M}\left(\frac{m_1}{r_2^3} + \frac{m_2}{r_1^3}\right)\right) - \frac{M}{m_1m_2}f(q,u) \tag{A.22}$$

Similarly, summing Eqs. (A.14b) and (A.20b) and solving for $\dot{u}_2$,

$$\dot{u}_2 = -\frac{1}{q_3}\left(u_1 - t_2u_3\right)u_2 + \mu r_{cm}s_1\left(\frac{1}{r_2^3} - \frac{1}{r_1^3}\right) \tag{A.23}$$

Finally, summing Eqs. (A.14c) and (A.20c) and solving for $\dot{u}_3$,

$$\dot{u}_3 = -\frac{1}{q_3}\left(u_1u_3 + t_2u_2^2\right) + \mu r_{cm}c_1s_2\left(\frac{1}{r_2^3} - \frac{1}{r_1^3}\right) \tag{A.24}$$

Linearization

Linearizing the nonlinear differential equations (3.4), (3.5a), (3.5b), and (3.5c) about an appropriate equilibrium state allows us to examine the infinitesimal stability properties of the original nonlinear system and perform linear controller synthesis. Linearizing an arbitrary function g of q, u, and μ_{FP},

$$g(q,u,\mu_{FP}) \approx g(\bar{q},\bar{u}) + \left.\frac{\partial g}{\partial q}\right|_0 q^* + \left.\frac{\partial g}{\partial u}\right|_0 u^* + \left.\frac{\partial g}{\partial \mu_{FP}}\right|_0 \mu_{FP}^* \tag{A.25}$$

where $q = q^* + \bar{q}$, $u = u^* + \bar{u}$, and $\mu_{FP} = \mu_{FP}^* + \bar{\mu}_{FP}$.

Applying Eq. (A.25) to Eqs. (3.4), (3.5a), (3.5b), and (3.5c) and arranging in a matrix format,

$$\begin{bmatrix} \dot{q}_1^* \\ \dot{q}_2^* \\ \dot{q}_3^* \\ \dot{u}_1^* \\ \dot{u}_2^* \\ \dot{u}_3^* \end{bmatrix} = \begin{bmatrix} 0 & \frac{\partial \dot{q}_1}{\partial q_2} & \frac{\partial \dot{q}_1}{\partial q_3} & 0 & \frac{\partial \dot{q}_1}{\partial u_2} & 0 \\ 0 & 0 & \frac{\partial \dot{q}_2}{\partial q_3} & 0 & 0 & \frac{\partial \dot{q}_2}{\partial u_3} \\ 0 & 0 & \frac{\partial \dot{q}_3}{\partial q_3} & 0 & 0 & 0 \\ \frac{\partial \dot{u}_1}{\partial q_1} & \frac{\partial \dot{u}_1}{\partial q_2} & \frac{\partial \dot{u}_1}{\partial q_3} & \frac{\partial \dot{u}_1}{\partial u_1} & \frac{\partial \dot{u}_1}{\partial u_2} & \frac{\partial \dot{u}_1}{\partial u_3} \\ \frac{\partial \dot{u}_2}{\partial q_1} & \frac{\partial \dot{u}_2}{\partial q_2} & \frac{\partial \dot{u}_2}{\partial q_3} & \frac{\partial \dot{u}_2}{\partial u_1} & \frac{\partial \dot{u}_2}{\partial u_2} & \frac{\partial \dot{u}_2}{\partial u_3} \\ \frac{\partial \dot{u}_3}{\partial q_1} & \frac{\partial \dot{u}_3}{\partial q_2} & \frac{\partial \dot{u}_3}{\partial q_3} & \frac{\partial \dot{u}_3}{\partial u_1} & \frac{\partial \dot{u}_3}{\partial u_2} & \frac{\partial \dot{u}_3}{\partial u_3} \end{bmatrix}_0 \begin{bmatrix} q_1^* \\ q_2^* \\ q_3^* \\ u_1^* \\ u_2^* \\ u_3^* \end{bmatrix} + \begin{bmatrix} 0 \\ 0 \\ 0 \\ \frac{\partial \dot{u}_1}{\partial \mu_{FP}} \\ 0 \\ 0 \end{bmatrix}_0 \mu_{FP}^* \tag{A.26}$$

$$\begin{bmatrix} \dot{q}^* \\ \dot{u}^* \end{bmatrix} = A(\bar{q}, \bar{u}, \bar{\mu}_{FP}) \begin{bmatrix} q^* \\ u^* \end{bmatrix} + B(\bar{q}, \bar{u}, \bar{\mu}_{FP}) \mu_{FP}^* \tag{A.27}$$

This corresponds to a state space representation of the linearized system. The partial derivatives from Eq. (A.26) are:

$$\frac{\partial \dot{q}_1}{\partial q_2} = \frac{t_2 u_2}{c_2 q_3} \qquad \frac{\partial \dot{q}_1}{\partial q_3} = -\frac{u_2}{c_2 q_3^2} \qquad \frac{\partial \dot{q}_1}{\partial u_2} = \frac{1}{c_2 q_3} \qquad \frac{\partial \dot{q}_2}{\partial q_3} = -\frac{u_3}{q_3^2} \qquad \frac{\partial \dot{q}_2}{\partial u_3} = \frac{1}{q_3} \qquad \frac{\partial \dot{q}_3}{\partial u_1} = 1$$

$$\frac{\partial \dot{u}_1}{\partial q_1} = \mu \left(r_{cm} s_1 c_2 \left(\frac{1}{r_2^3} - \frac{1}{r_1^3} \right) - \left(r_{cm} c_1 c_2 + \frac{m_1}{M} q_3 \right) \frac{\partial}{\partial q_1} r_2^{-3} + \left(r_{cm} c_1 c_2 - \frac{m_2}{M} q_3 \right) \frac{\partial}{\partial q_1} r_1^{-3} \right)$$

$$\frac{\partial \dot{u}_1}{\partial q_2} = \mu \left(r_{cm} c_1 s_2 \left(\frac{1}{r_2^3} - \frac{1}{r_1^3} \right) - \left(r_{cm} c_1 c_2 + \frac{m_1}{M} q_3 \right) \frac{\partial}{\partial q_2} r_2^{-3} + \left(r_{cm} c_1 c_2 - \frac{m_2}{M} q_3 \right) \frac{\partial}{\partial q_2} r_1^{-3} \right)$$

$$\begin{aligned} \frac{\partial \dot{u}_1}{\partial q_3} = & -\mu \left(\left(r_{cm} c_1 c_2 + \frac{m_1}{M} q_3 \right) \frac{\partial}{\partial q_3} r_2^{-3} - \left(r_{cm} c_1 c_2 - \frac{m_2}{M} q_3 \right) \frac{\partial}{\partial q_3} r_1^{-3} \right. \\ & \left. + \frac{1}{M} \left(\frac{m_1}{r_2^3} + \frac{m_2}{r_1^3} \right) \right) - \frac{1}{q_3^2} \left(u_2^2 + u_3^2 \right) + \frac{M}{m_1 m_2} \frac{\partial f}{\partial q_3} \end{aligned}$$

$$\frac{\partial \dot{u}_2}{\partial q_1} = \mu r_{cm} \left(s_1 \left(\frac{\partial}{\partial q_1} r_2^{-3} - \frac{\partial}{\partial q_1} r_1^{-3} \right) + c_2 \left(r_2^{-3} - r_1^{-3} \right) \right)$$

$$\frac{\partial \dot{u}_2}{\partial q_2} = \frac{u_2 u_3}{q_3 c_2^2} + \mu r_{cm} s_1 \left(\frac{\partial}{\partial q_2} r_2^{-3} - \frac{\partial}{\partial q_2} r_1^{-3} \right)$$

$$\frac{\partial \dot{u}_2}{\partial q_3} = \frac{1}{q_3^2} \left(u_1 - t_2 u_3 \right) u_2 + r_{cm} s_1 \left(\frac{\partial}{\partial q_1} r_2^{-3} - \frac{\partial}{\partial q_1} r_1^{-3} \right)$$

$$\frac{\partial \dot{u}_3}{\partial q_1} = \mu r_{cm} s_2 \left(c_1 \left(\frac{\partial}{\partial q_1} r_2^{-3} - \frac{\partial}{\partial q_1} r_1^{-3} \right) - s_1 \left(r_2^{-3} - r_1^{-3} \right) \right)$$

$$\frac{\partial \dot{u}_3}{\partial q_2} = -\frac{u_2^2}{q_3 c_2^2} + \mu r_{cm} c_1 \left(s_2 \left(\frac{\partial}{\partial q_2} r_2^{-3} - \frac{\partial}{\partial q_2} r_1^{-3} \right) + c_2 \left(r_2^{-3} - r_1^{-3} \right) \right)$$
$$\frac{\partial \dot{u}_3}{\partial q_3} = \frac{1}{q_3} \left(u_1 u_3 + t_2 u_2^2 \right) \mu r_{cm} c_1 s_2 \left(\frac{\partial}{\partial q_3} r_2^{-3} - \frac{\partial}{\partial q_3} r_1^{-3} \right)$$

$$\frac{\partial \dot{u}_1}{\partial u_1} = \frac{M}{m_1 m_2} \frac{\partial f}{\partial u_1} \qquad \frac{\partial \dot{u}_1}{\partial u_2} = \frac{2u_2}{q_3} \qquad \frac{\partial \dot{u}_1}{\partial u_3} = \frac{2u_3}{q_3}$$
$$\frac{\partial \dot{u}_2}{\partial u_1} = -\frac{u_2}{q_3} \qquad \frac{\partial \dot{u}_2}{\partial u_2} = \frac{1}{q_3} (t_2 u_3 - u_1) \qquad \frac{\partial \dot{u}_2}{\partial u_3} = \frac{t_2 u_2}{q_3}$$
$$\frac{\partial \dot{u}_3}{\partial u_1} = -\frac{u_3}{q_3} \qquad \frac{\partial \dot{u}_3}{\partial u_2} = -2\frac{t_2 u_2}{q_3} \qquad \frac{\partial \dot{u}_3}{\partial u_3} = -\frac{u_1}{q_3}$$

The previous set of equations make use of a few extra partial derivatives:

$$\frac{\partial}{\partial q_1} r_1^{-3} = -3\frac{m_2 r_{cm}}{M r_1^5} s_1 c_2 q_3 \qquad \frac{\partial}{\partial q_1} r_2^{-3} = 3\frac{m_1 r_{cm}}{M r_2^5} s_1 c_2 q_3$$
$$\frac{\partial}{\partial q_2} r_1^{-3} = -3\frac{m_2 r_{cm}}{M r_1^5} c_1 s_2 q_3 \qquad \frac{\partial}{\partial q_2} r_2^{-3} = 3\frac{m_1 r_{cm}}{M r_2^5} c_1 s_2 q_3$$
$$\frac{\partial}{\partial q_3} r_1^{-3} = 3\frac{m_2}{M r_1^5} \left(r_{cm} c_1 c_2 + \frac{m_2}{M} q_3 \right) \qquad \frac{\partial}{\partial q_3} r_2^{-3} = -3\frac{m_1}{M r_2^5} \left(r_{cm} c_1 c_2 - \frac{m_1}{M} q_3 \right)$$

$$\frac{\partial f}{\partial u_1} = C$$
$$\frac{\partial f}{\partial q_3} = -6\frac{\mu_0 \mu_{FP}^2}{\pi} \left(\frac{1}{(q_3 - \delta_1 - \delta_2 + d_0)^5} - \frac{1}{16 (q_3 - \delta_1 - \delta_2)^5} \right)$$
$$\frac{\partial f}{\partial \mu_{FP}} = 3\frac{\mu_0 \mu_{FP}}{\pi} \left(\frac{1}{(q_3 - \delta_1 - \delta_2 + d_0)^4} - \frac{1}{16 (q_3 - \delta_1 - \delta_2)^4} \right)$$

APPENDIX B

ACTUATOR-ALIGNMENT ERROR PARAMETERIZATION

The true axis for the i^{th} actuator, a_i, and the best initial estimate of that same axis, $\hat{a}_i$, are separated by the angle ϕ_i. The corresponding unit-norm axis of rotation, β_i, is by definition perpendicular to both a_i and $\hat{a}_i$. Representing this rotation as a set of Modified Rodriguez Parameters (MRPs) allows for the simple description of the actuator-axis alignment error:

$$\rho_i = \beta_i \tan\frac{\phi_i}{4} \tag{B.1}$$

The rotation matrix corresponding to ρ_i is defined as

$$Q(\rho_i) = 1_3 - \frac{4\left(1-\rho_i^T\rho_i\right)}{\left(1+\rho_i^T\rho_i\right)^2}\rho_i^x + \frac{8}{\left(1+\rho_i^T\rho_i\right)^2}\rho_i^x\rho_i^x \tag{B.2}$$

In general, ρ_i describe a three-parameter representation of the rotation between two sets of coordinates. For the present case of estimating a body-fixed axis, an appropriate choice of these coordinates can further reduce ρ_i to an unambiguous two-parameter set.

Combining the initial estimated actuator axis with two arbitrary, constant, perpendicular directions defines a rotation matrix between actuator and spacecraft body coordinates:

$${}^kQ^{gi} = \begin{bmatrix}\alpha_{1,i} & \alpha_{2,i} & \hat{a}_i\end{bmatrix} \tag{B.3}$$

Because β_i is by definition perpendicular to $\hat{a}_i$, its representation in the initial "guessed" actuator coordinates consists of only two non-zero parameters:

$$\beta_i = {}^kQ^{gi}\begin{bmatrix}b_{1,i}\\ b_{2,i}\\ 0\end{bmatrix} = {}^kQ^{gi}b_i \tag{B.4}$$

Using b_i instead of β_i to define the MRP set from equation (B.1) corresponds to defining the actuator-alignment error parameters with respect to the initial guess instead of the spacecraft body coordinates and produces a parameter set with only two non-zero values.

$$\rho_i = \begin{bmatrix} b_{1,i} \\ b_{2,i} \\ 0 \end{bmatrix} \tan\frac{\phi_i}{4} = \begin{bmatrix} p_i \\ 0 \end{bmatrix} \tag{B.5}$$

The true actuator axis can then be defined in terms of a known ${}^{k}Q^{gi}$ and alignment error parameters p_i with the use of equation (B.2):

$$a_i = {}^{k}Q^{gi} Q\left(\begin{bmatrix} p_i \\ 0 \end{bmatrix}\right)\begin{bmatrix} 0 \\ 0 \\ 1 \end{bmatrix} \tag{B.6}$$

Equation (B.6) can be linearized about a current estimate of the actuator-alignment parameters, $\bar{p}_i$. Crassidis and Markley provided a compact representation of the linearized effects of variations in a MRP set on a given vector observation.[78] This linearization can be re-interpreted as describing small variations in the estimated actuator axes:

$$a_i \approx \bar{a}_i + \left[\frac{\partial a_i}{\partial p_i}\right](p_i - \bar{p}_i) \tag{B.7}$$

where

$$\bar{a}_i = {}^{k}Q^{gi} Q\left(\begin{bmatrix} \bar{p}_i \\ 0 \end{bmatrix}\right)\begin{bmatrix} 0 \\ 0 \\ 1 \end{bmatrix} \tag{B.8}$$

$$\left[\frac{\partial a_i}{\partial p_i}\right] = \frac{4}{\left(1 + \bar{p}_i^T \bar{p}_i\right)^2} {}^{k}Q^{gi} Q\left(\begin{bmatrix} \bar{p}_i \\ 0 \end{bmatrix}\right)\begin{bmatrix} 0 \\ 0 \\ 1 \end{bmatrix}^{x}\left(\left(1 - \bar{p}_i^T \bar{p}_i\right) 1_3 - 2\begin{bmatrix} \bar{p}_i \\ 0 \end{bmatrix}^{x} + 2\begin{bmatrix} \bar{p}_i \bar{p}_i^T \\ 0 \end{bmatrix}\right)\begin{bmatrix} 1 & 0 \\ 0 & 1 \\ 0 & 0 \end{bmatrix} \tag{B.9}$$

BIBLIOGRAPHY

[1] Brown, O. and Eremenko, P., "Fractionated Space Architectures: A Vision for Responsive Space," AIAA paper RSA-2006-1002, 2006.

[2] Brown, O., Eremenko, P., and Collopy, P. D., "Value-Centric Design Methodologies for Fractionated Spacecraft: Progress Summary from Phase I of the DARPA System F6 Program," AIAA paper 2009-6540, Sept. 2009.

[3] Guzman, J. and Edery, A., "Mission design for the MMS tetrahedron formation," *Proceedings of the 2004 IEEE Aerospace Conference*, Vol. 1, March 2004, pp. 533–540.

[4] Campbell, M., "Planning Algorithm for Multiple Satellite Clusters," *AIAA Journal of Guidance, Control, and Dynamics*, Vol. 26, No. 5, Sept-Oct 2003, pp. 770–780.

[5] Zanon, D. J. and Campbell, M. E., "Optimal Planner for Spacecraft Formations in Elliptical Orbits," *Journal of Guidance, Control, and Dynamics*, Vol. 29, No. 1, Jan. - Feb. 2006, pp. 161–171, DOI: 10.2514/1.7236.

[6] Clohessy, W. H. and Wiltshire, R. S., "Terminal Guidance System for Satellite Rendezvous," *Journal of the Aerospace Sciences*, Vol. 27, No. 9, 1960, pp. 653–674.

[7] Vaddi, S. S., Vadali, S. R., and Alfriend, K. T., "Formation Flying: Accomodating Nonlinearity and Eccentricity Perturbations," *Journal of Guidance, Control, and Dynamics*, Vol. 26, No. 2, March - April 2003, pp. 214–223.

[8] Berryman, J. and Schaub, H., "Analytical Charge Analysis for Two- and Three-Craft Coulomb Formations," *Journal of Guidance, Control, and Dynamics*, Vol. 30, No. 6, Nov.-Dec. 2007, pp. 1701–1710, DOI: 10.2514/1.23785.

[9] Hamel, J.-F. and de Lafontaine, J., "Linearized Dynamics of Formation Flying Spacecraft on a J2-Perturbed Elliptical Orbit," *Journal of Guidance, Control, and Dynamics*, Vol. 30, No. 6, Nov.-Dec. 2007, pp. 1649–1658.

[10] Ahn, C. and Kim, Y., "Point Targeting of Multisatellites via a Virtual Structure Formation Flight Scheme," *Journal of Guidance, Control, and Dynamics*, Vol. 32, No. 4, July-August 2009, pp. 1330–1344.

[11] Kane, T. R. and Levinson, D. A., "Formulation of Equations of Motion," *Dynamics: Theory and Applications*, McGraw-Hill, New York, 1985, pp. 158–186.

[12] Natarajan, A. and Schaub, H., "Linear Dynamics and Stability Analysis of a Two-Craft Coulomb Tether Formation," *Journal of Guidance, Control, and Dynamics*, Vol. 29, No. 4, August 2006, pp. 831–838.

[13] Tragesser, S. G., "Static Formations Using Momentum Exchange Between Satellites," *Journal of Guidance, Control, and Dynamics*, Vol. 32, No. 4, July-August 2009, pp. 1277–1286.

[14] Schaub, H. and Junkins, J. L., *Analytical Mechanics of Space Systems*, chap. 5, American Institute of Aeronautics and Astronautics, 2003, pp. 213–218.

[15] Schaub, H. and Junkins, J. L., *Analytical Mechanics of Space Systems*, chap. 12, American Institute of Aeronautics and Astronautics, 2003, pp. 508–509.

[16] Landecker, P. B., Villani, D. D., and Yung, K. W., "An Analytic Solution for the Torque Between Two Magnetic Dipoles," *Magnetic and Electrical Separation*, Vol. 10, 1999, pp. 29–33.

[17] Miller, D., Sedwick, R., Kong, E., and Schweighart, S., "Electromagnetic Formation Flight for Sparse Aperture Telescopes," *Aerospace Conference Proceedings*, Vol. 2, 2002, pp. 2–729 – 2–741, DOI: 10.1109/AERO.2002.1035616.

[18] Kong, E. M. C., Kwon, D. W., Schweighart, S. A., Elias, L. M., Sedwick, R. J., and Miller, D. W., "Electromagnetic Formation Flight for Multisatellite Arrays," *Journal of Spacecraft and Rockets*, Vol. 41, No. 4, July-August 2004, pp. 659–666.

[19] Elias, L. M., Kwon, D. W., Sedwick, R. J., and Miller, D. W., "Electromagnetic Formation Flight Dynamics Including Reaction Wheel Gyroscopic Stiffening Effects," *Journal of Guidance, Control, and Dynamics*, Vol. 30, No. 2, March-April 2007, pp. 499–511.

[20] Schaub, H., "Stabilization of Satellite Motion Relative to a Coulomb Spacecraft Formation," *Journal of Guidance, Control, and Dynamics*, Vol. 28, No. 6, November-December 2005, pp. 1231–1239.

[21] Kim, M. and Schaub, H., "Coulomb formation conservation laws using differential orbit elements." *Proceedings of the Institution of Mechanical*

Engineers – Part G – Journal of Aerospace Engineering, Vol. 220, No. 5, 2006, pp. 463 – 474.

[22] Bae, Y. K., "Photonic Laser Propulsion: Proof-of-Concept Demonstration," *Journal of Spacecraft and Rockets*, Vol. 45, No. 1, 2008, pp. 153–155.

[23] Hellman, F., Gyorgy, E. M., Johnson, D. W., O'Bryan, H. M., and Sherwood, R. C., "Levitation of a magnet over a flat type II superconductor." *Journal of Applied Physics*, Vol. 63, No. 2, 1988, pp. 447.

[24] Tsuchimoto, M., Kojima, T., Takeuchi, H., and Honma, T., "Numerical Analyses of Levitation Force and Flux Creep on High T_C Superconductor," *Magnetics, IEEE Transactions on*, Vol. 29, No. 6, Nov 1993, pp. 3577–3579.

[25] Hull, J. R. and Cansiz, A., "Vertical and Lateral Forces Between a Permanent Magnet and High-Temperature Superconductor," *Journal of Applied Physics*, Vol. 86, No. 11, 1999, pp. 6396–6404, DOI: 10.1063/1.371703.

[26] Kordyuk, A. A., "Magnetic Levitation for Hard Superconductors," *Journal of Applied Physics*, Vol. 83, No. 1, Jan 1998, pp. 610–613.

[27] Shoer, J. P., "Flux-Pinned Interfaces for the Assembly, Manipulation, and Reconfiguration of Modular Space Systems," *Proceedings of the 2008 AIAA Guidance, Navigation and Control Conference and Exhibit*, AIAA, Honolulu, Hawaii, August 18-21 2008.

[28] Shoer, J. and Peck, M., "Stiffness Of A Flux-Pinned Virtual Structure For Modular Spacecraft," *Journal of the British Interplanetary Society*, Vol. 62, No. 2, February 2009, pp. 57–65.

[29] Norman, M. C. and Peck, M. A., "A Simplified Model of a Flux-Pinned Spacecraft Formation," *Journal of Guidance, Control, and Dynamics*, Vol. 33, No. 3, May-June 2010, pp. 814–822.

[30] Burke, J. and Murphy, R., "Human-Robot Interaction in USAR Technical Search: Two Heads Are Better Than One," *13th IEEE International Workshop on Robot and Human Interactive Communication, 2004*, Sept. 2004, pp. 307–312, DOI: 10.1109/ROMAN.2004.1374778.

[31] Lawson, P., "The Terrestrial Planet Finder," *Proceedings of the 2001 IEEE Aerospace Conference*, Vol. 4, 2001, pp. 2005–2011.

[32] Inalhan, G., Tillerson, M., and How, J. P., "Relative Dynamics and Control of Spacecraft Formations in Eccentric Orbits," *Journal of Guidance, Control, and Dynamics*, Vol. 25, No. 1, Jan. - Feb. 2002, pp. 48–59, DOI: 10.2514/2.4874.

[33] Ulybyshev, Y., "Long-Term Formation Keeping of Satellite Constellations Using Linear-Quadratic Controller," *Journal of Guidance, Control, and Dynamics*, Vol. 21, No. 1, Jan. - Feb. 1998, pp. 109–115, DOI: 10.2514/2.4204.

[34] Millard, L. and Howell, K., "Control of Interferometric Spacecraft Arrays for (U,V) Plane Coverage in Multi-Body Regimes," AAS paper 07-153, Jan. 2007.

[35] Hamel, J.-F. and de Lafontaine, J., "Neighboring Optimum Feedback Control Law for Earth-Orbiting Formation-Flying Spacecraft," *Journal of Guidance, Control, and Dynamics*, Vol. 32, No. 1, 2009, pp. 290–299, DOI: 10.2514/1.32778.

[36] Atchison, J. A. and Peck, M. A., "A Millimeter-Scale Lorentz-Propelled Spacecraft," AIAA paper 2007-6847, Aug. 2007.

[37] Earnshaw, S., "On the Nature of the Molecular Forces which Regulate the Constitution of the Luminiferous Ether," *Transactions of the Cambridge Philosophical Society*, Vol. 7, No. 1, 1842, pp. 97–112.

[38] Shoer, J. P. and Peck, M. A., "Reconfigurable Spacecraft as Kinematic Mechanisms," *Journal of Spacecraft and Rockets*, Vol. 46, No. 2, March - April 2009, pp. 466–469, DOI: 10.2514/1.37641.

[39] Yang, Z. J. and Hull, J. R., "Effect of Size on Levitation Force in a Magnet/Superconductor System," *Journal of Applied Physics*, Vol. 79, No. 6, 1996, pp. 3318–3322, DOI: 10.1063/1.361232.

[40] Johansen, T. H., Mestl, H., and Bratsberg, H., "Investigation of the Lateral Magnetic Force and Stiffness Between a High-T_C Superconductor and Magnet of Rectangular Shapes," *Journal of Applied Physics*, Vol. 75, No. 3, February 1994, pp. 1667–1670, DOI: 10.1063/1.356351.

[41] Chang, P.-Z., Moon, F. C., Hull, J. R., and Mulcahy, T. M., "Levitation Force and Magnetic Stiffness in Bulk High-Temperature Superconductors," *Journal of Applied Physics*, Vol. 67, No. 9, 1990, pp. 4358–4360, DOI: 10.1063/1.344927.

[42] Norman, M. C. and Peck, M. A., "Stationkeeping of a Flux-Pinned Satellite Network," *Journal of Guidance, Control, and Dynamics*, Vol. 33, No. 5, September-October 2010, pp. 1683–1687.

[43] Brown, O. and Eremenko, P., "The Value Proposition For Fractionated Space Architectures," AIAA paper 2006-7506, Sept. 2006.

[44] Ahsun, U. and Miller, D. W., "Dynamics and Control of Electromagnetic Satellite Formations," *Proceedings of the 2006 American Control Conference*, IEEE, Minneapolis, Minnesota, USA, June 14-16 2006, pp. 1730–1735.

[45] Brandt, E. H., "Friction in levitated superconductors." *Applied Physics Letters*, Vol. 53, No. 16, 1988, pp. 1554.

[46] Yamachi, N., Nishikawa, T., Sakai, N., Sawa, K., and Murakami, M., "Levitation forces of bulk superconductors in varying fields," *Physica C*, 2003, pp. 579–584.

[47] Meinel, A. B. and Meinel, M. P., "Large sparse-aperture space optical systems," *Optical Engineering*, Vol. 41, No. 8, 2002, pp. 1983–1994.

[48] Vallado, D. A., *Fundamentals of Astrodynamics and Applications*, chap. 8, Microcosm Press, Hawthorne, CA, 2007, pp. 574–578.

[49] Norman, M. C. and Peck, M. A., "Integrals of Motion for Planar Multibody Formations with Internal Forces," *Journal of Guidance, Control, and Dynamics*, (to appear).

[50] Murray, C. D. and Dermott, S. F., *Solar System Dynamics*, chap. 3.3, Cambridge University Press, Cambridge, UK, 1999, pp. 68–72.

[51] Leimkuhler, B. and Reich, S., "Symplectic Integration of Constrained Hamiltonian Systems," *Mathematics of Computation*, Vol. 63, 1994, pp. 589–605.

[52] Reich, S., "Momentum Conserving Symplectic Integrators," *Physica D*, Vol. 76, 1994, pp. 375–383.

[53] Leyendecker, S., Marsden, J. E., and Ortiz, M., "Variational Integrators for Constrained Dynamical Systems," *Journal of Applied Mathematics and Mechanics*, Vol. 88, No. 9, September 2008, pp. 677–708.

[54] Bloch, A. M., Hussein, I. I., Leok, M., and Sanyal, A. K., "Geometic Structure-Preserving Optimal Control of a Rigid Body," *Journal of Dynamical and Control Systems*, Vol. 15, No. 3, July 2009, pp. 307–330.

[55] Murray, C. D. and Dermott, S. F., *Solar System Dynamics*, chap. 2, Cambridge University Press, Cambridge, UK, 1999, pp. 22–62.

[56] Bae, Y. K., "Photonic Laser Propulsion (PLP): Photon Propulsion Using an Active Resonant Optical Cavity," *Proceedings of the 2007 AIAA SPACE Conference and Exposition*, AIAA, Long Beach, California, Sept. 18-20 2007.

[57] Norman, M. C. and Peck, M. A., "Orbit Maneuvers Through Inter-Satellite Forcing," AIAA paper 2009-6097, August 2009.

[58] Shoer, J. P. and Peck, M. A., "A Flux-Pinned Magnet-Superconductor Pair for Close-Proximity Station Keeping and Self-Assembly of Spacecraft," *Proceedings of the 2007 AIAA Guidance, Navigation, and Control Conference and Exhibit*, AIAA, Hilton Head, South Carolina, 2007.

[59] Tragesser, S. G., "Static Formations Using Momentum Exchange Between Satellites," *Proceedings of the 2008 AIAA/AAS Astrodynamics Specialist Conference and Exhibit*, AIAA/AAS, Honolulu, Hawaii, August 18-21 2008.

[60] Burns, J. A., "Elementary derivation of the perturbation equations of celestial mechanics," *American Journal of Physics*, Vol. 44, No. 10, October 1976, pp. 944–949.

[61] Stursberg, O. and Krogh, B. H., "Efficient Representation and Computation of Reachable Sets for Hybrid Systems," *Hybrid Systems: Computation and Control*, 2003, pp. 482–497.

[62] Bemporad, A. and Giorgetti, N., "Logic-based solution methods for optimal control of hybrid systems," *IEEE Transactions on Automatic Control*, Vol. 51, No. 6, June 2006, pp. 963–976.

[63] Vallado, D. A., *Fundamentals of Astrodynamics and Applications*, Microcosm Press, Hawthorne, CA, 2007.

[64] Wertz, J. R. and Larson, W. J., editors, *Space Mission Analysis And Design*, Microcosm Press, 3rd ed., 1999.

[65] Norman, M. C., Peck, M. A., and O'Shaughnessy, D. J., "In-Orbit

Estimation of Inertia and Momentum-Actuator Alignment Parameters," *Journal of Guidance, Control, and Dynamics*, (to appear).

[66] Bergmann, E. V., Walker, B. K., and Levy, D. R., "Mass Property Estimation for Control of Asymmetrical Satellites," *Journal of Guidance*, Vol. 10, No. 5, September-October 1987, pp. 483–491.

[67] Wilson, E., Sutter, D. W., and Mah, R. W., "Motion-Based Mass- and Thruster-Property Identification for Thruster-Controlled Spacecraft," *Infospace@Aerospace*, No. AIAA-2005-6907, AIAA, Arlington, VA, September 2005.

[68] Thienel, J. K., Luquette, R. J., and Sanner, R. M., "Estimation of Spacecraft Inertia Parameters," *AIAA Guidance, Navigation, and Control Conference*, No. AIAA-2008-6454, AIAA, Honolulu, HI, August 2008, pp. 1–8.

[69] Fosbury, A. M. and Nebelecky, C. K., "Spacecraft Actuator Alignment Estimation," *AIAA Guidance, Navigation, and Control Conference*, No. AIAA-2009-6316, AIAA, Chicago, IL, August 2009, pp. 1–18.

[70] Tanygin, S. and Williams, T., "Mass Property Estimation using Coasting Maneuvers," *Journal of Guidance, Control, and Dynamics*, Vol. 20, No. 4, July - August 1997, pp. 625–632.

[71] Peck, M. A., "Mass-Properties Identification for Spacecraft with Powerful Damping," *Advances in the Astronautical Sciences*, Vol. 103, AAS, San Diego, CA, August 1999, pp. 2005–2024.

[72] Peck, M. A., "Attitude Determination for Gyrostats in Non-Equilibrium Spins from Infrequent Vector Observations," *AIAA Guidance, Navigation, and Control Conference*, No. AIAA-2000-3946, AIAA, Denver, CO, August 2000, pp. 1–11.

[73] Peck, M. A., "Attitude Propagation with Intermittent Gyro Measurements and Single-Vector Observations," *AAS/AIAA Astrodynamics Specialist Conference*, No. AIAA-2000-4243, Denver, CO, August 2000, pp. 331–338.

[74] Peck, M. A., "Estimation of Inertia Parameters for Gyrostats Subject to Gravity-Gradient Torques," *Advances in the Astronautical Sciences*, Vol. 109, AAS, San Diego, CA, August 2001, pp. 113–132.

[75] Lee, A. Y. and Wertz, J. A., "In-Flight Estimation of the Cassini Spacecraft's

Inertia Tensor," *Journal of Spacecraft and Rockets*, Vol. 39, No. 1, January-February 2002, pp. 153–155.

[76] Psiaki, M. L., "Estimation of a Spacecraft's Attitude Dynamics Parameters by Using Flight Data," *Journal of Guidance, Control, and Dynamics*, Vol. 28, No. 4, July-August 2005, pp. 594–603.

[77] Lefferts, E. J., Markley, F. L., and Shuster, M. D., "Kalman Filtering for Spacecraft Attitude Estimation," *Journal of Guidance*, Vol. 5, No. 5, September-October 1982, pp. 417–429.

[78] Crassidis, J. L. and Markley, F. L., "Attitude Estimation Using Modified Rodriguez Parameters," *Proceedings of the Flight Mechanics/Estimation Theory Symposium*, NASA-Goddard Space Flight Center, Greenbelt, MD, May 1996, pp. 71–83.

[79] Crassidis, J. L., Markley, F. L., and Cheng, Y., "Survey of Nonlinear Attitude Estimation Methods," *Journal of Guidance, Control, and Dynamics*, Vol. 30, No. 1, January-February 2007, pp. 12–28.

[80] Mortari, D., Markley, F. L., and Singla, P., "Optimal Linear Attitude Estimator," *Journal of Guidance, Control, and Dynamics*, Vol. 30, No. 6, Nov.-Dec. 2007, pp. 1619–1627.

[81] Markley, F. L. and Sedlak, J. E., "Kalman Filter for Spinning Spacecraft Attitude Estimation," *Journal of Guidance, Control, and Dynamics*, Vol. 31, No. 6, November-December 2008, pp. 1750–1760.

[82] Bar-Shalom, Y., Li, X. R., and Kirubarajan, T., *Estimation with Applications to Tracking and Navigation*, John Wiley & Sons, 2001, p. 481.

[83] Kailath, T., *Linear Systems*, chap. 9, Prentice Hall, 594-631 1980.

[84] Pittelkau, M. E. and O'Shaughnessy, D. J., "Gyro Misalignment Decomposition Applied to MESSENGER Calibration," *Advances in the Astronautical Sciences*, Vol. 134, AAS, San Diego, CA, February 2009, pp. 1527–1540.